COLOR EVOLUTION IN HIGH REDSHIFT GALAXIES

by

Peter Ronald Manuel Eisenhardt

A Dissertation Submitted to the Faculty of the

DEPARTMENT OF ASTRONOMY

In Partial Fulfillment of the Requirements
For the Degree of

DOCTOR OF PHILOSOPHY

In the Graduate College

THE UNIVERSITY OF ARIZONA

1 9 8 4

INFORMATION TO USERS

8504753

Eisenhardt, Peter Ronald Manuel

COLOR EVOLUTION IN HIGH REDSHIFT GALAXIES

The University of Arizona   PH.D.   1984

University
Microfilms
International   300 N. Zeeb Road, Ann Arbor, MI 48106

PLEASE NOTE:

In all cases this material has been filmed in the best possible way from the available copy. Problems encountered with this document have been identified here with a check mark __√__.

1.   Glossy photographs or pages __√__

2.   Colored illustrations, paper or print __√__

3.   Photographs with dark background _____

4.   Illustrations are poor copy _____

5.   Pages with black marks, not original copy _____

6.   Print shows through as there is text on both sides of page _____

7.   Indistinct, broken or small print on several pages __√__

8.   Print exceeds margin requirements _____

9.   Tightly bound copy with print lost in spine _____

10. Computer printout pages with indistinct print _____

11. Page(s) _____ lacking when material received, and not available from school or author.

12. Page(s) _____ seem to be missing in numbering only as text follows.

13. Two pages numbered _____. Text follows.

14. Curling and wrinkled pages _____

15. Other_____

University
Microfilms
International

COLOR EVOLUTION IN HIGH REDSHIFT GALAXIES

by

Peter Ronald Manuel Eisenhardt

_____

A Dissertation Submitted to the Faculty of the

DEPARTMENT OF ASTRONOMY

In Partial Fulfillment of the Requirements
For the Degree of

DOCTOR OF PHILOSOPHY

In the Graduate College

THE UNIVERSITY OF ARIZONA

1 9 8 4

THE UNIVERSITY OF ARIZONA
GRADUATE COLLEGE

As members of the Final Examination Committee, we certify that we have read

the dissertation prepared by ___Peter Ronald Manuel Eisenhardt___

entitled __Color Evolution in High Redshift Galaxies__

_____

_____

_____

_____

and recommend that it be accepted as fulfilling the dissertation requirement

for the Degree of __Doctor of Philosophy__.

Marc Aaronson _____ _10/18/84_
                                Date

Raymond E. White _____ _18 October 1984_
                                Date

Ray Weymann _____ _18 Oct. 1984_
                                Date

Rodger I. Thompson _____ _October 18, 1984_
                                Date

_____ _____
                                Date

Final approval and acceptance of this dissertation is contingent upon the
candidate's submission of the final copy of the dissertation to the Graduate
College.

I hereby certify that I have read this dissertation prepared under my
direction and recommend that it be accepted as fulfilling the dissertation
requirement.

Marcia J. Rieke _____ _Dec 10, 1984_
Dissertation Director   Date

STATEMENT BY AUTHOR

PREFACE

Writing a doctoral dissertation is both an opportunity and a peril: the opportunity to spell things out in the rigorous detail you feel a subject deserves, and the peril of being sidetracked by irrelevancies. When the subject is cosmology, there is a universe full of details to get sidetracked by. "To describe the universe in terms of our present knowledge is to say almost nothing about everything," (attributed to Schucking by Sandage, Sandage and Kristian 1975.)

I consider myself fortunate to have had the chance to make some increment to the "almost nothing" there is to say.

This contribution was only possible because of the many resources available to me at Steward Observatory. Most important were the people I came in contact with. My advisers, Marcia Lebofsky and George Rieke, supplied me with inspiration, means and assistance at every stage of my graduate student career. From the right size feedback resistor to use in a preamp, to helping me find a job, their support was vital. To them I owe my appreciation of the importance of infrared astronomy.

The Simultaneous Photometer for Infrared and Visual Light could not have been constructed without the machining expertise provided by Wilbur Griffin and Robert Miller. Griffin was also a source of valuable advice on the mechanical design. Most of the electronics were designed and built by Earl Montgomery, who was indispensable in getting the instrument up and running.

iii

I regret that my father, Rudi Eisenhardt, who had more to do with my interest in astronomy than anyone else, did not live to debate the merits of my dissertation.

> ...Just once,
> everything, only for once. Once and no more. And we, too,
> once. And never again. But this
> having been once, though only once,
> having been once on earth - can it ever be cancelled?

> Rilke

My mother, Angelica Eisenhardt, had unfailing faith in my ability to complete my graduate work, often greater than my own, and helped me through many difficult times.

Mary Ellen Kramer, my greatest friend, my wife, has aided this work in many ways, tangible and intangible. Most of all, she has given me faith in myself, and in us.

It is easy to forget what it is we are studying in the midst of worrying about K corrections, error statistics, and detector impedance. For the intense personal reminder, the real presence of everything in the universe, there is no substitute for staring at a clear dark sky. Perceiving the universe - that to me is what astronomy is all about.

TABLE OF CONTENTS

TABLE OF CONTENTS--<u>Continued</u>

TABLE OF CONTENTS--<u>Continued</u>

LIST OF ILLUSTRATIONS

ix

LIST OF ILLUSTRATIONS--<u>Continued</u>

LIST OF TABLES

ABSTRACT

A Simultaneous Photometer for Infrared and Visual light (hereafter SPIV) has been constructed. SPIV uses three dichroic filters to divide light from a common aperture in the telescope focal plane into four colors with bandpasses (in microns) of: 0.42 to 0.7 (V_B); 0.7 to 0.95 (I_B); 1.45 to 1.8 (H); 1.97 to 2.27 (K). The H and K bands are detected by liquid helium cooled InSb diodes. I_B is detected by a helium cooled Si diode, and V_B by an uncooled EMI 9658R photomultiplier tube. The instrument response function (IRF) including the effect of atmospheric transmission is shown. The maximum usable aperture size of 2 mm corresponds to 7 arcseconds on the Multiple Mirror Telescope and to 20 arcseconds on the UAO 61" and 90" telescopes. Information about the sky brightness is combined with the IRF to calculate the expected background noise. These calculations show SPIV should be background noise limited in all bands. Observations show this is true except for I_B, which is detector noise limited. The optical alignment of the four channels is shown to be satisfactory.

The SPIV instrumental magnitude system is defined. Observations of 40 radio galaxies and 39 non-radio first ranked cluster galaxies with known redshifts ranging from 0.019 to 1.6 are reduced on this system, correcting for atmospheric extinction, reddening, and aperture. The transformation to standard magnitude systems is derived.

The reduced V_B-H, I_B-H and H-K colors as a function of redshift are compared for the radio and non-radio galaxies using statistical tests. No convincing differences are found, with the possible exception of H-K in the $z = 0.2$ to 0.4 range. These colors are also compared to a "no evolution" prediction generated by redshifting a composite spectrum of nearby elliptical galaxies, and to evolutionary models from Bruzual (1981). Passively evolving models with little residual star formation and a galaxy formation epoch $z_f > 3$ are slightly favored by H-K observations. These models predict about one magnitude brightening at H by a redshift of one. The I_B-H color becomes redder with redshift much faster than the reddest model, and shows large scatter for $z < 0.3$. The colors flatten at higher redshift and show individual blue deviations. The V_B-H observations follow a track which is fit well by a passively evolving model with no residual star formation and $z_f > 3$. Residual star formation models require an older universe than is allowed by $q_0 = 0.5$, $H_0 = 80$ km/sec/Mpc to fit the red V_B-H envelope at high redshift. Some galaxies show strong blueward deviations for $z > 0.4$. This behavior is most easily explained by episodes of star formation involving small fractions of the total number of stars. Because of the flatness of H-K and I_B-H at high redshift, and the scatter in V_B-H, determining redshifts > 0.4 from broadband colors will be difficult.

CHAPTER 1

INTRODUCTION

High redshift galaxies are among the most interesting objects in the universe. "High redshift" in this dissertation means $z = \Delta\lambda/\lambda > 0.5$ Assuming the standard hot big bang models (Ellis 1984) are correct, galaxies with these redshifts have distances from us which are a significant fraction of the (horizon) size of the universe. Differences between the geometries of closed and open universe models start to become important. The light travel time is a third or more of the age of the universe.

The optical and infrared radiation from normal galaxies is primarily starlight. The successes of stellar evolution theory and the fact that we live in a normal galaxy gives us some confidence that we understand this radiation. Thus high redshift galaxies are, in a sense, test particles of the distant reaches of the universe. This is not true for quasars, which are seen to much higher redshifts.

Combining cosmology with stellar evolution theory leads to a possible contradiction. Observations of globular clusters imply some stars are well over 10 billion years old (Janes and Demarque 1983). Yet if the cosmic deacceleration parameter $q_o = 0.5$, as required by the current inflationary universe models (Guth and Steinhardt 1984), and the Hubble constant $H_o > 65$ km/sec/Mpc (Aaronson and Mould 1983), the

1

universe is <u>less</u> than 10 billion years old. The conflict assumes that atomic and cosmological time scales are the same.

Giant Elliptical Galaxies

It is fortunate that the brightest normal galaxies known are relatively simple systems in terms of their stellar content. These objects, the first ranked cluster galaxies, are invariably ellipticals (Hubble 1936) and have remarkably constant luminosities (Sandage 1972b) Elliptical galaxies have little dust to obscure their light, and are primarily composed of a uniformly old population of stars (Frogel et al. 1978). Nature has provided a test particle (or standard candle) with a large and apparently constant luminosity, and whose stellar evolution can be modelled with few free parameters.

These giant elliptical galaxies are sometimes powerful radio sources. Sandage (1972c) found that the 3C sources which were in galaxies were quite similar to first ranked cluster giant elliptical galaxies, although 3C galaxies extend to slightly lower luminosities. Because such powerful radio sources are rare, many 3C radio galaxies are at very high redshifts. The current record is $z = 1.82$ for 3C256 (Spinrad, Djorgovski and Marr 1983).

Thus most of the known high redshift galaxies are radio sources. Assuming they are like the brightest nearby galaxies, they are giant ellipticals, though of course morphological classification of these very faint objects is extremely uncertain. Nearby ellipticals are assumed to be the descendants of these objects in the remainder of this dissertation.

Figure 1 shows the spectrum of a prototypical elliptical galaxy, taken from Lebofsky and Rieke (1984). The spectrum is the average of several nearby ellipticals observed in the optical with the Oke scanner and in the infrared with the Steward Observatory Fourier Transform Spectrometer. The ordinate plots the number of photons per unit wavelength. It is clear that the bulk of a typical elliptical's luminosity is in the near infrared, and the effect of redshift is to increase the ratio of infrared to visible luminosity. High redshift galaxies should be very red objects, and the need for infrared observations is apparent.

The effects of evolving stellar populations, however, are greatest in the ultraviolet (Bruzual 1981), because the main contribution here is from hot stars, and luminous 0 stars evolve quickly. Light emitted in the ultraviolet by high redshift galaxies is observed at optical wavelengths. Since information about stellar evolution is critical (see e.g. Tinsley 1972) to determinations of cosmological parameters, both optical and infrared observations of high redshift galaxies are required. Such observations, when they have been made at all, have usually been done on different telescopes, on different instruments, through different apertures.

Objectives of the Dissertation

With such considerations in mind, the design and construction of a four channel Simultaneous Photometer for Infrared and Visible light (hereafter SPIV) was begun. The primary design objective was to measure

Standard Elliptical Galaxy Spectrum
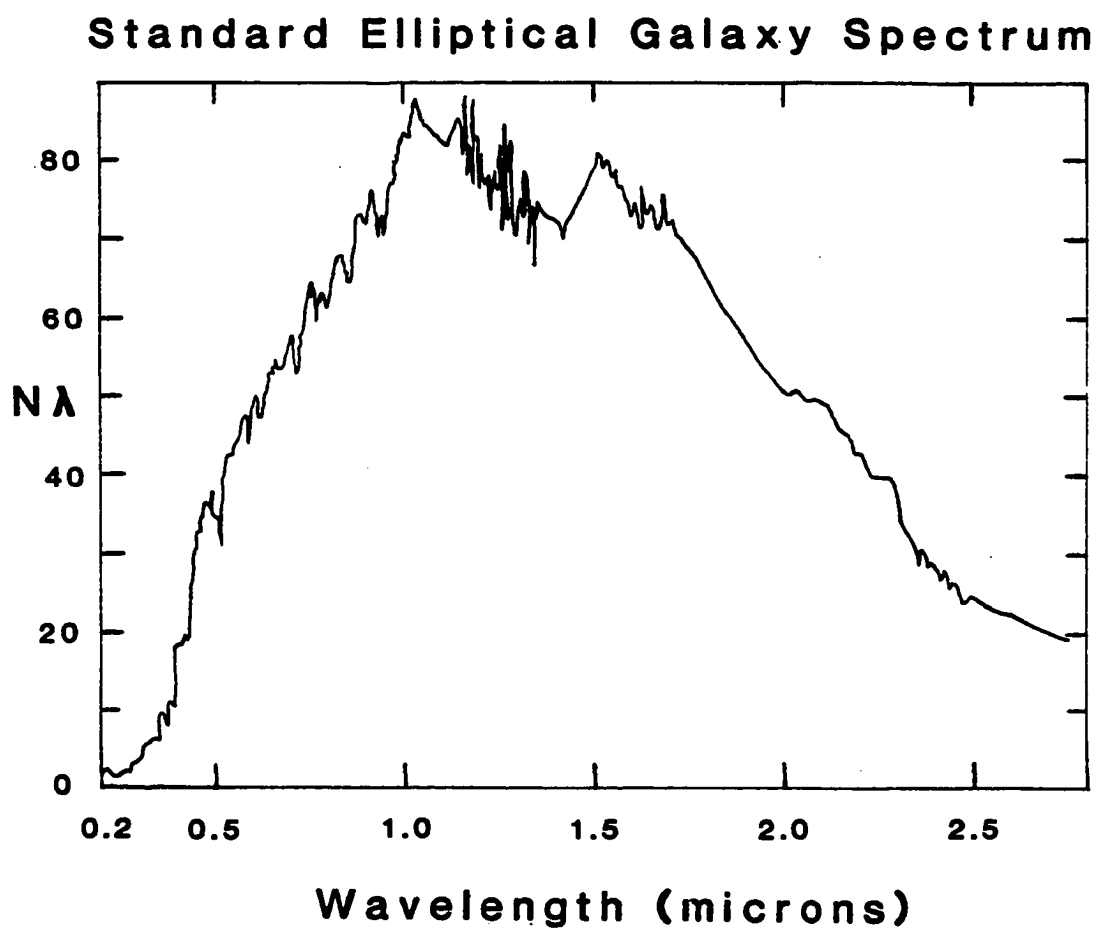
Figure 1. Standard Elliptical Galaxy Spectrum. The relative number of photons per unit wavelength is plotted versus the wavelength in microns.

visual and infrared colors, in the range 0.4 to 2.5 microns, of distant galaxies as efficiently as possible.

The scientific goals of this dissertation are to obtain information about a sufficient number of galaxies to answer some or all of these questions:

1) How do the optical and infrared colors of giant elliptical galaxies change with redshift?

2) What differences are there between radio and optically selected galaxies?

3) What amount of stellar evolution is required to explain the observed color evolution?

4) When did galaxies form?

5) Is galaxy evolution dependent on local conditions?

6) What does the above knowledge tell us about Hubble's constant H_0 and the cosmic deacceleration parameter q_0?

To address these questions we would like, ideally, spectro-photometry as a function of time. What is presented here as a practical alternative, since high z galaxies are faint objects, are colors as a function of redshift.

Existing Studies

The above questions have intrigued many astronomers over several decades, so a great deal of relevant published work exists. Rather than attempt to discuss them all, I will focus on those most relevant to this dissertation. Volume IX of the Stars and Stellar Systems series

contains several review articles which are pertinent (Sandage, Sandage and Kristian 1975).

Optical Studies

Optical studies of high redshift galaxies have mainly been carried out using the Palomar 200" (Kristian, Sandage and Westphal 1978, Gunn and Oke 1975) and the Lick 3m and KPNO 4m telescopes (Smith and Spinrad 1980; Spinrad 1982; Spinrad, Djorgovski and Marr 1983).

Virtually all known redshifts > 1 are for 3C galaxies measured by Spinrad and collaborators; a recent summary of the observations of 3C objects is found in Laing, Riley and Longair (1983). Because most of the redshifts are from emission lines, little information on the continuum is available in Spinrad's work. The emission lines typically have equivalent widths of a few hundred Angstroms. Spinrad (1982) has suggested the ionization levels can be explained by shock-wave heating, and that these very high redshift galaxies are likely to be involved in mergers (Djorgovski 1984).

Gunn and Oke (1975) analyzed spectrophotometry of 28 first ranked cluster galaxies with redshifts up to $z = 0.46$ in an attempt to determine q_0. Using a procedure which is insensitive to selection effects, they found values ranging from -1.3 to +0.3 ± 0.65 depending on whether effects of evolution and the highest redshift galaxy (3C295) were included. (Note the change from open to closed universe occurs when q_0 becomes > 0.5 (Weinberg 1972, p. 441)). They also suggested radio and optical luminosity might be correlated. Kristian, Sandage and Westphal (1978) found $q_0 = 1.6$ ±0.4 assuming no evolution from Johnson BVR

photometry using a larger sample restricted to z < 0.4. On the basis of color vs. redshift curves, they found no evidence of evolution for z < 0.4. They also found that the luminosity of brightest cluster galaxies was constant within an rms scatter of 0.35 magnitudes, and independent of whether the galaxy was a radio source. Both papers demonstrated that q_0 was relatively insensitive to the aperture correction, which allows for the changing fraction of galaxy luminosity accepted by a fixed instrumental aperture, so long as an aperture correction was made.

Butcher and Oemler (1978) in a study of the colors of galaxies in clusters found an excess number of blue galaxies for redshifts of order 0.4 as compared to nearby clusters. While controversial, this result appears to have held up (see Dressler 1984), although it may not apply to the first ranked cluster member.

Gunn, Hoessel and Oke are presently at work on an optically selected sample of first ranked cluster galaxies which extends at least to redshifts of 0.92 (Oke 1983). Some of these galaxies have been observed here. Oke (1983) states that there is no evidence in this sample for changes of color with redshift, but suggests this may be not be true for less luminous members of clusters.

Evolutionary Models

The technique of assuming an initial mass function and star formation rate, and using theoretical stellar evolution tracks to predict the integrated properties of galaxies as a function of time was pioneered by Beatrice Tinsley (1967,1972). She found that the effect of luminosity evolution on q_0 was substantial, raising its apparent value

by at least 0.5, and that large luminosity increases imply smaller color changes and vice versa (Tinsley 1972). This result has particular relevance to the findings of Kristian, Sandage and Westphal (1978) summarized above. More recent work (Gunn, Stryker and Tinsley 1981) finds that giant elliptical galaxies are composed of an old metal rich population with an initial mass function similar to that for the solar neighborhood, plus some hotter stars whose origin is uncertain. Blue stragglers and young stars are suggested as possibilities for the hot component.

The most recent evolutionary synthesis models are those of Bruzual (1981, 1983) which explore a wide range of models and pay particular attention to the ultraviolet. He found models whose star formation rate declines exponentially with approximately a one billion year timescale best fit observations of elliptical galaxies for a Hubble constant of 50 km/sec/Mpc and $q_0 = 0$. Infrared <u>colors</u> are virtually unaffected by evolution. These models are used in this dissertation.

Infrared Studies

The first comprehensive study of nearby elliptical galaxies at infrared wavelengths was that of Frogel et al. (1978). They find that the luminosity of ellipticals is dominated by giant stars. A color luminosity relation in the sense that more luminous ellipticals are redder, and color gradient in the sense that the nuclei are redder are reported. Both effects are small: less than 0.1 magnitude for a factor of ten in aperture or one magnitude in luminosity, and the data are consistent with much smaller slopes.

There have been several studies of high redshift galaxies in the infrared in recent years. Grasdalen (1980) combined Sandage's V photometry with his own infrared measurements and found that the two galaxies with $z > 0.4$ were somewhat bluer than expected for no evolution. He also found luminosity evolution was required if $q_0 = 0$. Lebofsky (1981) used infrared photometry of 33 radio and non-radio giant ellipticals to show that there was no observable evolution in H-K with redshift, and that $q_0 = 0.05 \pm 0.3$ for the sample with $z < 0.5$. The value for q_0 rose to 0.7 when the higher redshift galaxies were included, which she attributed to luminosity evolution. Puschell, Owen and Laing (1982) measured infrared colors of radio galaxies and in contrast to Lebofsky (1981) found anomalously blue values for high redshift objects. Ellis and Allen (1983) measured infrared J-K colors for a sample of optically selected galaxies with known redshift, and found that they differ from the colors of radio galaxies. Lilly and Longair (1982, 1984), in the study which most closely parallels this one, observed a sample of 83 3C galaxies in the infrared, and combined this with published V photometry for 27 galaxies with $z < 0.5$ and CCD r photometry for 12 galaxies with $z > 0.5$. They found no evidence for color evolution in H-K, and that radio galaxies of $z < 0.4$ match the no evolution prediction based on nearby non-radio ellipticals. The optical infrared colors showed a range of colors at high redshift, with all being bluer than predicted for no evolution. Approximately one magnitude of evolution by $z = 1$ was found if $q_0 < 0.5$.

The studies cited above are (quite naturally) preoccupied with finding a value for q_0 by measuring magnitudes as function of redshift. This value is plainly very sensitive to luminosity evolution, and requires accurate magnitude measurements. This dissertation, in contrast, will focus on color evolution, about which there have been conflicting statements. SPIV is naturally suited to accurate color measurements, because it measures its four bands through the same aperture at the same time. The optical/infrared colors in particular have not been previously measured with the same aperture. The other major goal addressed here is to compare radio and optically selected galaxies, for this has only been done in the optical at redshifts less than 0.4 (Sandage 1972c, Kristian, Sandage and Westphal 1978). The Hubble diagram is briefly mentioned, but detailed discussion of luminosity evolution and q_0 is deferred to that by Lebofsky and Eisenhardt (1984).

Outline of the Dissertation

Chapter 2 discusses the design of SPIV, specifying the properties of the optics and the instrument response function. The expected performance of SPIV observing high redshift galaxies is calculated. A note of explanation: Because so little optical light is expected from high redshift galaxies, the two bands below one micron are much broader than the standard Johnson filters, and are referred to as V_B and I_B.

Chapter 3 describes the ancillary equipment required to observe with SPIV, outlines the observing procedure, and lists the observing

sessions and objects observed. The actual performance is compared to the calculations of Chapter 2.

The reduction and calibration of the observations are the subject of Chapter 4. The instrumental standard system is defined, and various corrections to the data are justified.

Chapter 5 addresses the questions outlined above, using statistical tests to compare radio and non-radio galaxies, and observations to predictions. Predictions from Bruzual's (1981) models are presented and evaluated.

Chapter 6 summarizes the results of the dissertation.

CHAPTER 2

INSTRUMENT DESIGN

The design of SPIV was first presented in Eisenhardt (1982).
Much of that discussion is reproduced here, although the present work
should be considered definitive, as the instrument was not operational
when the earlier paper was written. Those readers not concerned with
the details of the design may wish to skip to the discussion of expected
performance at the end of the chapter after reading the summary of the
important features in the next few paragraphs.

The main design goal of SPIV is to obtain coarse spectral
information for many distant galaxies. Specifically, SPIV should have
the capability of measuring several broadband colors to 10 - 20%
accuracy for a typical giant elliptical galaxy at a redshift of one in
less than an hour on the Multiple Mirror Telescope (hereafter MMT).
This requires high efficiency, low noise, and that most of the light
from an extended galaxy be accepted.

High efficiency is accomplished by good transmission, high
quantum efficiencies, and by simultaneously measuring all four channels.
The bandpasses are nearly as broad as detectors and atmospheric windows
allow. The limiting noise source is the background, which cannot be
reduced without decreasing the net efficiency. The usable aperture size
is large enough, and spectral coverage broad enough, so that most of the
light from high redshift ellipticals transmitted by the atmosphere is

12

accepted by SPIV. Simultaneousness was desired from the outset, both because of efficiency, and equally importantly, because of the resulting accuracy in measured color ratios.

Briefly, light from the telescope is deflected by a diagonal chopping mirror into the liquid helium cooled dewar (see Figure 2). At the (f/9) focal plane, there is a choice of apertures from 0.5 to 2 mm, corresponding to 5 to 20 (61" and 90") or 1.75 to 7 (MMT) arcseconds. Next, light is split by the Valtec dichroic, transmitting wavelengths greater than 1 micron, and reflecting the shorter wavelengths. Long wavelengths next encounter an infrared H filter, which reflects non-H wavelengths to a K filter. H and K are then imaged by silicon lenses onto InSb diodes. On the short wavelength side, light encounters the OCLI dichroic, which transmits light longwards of 0.7 microns to be detected by a silicon diode, and reflects the visible through a field lens out the far side of the dewar. After passing through either a standard V filter or a UV blocking filter (invariably the latter in this work), visible light is finally detected by an EMI 9658R photomultiplier tube (PMT). In early observations no UV blocking filter was used. References to this unfiltered V_B are in parentheses following the filtered V_B values. The overall instrument response function (IRF), including atmospheric transmission, is shown in Figure 3.

Signals from the diodes are amplified by a liquid nitrogen cooled dual JFET, the first stage in a preamplifier design discussed by Rieke et al. (1981). The optics are designed to accomodate an f/9 or slower beam, allowing SPIV to be used on a variety of telescopes. The PMT, which has an extended S-20 cathode, is operated at ambient

SPIV : Bottom View

Entrance Window

Dewar Case

Valtec Dichroic

OCLI Dichroic

Aperture Slide

Aperture Selection
Control Rod

R_B

Si Diode

Zn Se Lens

Relay Lens

In Sb
Diode

K

Si Lens

H Filter

Si Lens

In Sb
Diode

H

Helium Cooled
Work Surface

Field Lens V_B (Photomultiplier)
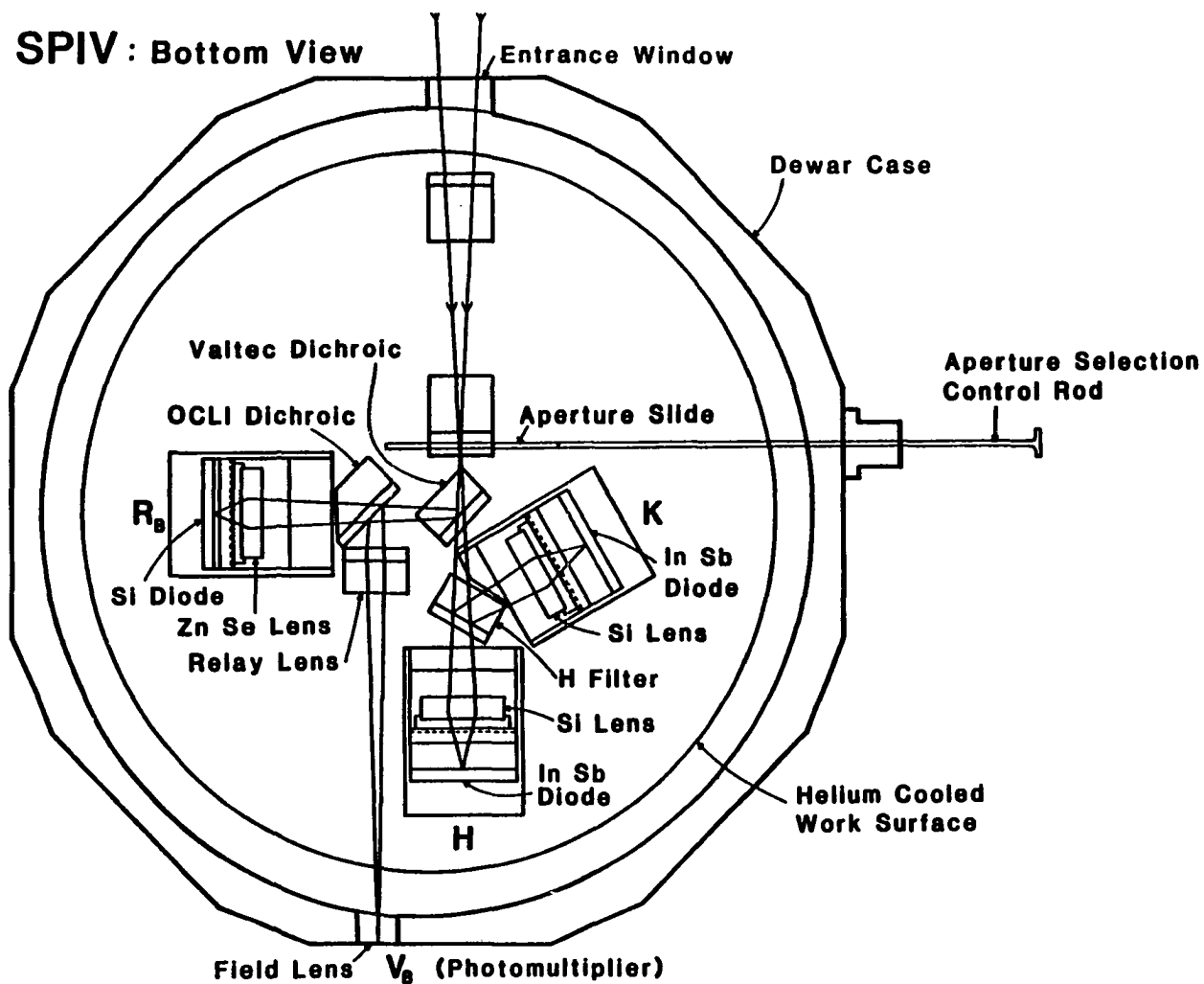
Figure 2(a). Bottom View of SPIV. For clarity, many details have been omitted: Electronics, radiation shields, baffles, etc.
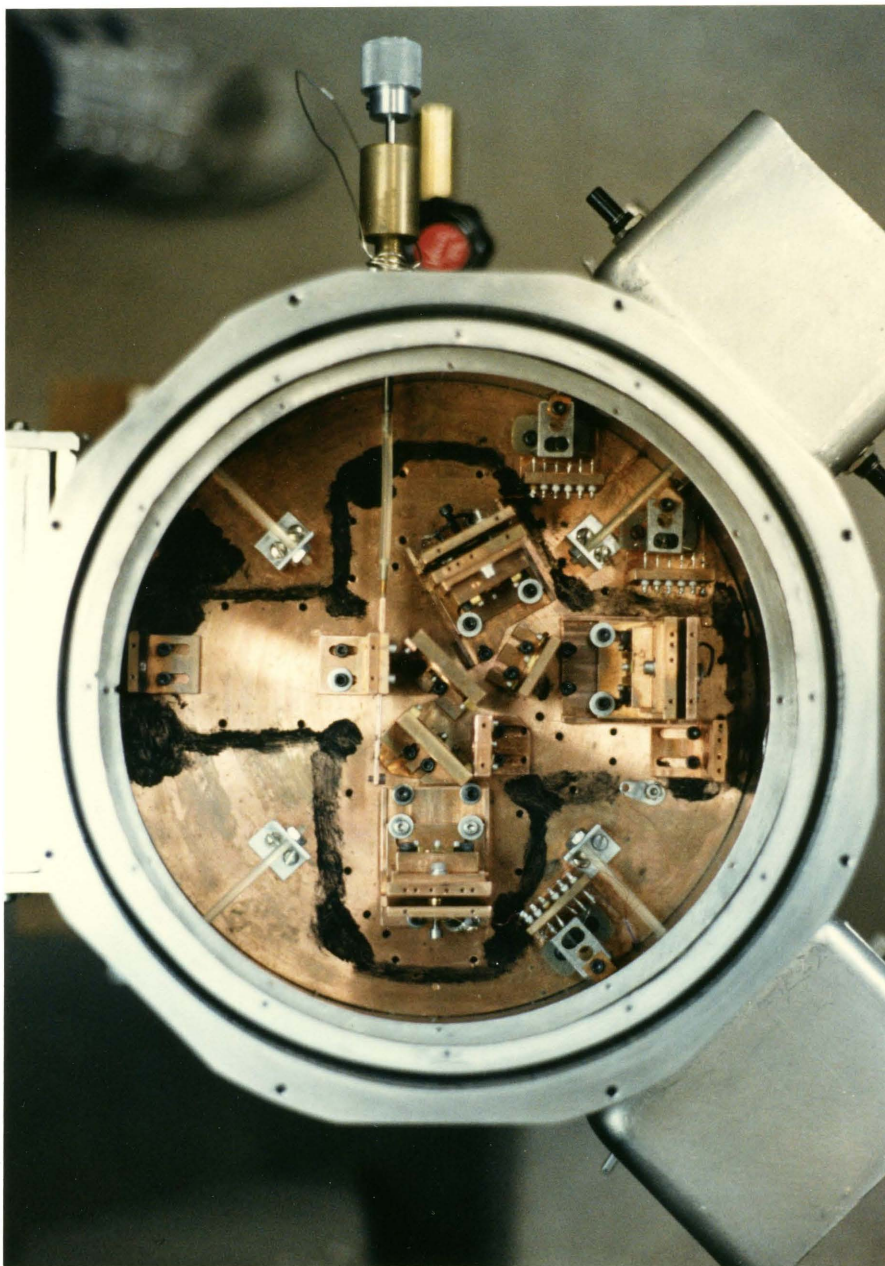
Figure 2(b). Photograph of SPIV Work Surface. In this photograph, the liquid nitrogen cooled JFET's are visible, though they are not drawn in Figure 2(a).
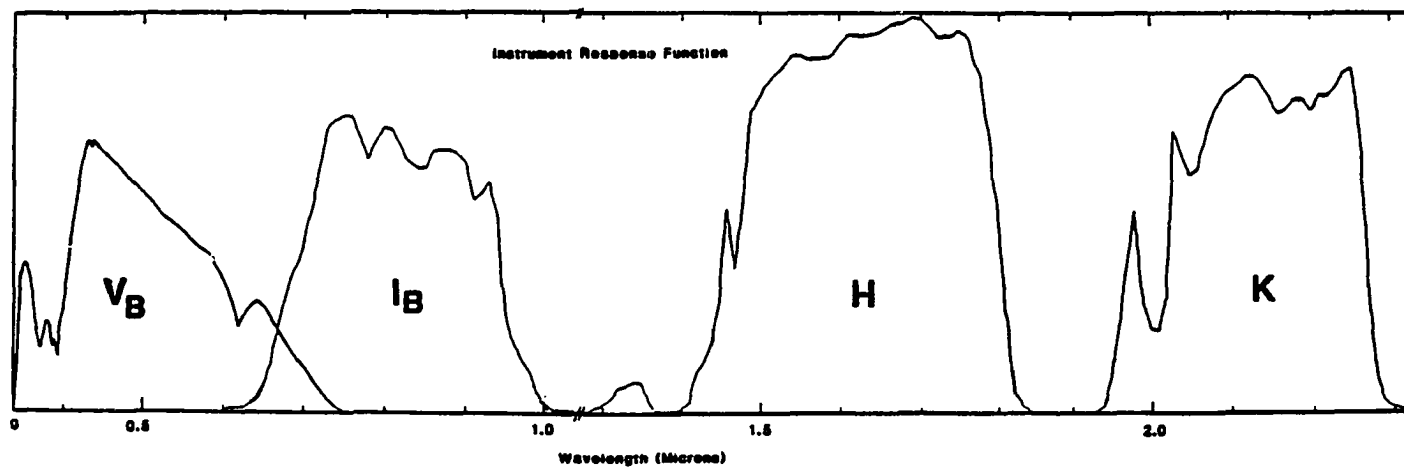
Figure 3. Instrument Response Function. The relative response including atmospheric transmission of the four SPIV bands are shown. Peak values are approximately 15% for V_B and 50% for the others.

temperature, and uses a magnetic lens to reduce dark current below sky background levels. The InSb diodes are also background limited.

Photometric Band Separation

Spectroscopic Approach

The main design goal of SPIV is to obtain coarse spectral information for galaxies, so a spectroscopic approach was considered in some detail. Since the wavelength varies by a factor of six over the range of interest, this required a prism rather than a grating as the dispersing element. The prism must generate enough dispersion relative to the projected aperture size to allow good separation of the four channels. At the same time efficiency must be kept high, and bulk and cost reasonably low. For this reason designs with a minimum number of surfaces were explored.

The Fèry prism (Fèry 1911) excells in this regard, since it uses the prism as both camera and collimator, the refractive analogue of the Rowland diffraction grating. Unfortunately, it suffers from severe astigmatism, a major handicap for the photometric purposes envisioned here.

An on-axis Littrow prism (silvered on the second surface) using a single spherical mirror as both camera and collimator was investigated in detail, using a ray tracing program developed by me. The prism was tilted perpendicularly to the dispersion direction to allow the converging spectrum to be picked off by a diagonal mirror, as shown in Figure 4. Even for the optimum choice of prism angle, tilt and

TOP VIEW

RED

Focal
Plane

Rear surface of Prism silvered

BLUE

Spherical Mirror is
Camera and Collimator

SIDE VIEW

Prism tilt allows converging spectrum to be picked off by Diagonal Mirror

Hole bored in Prism lets light from Telescope through
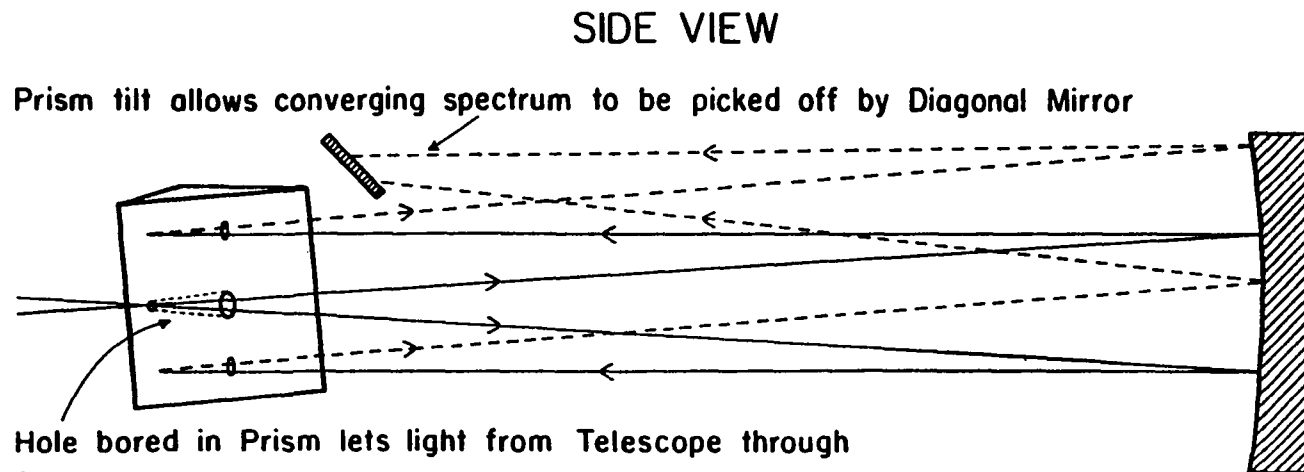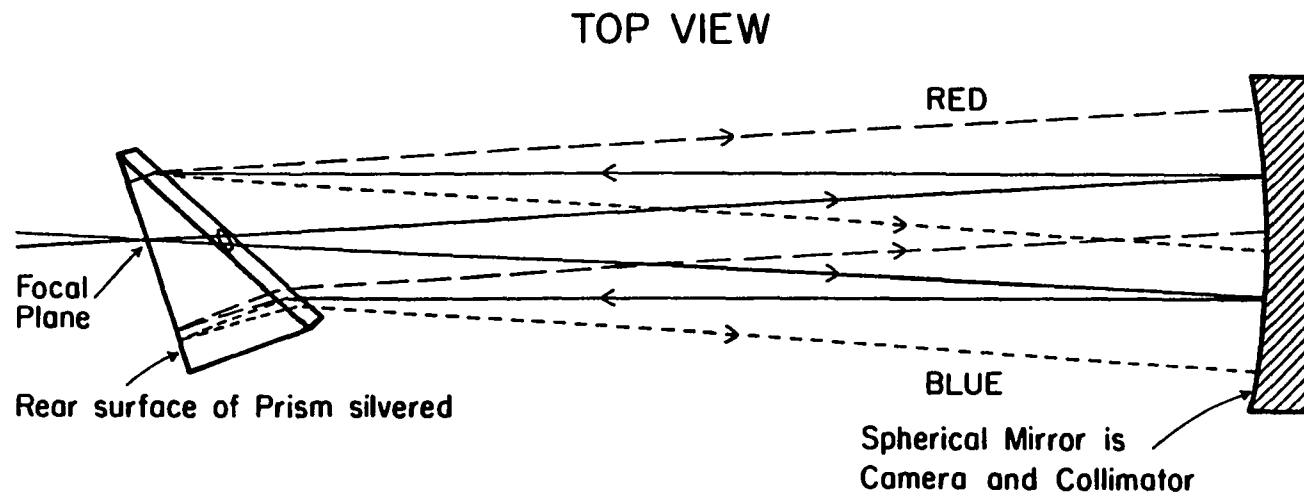
Figure 4. On-axis Littrow Prism Spectrograph Design.

incidence angle, however, it proved very difficult to get enough dispersion in comparison to the aperture size.

It is not difficult to show that the various constraints impose fundamental problems on the prism approach. From Snell's law, the dispersion $\Delta\theta$ is roughly equal to Δn_{prism}, and the size of the spectrum is $\Delta\theta \cdot f_{camera}$. The projected aperture size is $d_{ap} \cdot f_{cam}/f_{coll}$. Therefore the size of the spectrum compared to the projected aperture is $f_{coll} \cdot \Delta\theta/d_{ap} \equiv R$. The collimator diameter, and hence the size of and light path through the prism, are approximately given by f_{coll}/f_{no}. The f_{no} is fixed at 9, and the aperture size is 2 mm (see section on reducing optics below). Investigation of available materials showed fused silica to have the highest dispersion over the range of interest, namely $\Delta n=0.03$ from 0.4 to 2.5 microns. Fused silica does have some absorption in this range: the coefficient is about 0.03/cm (Smith, Jones and Chasmar 1957). Thus to keep absorption losses small the path length must be < 8 cm, i.e. $f_{coll} <$ 70 cm. Then R is < 10, which is not adequate to cleanly separate four channels. These estimates are quite close to the results obtained from ray tracing. Higher grades of fused silica with lower absorption are available, but the cost for the necessarily large piece required rises to impractical amounts, and in any case it was felt that one meter represented a reasonable size limit for the instrument.

Dichroic Approach

Because of these problems with the prism approach, attention was redirected towards dichroics, which are certainly more "traditional" than prisms in a photometer.

Dichroics are in some sense the heart of SPIV, allowing the four fold gain of simultaneous photometry to be realized. The desired bandpasses were H and K (roughly 1.4 to 2.5 microns) and as much of the region below the silicon diode's cutoff (near one micron, see section on detectors below) as possible. Considerable effort was spent searching for a stock filter which would split around one micron, but in the end a special coating run from Valtec was required. The split between V_B (0.4 to 0.7 microns) and I_B (0.7 to 1.0 microns) was accomplished using a stock cold mirror from OCLI, while it was found that an H filter reflected K quite successfully. Transmission tracings are shown in Figure 5. The dichroics are not perfect: the Valtec leak at 6350 A° is particularly bothersome, as is the fact that the turnover from reflection to transmission is at 0.95 rather than 1.0 microns. Response below 0.42 microns is small and erratic (a UV blocking filter eliminates this response). However, the overall performance is reasonably good: 80% to 90% efficiency for each of the bands.

Detectors

The choice of detectors centered around various types of light sensitive diodes: InSb, Ge and Si. The performance of these in the range from room temperature to liquid helium has been described in Rieke et al. (1981). Their spectral response and quantum efficiency of the Si
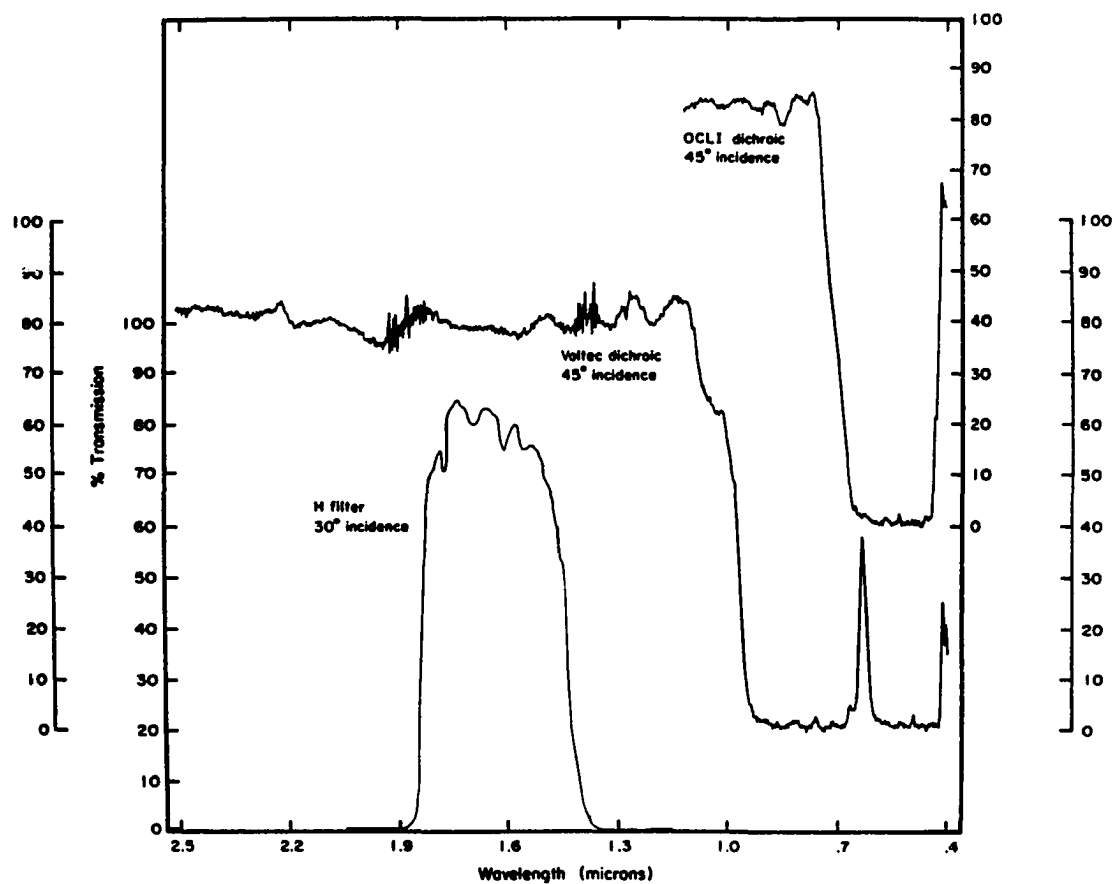
Figure 5. Transmission Tracings for Dichroics Used in SPIV. The upper right scale refers to the OCLI dichroic, the lower left to the H filter, the outer scales to the Valtec dichroic. H filter data was obtained using a CVF, the dichroics were measured using the KPNO Cary spectrophotometer.

and Ge diodes were measured by the author using a lamp calibrated by the National Bureau of Standards, provided by Richard Cromwell; a laboratory blackbody source; and narrow band filters loaned by Kitt Peak National Observatory (hereafter KPNO). Noise measurements as a function of frequency were obtained using a low noise amplifier (whose noise was measured and subtracted quadratically) and electronic filter. These allowed the calculation of the noise equivalent power (NEP - defined as the radiant power incident on the detector for which the signal is equal to the rms noise in one second) as a function of temperature and wavelength. For example, an optical detector with an NEP of 10^{-15}Watts/$\sqrt{Hz}$ on a telescope with a one square meter collecting area (and no transmission losses) could measure Johnson V for a 15th magnitude A0 star with a signal to noise ratio of about 4 in one second. The diode NEP calculations are summarized in Figure 3 of Rieke et al. (1981), reproduced here as Figure 6.

The Si and InSb diodes achieved minimum NEPs near 1. x 10^{-16} W/$\sqrt{Hz}$, while 10^{-15}W/$\sqrt{Hz}$ was achieved for the Ge diode. In all cases the best performance was at liquid helium temperatures (4°K), though the long wavelength response is then curtailed. Noise in these diodes is due to a number of causes, not all of them understood, but a major factor is simply the size of the sensitive area. For this reason the diodes are quite small. The Si and InSb results are for diodes selected from among several for high performance, while for Ge only one diode was available. Also, the Ge diode had a 1 mm diameter, compared to 0.5 mm for the others, which should cause about a factor of two increase in noise. More recent tests (Rieke 1984) indicate that Ge diodes can
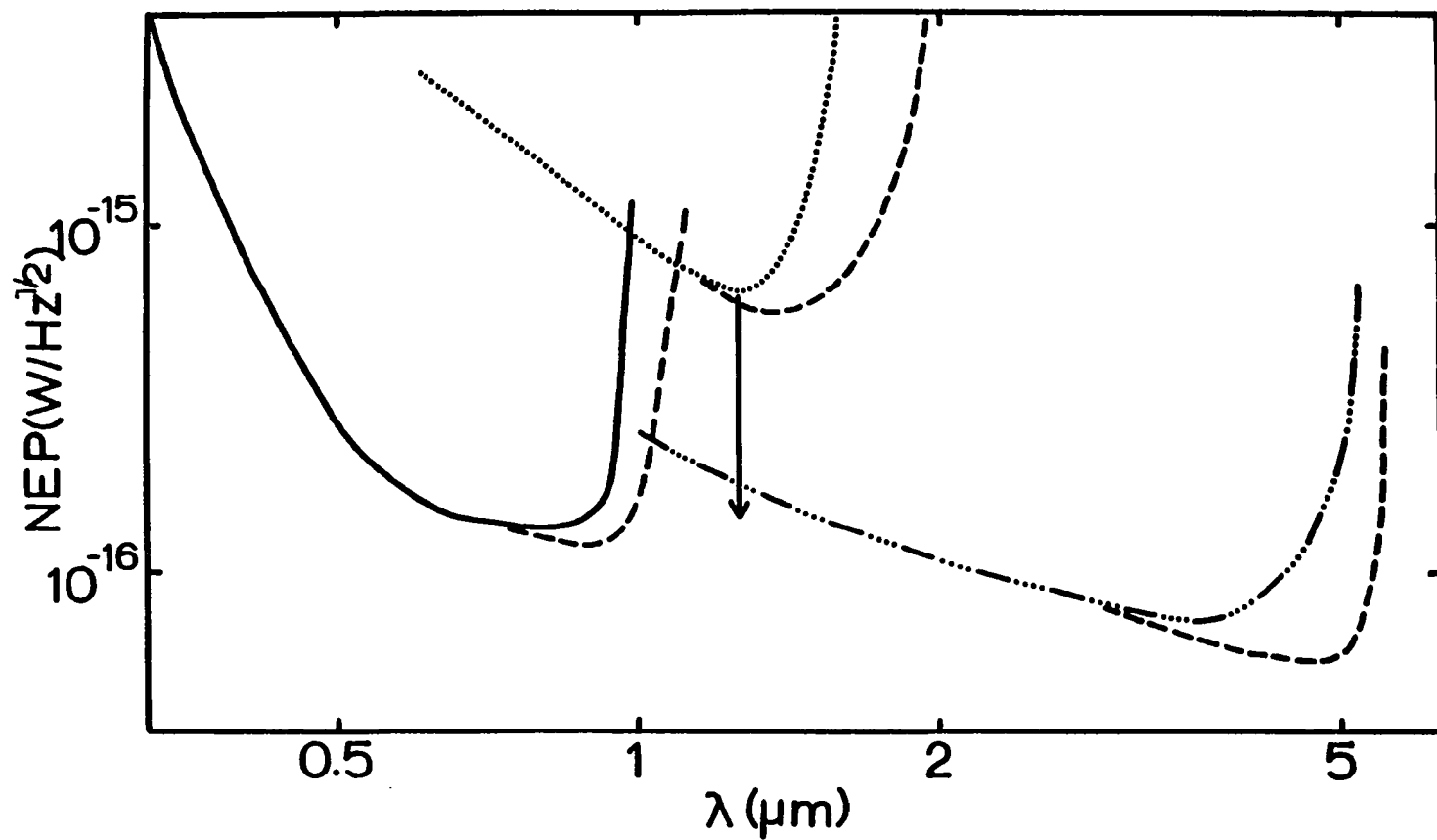
Figure 6. NEP's for Si, Ge and InSb diodes. The log of the noise equivalent power is plotted with a solid line for Si, dotted for Ge, and dot-dash for InSb, at 4°K. Dashed lines show the long wavelength response lost by cooling to 4°K. Reproduced from Figure 3 of Rieke et al. (1981).

achieve effective NEP's of less than $10^{-18}W/\sqrt{Hz}$, with a different preamplifier design (Low 1984, see Electronics section below). These diodes are well suited for measurements in the 0.8 to 1.6 micron range.

InSb is the clear choice at K (2 microns) and has proved very successful in many Steward Observatory infrared photometers over the range 1 to 5 microns. It is therefore used in SPIV for both the H and K bands. Shortwards of 1 micron Si diodes are the preferred detector - except that numerous alternatives already exist in the visible. Because of its compactness and ease of operation, and the fact that its NEP is low enough for measurements to be background rather than detector limited (see section on performance below), the Si diode was selected for the region 0.7 to 1.0 microns (I_B). . Below 0.7 microns detector noise limits performance, and photomultiplier tubes become the detector of choice.

After surveying the available tubes, the EMI 9658R, which has an S-20 cathode with extended red response, was selected. The cathode is prismatically corrugated so that reflected (and hence undetected) photons are deflected parallel to the PMT face and have a second chance to generate a photoelectron. This PMT has good quantum efficiency (25-30% peak near 0.4 microns, 7% at 0.7 microns) and is fairly rugged. It has the virtue of not requiring cooling to achieve background limited performance, provided magnetic lenses are used to reduce the effective size of the cathode. The measured dark current with magnetic lenses at room temperature was 8 x 10^{-11} amperes.

There are certain practical difficulties in the use of the above diodes. The best performance is at 4°K, and InSb diodes will not

operate at all at room temperature, which complicates alignment. Techniques for maintaining cryogenic temperatures have been discussed by Low and Rieke (1974). These result in the available cold mounting area being rather restricted: SPIV uses a comparatively large dewar with an eight inch diameter work surface. A bottom view is shown in Figure 2.

Electronics

The diode preamplifier design, which is discussed in detail in Rieke et al. (1981), uses a dual JFET as the first stage. This device has low noise at liquid nitrogen temperatures, and must be near the diode to minimize noise from capacitive pickup, but will not operate at $4°K$. Hence it must be isolated from the helium cooled work surface, and is thermally connected to the nitrogen cooled radiation shield (see Figure 2 in Rieke et al. 1981).

The PMT is operated in DC or "current" mode. The preamplifier uses an operational amplifier with feedback to convert current to voltage, and includes a "crowbar" which grounds the high voltage supply if the anode current exceeds a threshold value (typically a few microamperes).

It should be noted that an integrating preamplifier has recently been developed, which promises much better performance (as mentioned above, Low 1984). Because the device integrates, the readout noise (about 14 electrons) is more meaningful than the NEP. However, tests with Ge and Si diodes have shown that with the longest practical integration times the effective NEP can approach a few times 10^{-19} W/$\sqrt{Hz}$. Unfortunately, for InSb diodes, leakage current limits the

integration time so that the technique is not advantageous. Because it is background limited (see below) this preamp would not improve SPIV's performance much. But for low background applications such as spectroscopy the potential gains are large.

Reducing Optics

Reducing optics are required because of the need for a reasonably large aperture - seven seconds of arc or more (see section on aperture corrections in chapter 4) - and at the same time for small area detectors (see above). Seven arcsec corresponds to 2 mm at the MMT f/9 focal plane, while the InSb and Si detectors have a 0.5 mm diameter. The EMI photocathode has a diameter of nearly two inches, but with magnetic lenses to reduce the dark current, the most sensitive region is restricted to the central 4 mm (see Figure 7).

Field Lenses

The most desirable configuration for the reducing optics is the field lens, imaging the primary mirror onto the detector surface. Fluctuations in position in the focal plane are fluctuations in the angle at which light strikes the primary. At the primary image, these fluctuations cause changes in the angle at which light strikes the detector, not changes in the position on the detector. Because of sensitivity variations (such as those in Figure 7) across the detectors, this is obviously an advantage.

Unfortunately, it proved impractical to use field lenses for the diodes. The distance from the field lens to the primary is approximately the same as the telescope's focal length, and much greater

Spatial PMT response: output (amps $\times 10^{-7}$) vs. position (inches)
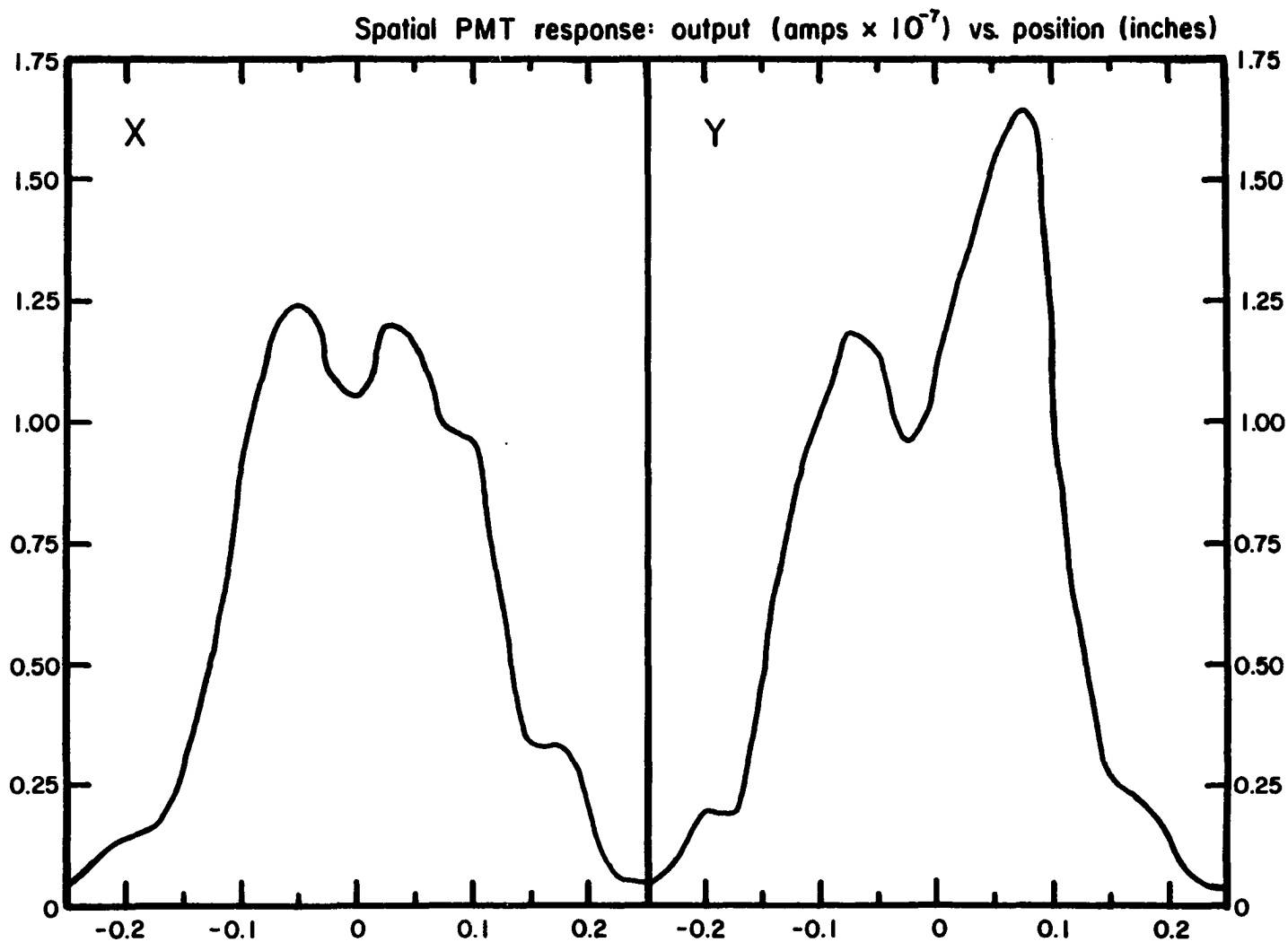
Figure 7. Variation in Output with Position for the EMI 9658R. Measurements were made with magnetic lenses in place. The cathode potential was -1000 volts.

than the field lens focal length. Thus the primary image will appear at the focus of the field lens, with a size: $d = D_{tel} \cdot f_{field}/f_{tel} = f_{field}/f_{no}$. Since we are given $f_{no.} = 9$, $d=0.5$ mm, this means $f_{field} = 4.5$ mm. The f/9 beam has a minimum size at the focal plane of 2 mm. Therefore all three dichroics, field lenses and diodes must be within 3 cm of the focal plane if the lenses are to be slower than f/1. This is too confining. Designs with two lenses may have been feasible, but efficiency has to be kept high, and the presence of the dichroics limits the possible lens positions severely.

Focal Plane Imaging

Instead the focal plane was imaged onto the detector, even though spatial sensitivity variation is then a problem. Tests indicate that this variation isn't too serious for the diodes: less than 20% (Montgomery 1982). This was confirmed at the 61" telescope, as is shown in Chapter 3.

Even this compromise proved difficult. Although it is impractical to have three lenses, dichroics and diodes within 3 cm of the focal plane, the cold work surface of the largest commonly available dewar is only eight inches across. In the end a distance of 8 cm from the focal plane was chosen for the lenses, with the detector distance then an additional 1.2 cm (see Figure 2). This should easily have imaged the 2 mm field within the 0.5 mm detectors, but due to aberrations from the fast (f/1) single element spherical lenses, the fit is rather tight. Being able to use silicon with its high refractive index (3.5) helped, but for the I_B channel ZnSe (n=2.5) was the best

available material. Consequently, the I_B channel has the poorest image, as shown in Figure 8. The image at K (not shown) is very similar to that at H. There are some small light losses, particularly at I_B, of the outer rays from a 2 mm aperture (see Table I). The losses for K (not shown) are smaller than those for H since silicon has less dispersion at K. In actual use these losses are small (see Chapter 3).

Alignment. The alignment of the diode reducing optics was far from trivial, since the operating temperature is 4°K. Great effort was expended to ensure that the beam profiles were nearly optimum. The lens mounts were designed to permit small (25 micron) repeatable increments in their position relative to the detector in all three coordinates. The initial alignment of the lens mounts (with lenses removed) and diodes was performed visually using a He/Ne laser at room temperature. The leak in the Valtec dichroic (see Figure 5) fortuitously coincides with the He/Ne laser line, which was helpful in aligning the two InSb diodes. The lenses were then inserted, and an f/9 beam was generated using a lens in front of the dewar window. The two dimensional beam profile was then measured by noting the output from each diode as a laboratory blackbody source was scanned across the focal plane, adjusting the f/9 lens focus for each band measured. The source diameter was small (60 microns in the focal plane) in comparison to the 2 mm aperture being imaged onto the diodes. Iterations on this initial profile were then measured, until satisfactory profiles were obtained. Each iteration required about one day, and consisted of: opening the dewar and adjusting the lens mounts; sealing the dewar and evacuating it to below 10^{-5} torr; cooling first to liquid nitrogen and then to liquid
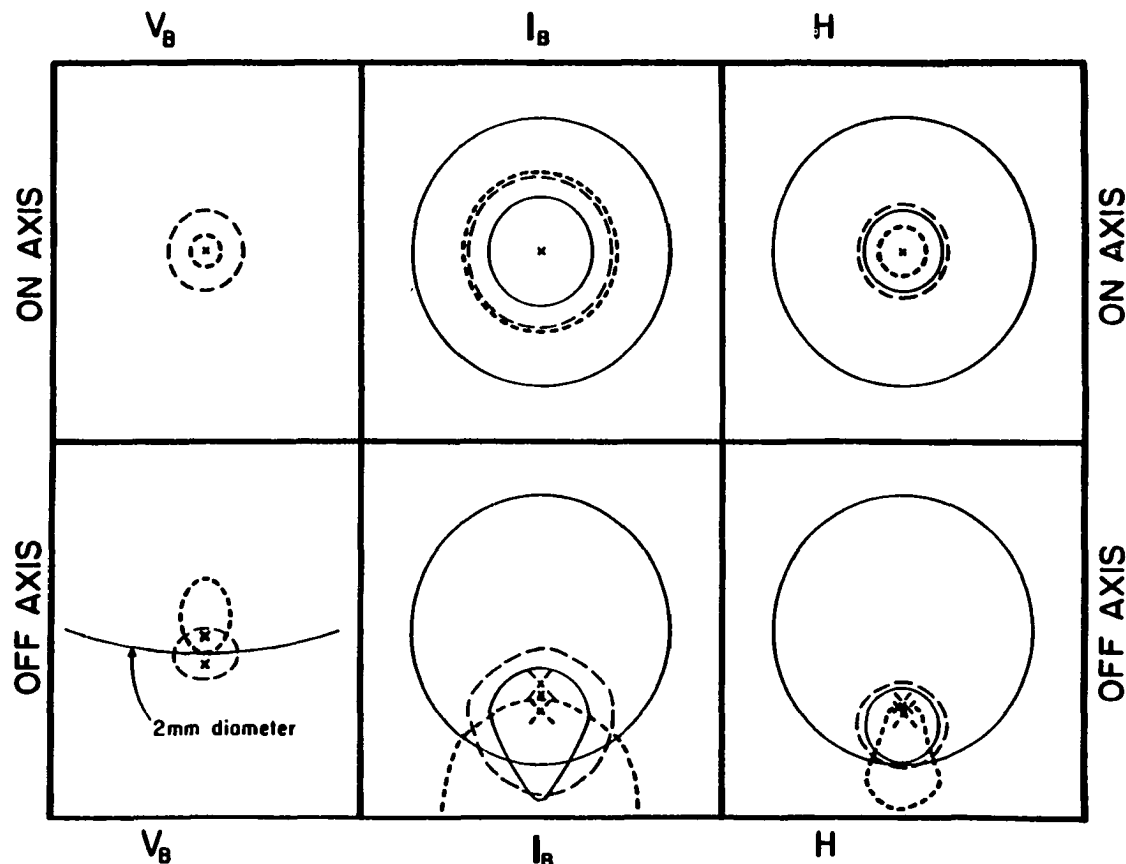
Figure 8. Images of Points on Detectors. For V_B, points are on the primary mirror, with the off axis point at the primary edge. The arc labelled 2 mm diameter refers to the size of the image of the primary on the photomultiplier cathode. For I_B and H, points are in the focal plane, and off axis refers to the edge of a 2 mm aperture. Long light dashed lines refer to long wavelengths in the band, heavy short dashes to short wavelengths in the band, solid lines to intermediate wavelengths. The outer circles shown for I_B and H are the 0.5 mm diameter diode sensitive areas. Crosses refer to chief ray positions.

TABLE I

Percentage Light Missing Detectors Due to Lens Aberrations for Various Aperture Sizes.

Losses as a function of off axis position (in mm) in the focal plane are shown for I_B channel with a ZnSe lens and the H channel with a Si lens. The losses for the the K channel, which also uses a Si lens, are similar to those for H, but somewhat smaller. No light misses the V_B channel photomultiplier cathode. Losses are calculated for a central wavelength and the two endpoints of the channels, shown under the heading λ in microns. n is the refractive index of the lens material at the indicated wavelength. Avg is the average loss over wavelength at the particular off axis distance, given by: Avg = [2(central λ loss) + outer λ losses]/4. Avg 1 is the cumulative loss assuming a uniform light distribution within the listed radius, while Avg 2 is the cumulative loss assumin a centrally peaked distribution: uniform out to 0.5 mm radius, then falling off as $1/r^2$.

Channel	Average	$\lambda(\mu)$	n	0.35	0.40	0.50	0.55	0.65	0.75	0.85	0.95	1.00	1.05	1.15	1.25
				Off axis position or aperture radius in mm											
I_B		1.00	2.489	--	--	--	--	2.	11.	16.	19.	22.	22.	27.	34.
		0.85	2.510	--	--	--	--	--	--	1.	8.	12.	16.	26.	32.
		0.70	2.557	1.	2.	5.	6.	9.	11.	16.	20.	21.	23.	28.	33.
	Avg			0.3	0.5	1.3	1.5	2.8	5.5	8.5	13.8	16.8	19.3	26.8	32.8
	Avg 1			0.1	0.2	0.6	0.7	1.3	2.3	3.7	5.7	6.8	7.9	11.1	14.4
	Avg 2			0.1	0.2	0.6	0.7	1.2	2.1	2.6	3.7	4.4	5.0	6.5	8.0
H		1.80	3.460	--	--	--	--	--	--	--	3.	8.	12.	22.	29.
		1.66	3.470	--	--	--	--	--	--	--	1.	2.	9.	22.	32.
		1.40	3.493	--	--	--	--	--	--	3.	6.	6.	9.	14.	32.
	Avg			--	--	--	--	--	--	0.8	2.8	4.5	9.8	20.0	31.3
	Avg 1			--	--	--	--	--	--	0.2	0.7	1.1	1.9	4.9	8.9
	Avg 2			--	--	--	--	--	--	0.1	0.4	0.5	0.9	2.2	3.9

helium temperature; measuring the beam profiles as above; and finally warming the dewar up for the next iteration.

PMT Field Lens

For the V_B channel the case is somewhat different: here the spatial variation is substantial (Figure 7), the detector area is larger, and the detector is farther from the focal plane. Thus a field lens is required, but the limitations on it are less severe. Yet limitations remain. The photomultiplier has to be at least 3.5 cm from the outer edge of the dewar case to accomodate the magnetic lenses. If a single element field lens were also outside the dewar, the window becomes quite large, making thermal radiation leakage into the dewar a problem. I decided to use two lenses, the first a relay lens, the second serving double duty as window and lens, leaving the efficiency as high as if a single lens and flat window were used. The projected primary image is of fairly good quality, and small enough (2 mm) to easily fit in the region of peak sensitivity (see Figure 8).

Instrument Response Function

In order to improve efficiency, the V_B and I_B bands were chosen to be as broad as possible. Even if the sky background dominates the noise, the signal to noise ratio still improves as the square root of the bandwidth. The result is that these colors are not closely related to Johnson V and I. Also, the K filter is non-standard (see section on noise at K below). The combination of broad bandpasses and very red objects made it essential to know the shape of the IRF.

Correction for low temperature

Determining the IRF was complicated by the fact that the performance of the interference filters is a function of temperature. Transmission tracings were taken at room temperature, while SPIV operates at four degrees Kelvin. The main effect is a change in wavelength scale for the filters. This wavelength shift was calibrated using a monochromator borrowed from UCSD. The performance of the InSb and Si diodes at 4°K is shown in Figure 6. The 9658R PMT is operated at ambient temperature, and its quantum efficiency was taken from curves supplied by the manufacturer. (The discussion in Chapter 3 suggests the actual efficiency is somewhat lower for V_B).

Atmospheric transmission

The final ingredient in the IRF at the telescope is the effect of the atmosphere. For V_B, monochromatic extinction coefficients for unit airmass from Kitt Peak were used (Hayes 1982). For the other bands, transmission values were taken from Figures 5-31(a), 5-31(b), and 5-32(a) of Wolfe and Zissis (1978). For I_B and H, the atmospheric path length used was 300 meters. Since the main absorber in these bands is water, which has a small scale height, the short path length is justified. For K the main absorber is CO_2, and the longer path length of 5.5 km was appropriate.

The combination of the above information yields the IRF shown in Figure 3. The vertical scale is arbitrary and is different for each color. Approximate peak efficiencies are 15% for V_B, and 50% for I_B, H, and K. The effective wavelengths are defined by:

$$\lambda_{eff} = \frac{\int \lambda \phi(\lambda) d\lambda}{\int \phi(\lambda) d\lambda}$$ 2.1

where $\phi(\lambda)$ is the IRF for the appropriate band. The values of λ_{eff} in microns are: V_B:0.541 (0.514 without the UV blocking filter), I_B:0.816, H:1.630, K:2.134.

Expected Performance

I now consider the expected performance of SPIV on the MMT observing giant elliptical galaxies at redshifts z = 0.5 and z = 1.0. The actual performance is given in the next chapter. The Robertson-Walker metric is assumed throughout. The aperture size in these calculations is 2 mm or 7 arcsec at the MMT's f/9 focus, corresponding to about 30/h to 40/h kpc where h $\cong$ H_0/100, and H_0 is Hubble's constant in km/sec/megaparsec.

Signal

Because SPIV uses photon detectors, the signals it produces are proportional to the number of incident photons N_λ, rather than the energy spectrum F_λ. I will therefore calculate signals in terms of number of photons per unit wavelength (because wavelength is more commonly used in the optical and near infrared than is frequency). In the following derivation, the subscript "o" refers to quantities in the observer's frame, while subscript "e" refers to the frame in which light is emitted.

Consider a packet of photons dN emitted by a source of (photon) luminosity $N'_{\lambda e}$ in wavelength range $d\lambda_e$ for a time Δt_e. This packet will spread out uniformly over an area A_{prop} with an observed (photon)

flux $F_{\lambda o}$. Then the number of photons in the packet is:

$$dN = A_{prop}F_{\lambda o}\Delta t_o d\lambda_o = N'_{\lambda e}\Delta t_e d\lambda_e \qquad 2.2$$

where the Robertson-Walker metric for a Friedmannian universe with zero cosmological constant gives for the proper area (Peebles 1971):

$$A_{prop} = 4\pi(R_0 r)^2 \qquad 2.3$$

$$R_0 r = \frac{c\{q_0 z + (q_0-1)[(1 + 2q_0 z)^{1/2}-1]\}}{H_0 q_0^2(1 + z)}$$

$$q_0 \equiv -\ddot{R}_0\frac{R_0}{\dot{R}_0^2}$$

where $R_0 = R(t_0)$ is the cosmic scale factor (now), r is the metric distance to the source, and q_0 is the deacceleration parameter. Dots indicate time differentiation. $R_0 r$ reduces to cz/H_0 for small z. The received signal S(z) is given by:

$$S(z) = A_{tel} \int\phi(\lambda_0)F_{\lambda o}d\lambda_o \qquad 2.4$$

where $\phi(\lambda)$ is the IRF, and A_{tel} is the telescope collecting area. Noting that $\lambda_0=(1 + z)\lambda_e$ and that $\Delta t_0=(1 + z)\Delta t_e$, equations 2.2 and 2.4 give:

$$S(z) = \frac{A_{tel} \int\phi(\lambda_0)N'_{\lambda e}d\lambda_e \Delta t_e}{A_{prop}(z) \qquad \Delta t_o}$$

$$= \frac{A_{tel} \int\phi(\lambda_0)N'(\lambda_0/1+z)d\lambda_0}{A_{prop}(z)} \frac{1}{(1+z)(1+z)} \qquad 2.5$$

To estimate the measured magnitude, we can compare this signal to that for a galaxy 10 parsecs away, making use of the absolute magnitude. The redshift corresponding to this distance is very small:

$$z(10pc) = \frac{10pc\ H_0}{c} = \frac{10pc}{1Mpc}\frac{100km/sec\ h}{3 \times 10^5 km/sec} = 3.336 \times 10^{-9}\ h \qquad 2.6$$

Then from equations 2.3 and 2.5 the ratio of signals from a galaxy at 10pc and one at redshift z is:

$$\frac{S(10pc)}{S(z)} = \frac{\int \phi(\lambda)N(\lambda)d\lambda}{\int \phi(\lambda)N'(\lambda/1+z)d\lambda} \left[\frac{q_0 z + (q_0-1)[(1 + 2q_0 z)^{1/2}-1]}{q_0^2 \ 3.336 \times 10^{-9} \ h} \right]^2 \qquad 2.7$$

Here I have dropped the subscript o, $N(\lambda)$ is the present day photon spectrum, and $N'(\lambda)$ is the spectrum at the earlier epoch z. Taking -2.5 log of both sides, and using the following definitions:

$$C_{corr} \equiv 5 \log \left[\frac{q_0 z + (q_0-1)[(1 + 2q_0 z)^{1/2}-1]}{q_0^2} \right] \qquad 2.8$$

$$K_{corr} \equiv 2.5 \log \left[\frac{\int \phi(\lambda)N(\lambda/1+z)d\lambda}{\int \phi(\lambda)N(\lambda)d\lambda} \right]$$

$$E_{corr} \equiv 2.5 \log \left[\frac{\int \phi(\lambda)N'(\lambda/1+z)d\lambda}{\int \phi(\lambda)N(\lambda/1+z)d\lambda} \right]$$

we have finally:

$$m - M = C_{corr} - K_{corr} - E_{corr} - 5 \log(h) + 42.38 \qquad 2.9$$
$$+ \ \text{additional corrections}$$

Here m and M are the absolute and apparent magnitudes. I have taken M_{VB}= -21.5 + 5 log(h) (typical for a giant elliptical - Sandage 1972b), and H-K = 0.24, I_B-K = 2.10, V_B-K = 3.30 (Frogel et al. 1978). C_{corr} is a cosmological correction which depends on q_0 and z. For the case q_0= 0 C_{corr} reduces to 5 log[z + z^2/2]. The additional corrections (such as aperture corrections) are discussed in Chapter 4, and will be ignored for the present. The E_{corr} term is an evolution correction, and represents the effect of changes in the galaxy's spectrum due to the earlier epoch. Determining E_{corr} is one of the major goals of this dissertation, and will be discussed in Chapter 5,

along with K_{corr}, the K correction. For the present purpose of predicting SPIV's performance, E_{corr} will be assumed to be zero. This is a conservative assumption because high redshift galaxies are expected to be more luminous than nearby ones. Expected magnitudes for the cases z=0.5,z=1, q_0 = 0 and 0.5 are in Table II.

The actual number of photons detected in each channel can be found from equation 2.5 and information about N(λ), A_{tel}, and the IRF and losses in each band. N(λ) can be found from Figure 1 by normalizing to an absolute V magnitude of -21.5 + 5 log(h). Then from equations 2.3, 2.5 and 2.6:

$$K = \frac{\int \phi_V(\lambda)AO(\lambda)d\lambda}{\int \phi_V(\lambda)N_{fig\ 1}(\lambda)d\lambda} \frac{10^{21.5/2.5}}{h^2} 4\pi\left[\frac{c}{H_0}3.336 \times 10^{-9}h\right]^2 \quad 2.10$$

$$= 4.43 \times 10^{-9} \frac{\int \phi_V(\lambda)AO(\lambda)d\lambda}{\int \phi_V(\lambda)N_{fig\ 1}(\lambda)d\lambda} 4\pi(c/H_0)^2$$

$$= 11.2 \times 4\pi(c/H_0)^2$$

Here K = N(λ)/$N_{fig\ 1}(\lambda)$, AO(λ) is the photon flux from a 0 mag AO star, where from Johnson (1966) 0 magnitude at 0.55 microns is 3.81 x 10^{-23}W/m^2Hz, or 1.046 x 10^{11} photons/sec/m^2micron, and $\phi_V(\lambda)$ is the Johnson V response function. AO(λ) and $\phi_V(\lambda)$ are taken from Djorgovski (1984). Then from equations 2.3, 2.5 and 2.8, we have for the number of detected photons:

$$S(z) = \frac{A_{tel}\int \phi(\lambda)N_{fig\ 1}(\lambda/1+z)d\lambda\ 11.2}{10^{Ccorr/2.5}} \quad 2.11$$

The collecting area of the MMT is taken to be 15 m^2. The light path at the MMT from sky to instrument includes 5 reflections, each of which I

TABLE II

Predicted Performance of SPIV on the MMT

m_m is the magnitude for a giant elliptical calculated using equation 2.9, m_{a0} using equation 2.12. Noise is the number of noise electrons/$\sqrt{t(sec)}$ Sig is the number of detected photons/sec. S/N is the signal to noise after one hour integration. (V_B) is the value for V_B without the UV blocking filter.

z	q_0	entry	V_B	(V_B)	I_B	H	K
-	-	Noise	37.4	41.5	346.	1100.	1012.
0.5	0.	m_m	21.30	21.38	19.17	16.67	16.05
		m_{a0}	21.42	21.65	19.09	16.70	16.06
		Sig	22.9	29.7	565.	1040.	803.
		S/N	37.	43.	98.	57.	48.
	0.5	m_m	21.02	21.10	18.89	16.39	15.77
		m_{a0}	21.15	21.37	18.81	16.43	15.79
		Sig	29.5	38.3	729.	1340.	1040.
		S/N	47.	55.	126.	73.	62.
1.0	0.	m_m	24.56	24.50	22.00	18.82	17.81
		m_{a0}	24.70	24.78	21.92	18.86	17.83
		Sig	1.12	1.67	41.4	143.	158.
		S/N	1.8	2.4	7.2	7.8	9.4
	0.5	m_m	24.03	23.97	21.47	18.29	17.28
		m_{a0}	24.16	24.24	21.39	18.32	17.29
		Sig	1.8	2.7	68.	234.	259.
		S/N	3.0	4.0	12.	13.	15.

assume to have 90% efficiency. There is an additional factor of two lost because of chopping (the object is only measured half the time). This gives an effective A_{tel} of 4.5 m^2. The resulting expected number of detected photons/second is shown in Table II.

Because SPIV's colors are far from standard, the magnitudes calculated above with equation 2.9 are only approximately correct, since the assumed absolute magnitudes are for standard filters. The more exact magnitudes can be found by comparison with an A0 star (see Chapter 4). It is straightforward to show, using the above equations, that the correct magnitudes are given by:

$$m = -2.5 \log\left[\frac{\int\phi(\lambda)11.2N_{fig\ 1}(\lambda/1+z)d\lambda}{\int\phi(\lambda)A0(\lambda)d\lambda}\right] + C_{corr} \qquad 2.12$$

These magnitudes are also listed in Table II.

Noise

We can distinguish three types of noise that enter into SPIV's measurements: detector noise, statistical signal noise, and background noise. It is convenient to express the contributions from each of these as an equivalent number of electrons produced in each channel as a function of time.

Detector noise can be measured directly, and is dependent on the preamplifier design, as mentioned above. In an integrated measurement, the constant detector noise level adds quadratically, so the integrated detector noise is proportional to the square root of the integration time. This is reflected in the units of the NEP, $W/\sqrt{Hz}$ = Joules/$\sqrt{sec}$. It follows that the number of detector noise electrons is given by:

$$N_e = NEP \cdot QE \cdot \frac{\lambda}{hc} \sqrt{t} \qquad\qquad 2.13$$

where t is the integration time in seconds, QE is the quantum efficiency of the detector, and h is Planck's constant. Note that for the integrating preamplifier design (Low 1984) mentioned above, N_e is independent of time, until noise from leakage current dominates.

Statistical signal noise, or shot noise, is due to the finite number of signal electrons generated by the object. It is simply equal to the square root of the number of signal electrons (equation 2.11).

Background noise is due to fluctuations in the signal from sources other than the object, generally the sky. In the infrared thermal radiation from the telescope can also be a noise source. Again the noise is equal to the square root of the electrons generated in the detector by the background. It can be greater than this, however, because (for example) of systematic changes in the sky brightness. Infrared observers use chopping and wobbling techniques (see next chapter) largely to eliminate these systematic noise sources.

The total noise is the quadratic sum of these three noise sources (assuming they are uncorrelated). Therefore the total noise will decrease at most by a factor of 1.4 if the detector noise is reduced from a level equal to the background noise to a level much smaller than the background. In this situation a detector is said to be background limited. The expected noise rates are shown in Table II. Note that for these rates A_{tel} is 9 m^2, because the noise sources (aside from object shot noise, which is comparatively small) are present throughout the chopping cycle.

At V_B and I_B, sky brightness data is taken from Broadfoot and Kendall (1968). Assuming a seven arcsec aperture, the V_B integral over the PMT response gives 875 detected sky photons/second (1190 with no UV blocking filter), with an rms noise of 29.6 (34.5) $\sqrt{t(sec)}$ e⁻. The measured dark current of 8×10^{-11} amps is equivalent to 500 e⁻/sec at the cathode with a gain of 10^6, so the PMT noise is $22\sqrt{t(sec)}$ e⁻. Signal noise is negligible in comparison, so the total noise at V_B is 37.4 (41.5) $\sqrt{t(sec)}$ e⁻.

The corresponding integral at I_B over sky brightness gives an rms noise of $247\sqrt{t}$ e⁻. Using equation 2.13, the Si diode's NEP of 10^{-16}W corresponds to $242\sqrt{t}$ e⁻ noise at 0.8 microns. Again signal noise is negligible, so the total noise is $346\sqrt{t}$ e⁻.

At K background radiation is primarily thermal, arising from the telescope as well as the sky. Because SPIV is used at f/9 and measures visual as well as infrared light, optical black baffles are in the line of sight. Therefore the thermal background is relatively high, though of course it depends on temperature. For this reason the K filter cuts off at wavelengths shorter than the standard 2.5 microns, and a higher signal to noise ratio (S/N) is achieved. Assuming thermal radiation with a temperature of 290 °K at 60% emissivity from an f/9 cone, the K background noise is $811\sqrt{t}$ e⁻. The detector noise equivalent to an NEP = 10^{-16}W at 2.1 microns with 60% QE is $634\sqrt{t}$ e⁻, yielding a total noise of $1012\sqrt{t}$ e⁻.

The noise at H is more difficult to quantify. It is primarily due to molecular band emission from OH (Chamberlain 1961). The H background varies from night to night and is not correlated with

temperature, but is approximately equivalent to the K band background using the MMT infrared dewar (Rieke 1982). The MMT dewar uses baffling suited to infrared, not visual, purposes, hence it views an effective emissivity of only about 30%. On the other hand the MMT dewar has a broader K filter than does SPIV. Therefore $1000\sqrt{t}$ e^- is a reasonable estimate of the H background noise, while the detector NEP of 10^{-16}W contributes $485\sqrt{t}$ e^- noise at 1.6 microns, 60% QE. The total noise is then $1100\sqrt{t}$ e^-. Note that the dominant noise source is the background in all 4 channels.

It will be of interest in Chapter 3 to know how the signal to noise ratio is expected to vary with telescope aperture and focal ratio (f number), given a constant linear size focal plane aperture. If the dominant noise source is the sky in the measuring aperture, the noise is proportional to the angular aperture size θ and the primary diameter D:

$$N \propto D\theta = D\frac{1}{Df_{no}} = \frac{1}{f_{no}} \qquad 2.14$$

where the equality does not hold for the MMT, because it is an unfilled aperture. If thermal background dominates, as at K, we have:

$$N \propto \frac{1}{f_{no}} \qquad 2.15$$

assuming the linear focal plane aperture size is constant. Finally, if detector noise dominates, it is independent of the telescope. The signal is proportional to the primary area, or to D^2, unless the object overfills the aperture. The resulting relative signal to noise ratios are shown in Table III.

TABLE III

Predicted Relative Signal to Noise Ratios at Three Telescopes

Calculated using Equations 2.14, 2.15 and the discussion above, with D_{MMT} = 4.5m, $D_{90"}$ = 2.3m, $D_{61"}$ = 1.54m; θ = 20 arcseconds (61" and 90") or 7 arcseconds (MMT); and f_{no} = 9 (MMT and 90") or 13.5 (61").

Limiting Noise Source	61"	90"	MMT
Sky Background	1	1.5	8.3
Thermal Background	1	1.5	5.7
Detector Noise	1	2.2	8.5

Table II shows the expected signal to noise ratio (S/N) after one hour on the MMT. The design goals stated at the beginning of this chapter have been met, aside from the V_B channel. This is because V_B corresponds to 0.2 to 0.35 microns in the rest frame at a redshift of one, and as Figure 1 shows, there are very few photons emitted by present day ellipticals in this spectral region. As we shall see, however, z = 1 ellipticals are not identical to present day ones. The actual performance in use is compared with these results in Chapter 3.

CHAPTER 3

OBSERVATIONS

Observing with SPIV involves considerably more than bolting the dewar onto the telescope (see Figure 9). High background levels in the infrared require chopping, or continuous sky subtraction. Each of the four channels is sequentially sampled and digitized at a rate well in excess of the chopping frequency. The electronics and software to accomplish these tasks were developed by Earl Montgomery and my adviser, Marcia Rieke. Most of the work on the viewing system was done by Reinhard Pawlicki and Earl Montgomery.

Observing Procedure

After mounting the dewar, chopping mirror and viewing system at the Cassegrain focus, and connecting the numerous cables associated with SPIV, the telescope is balanced. Mounting and cabling the instrument typically requires about two hours. The observing procedure is essentially as described in Low and Rieke (1974). The electronics and control system are checked to ensure the detectors are getting signals through to the computer, and the chopper is adjusted. Once it is dark enough to find a star, the viewing system adjustments can be made.

Viewing System

Light collected by the telescope encounters the viewing system mirror, which is on a retractable mount, at the Cassegrain focus (see
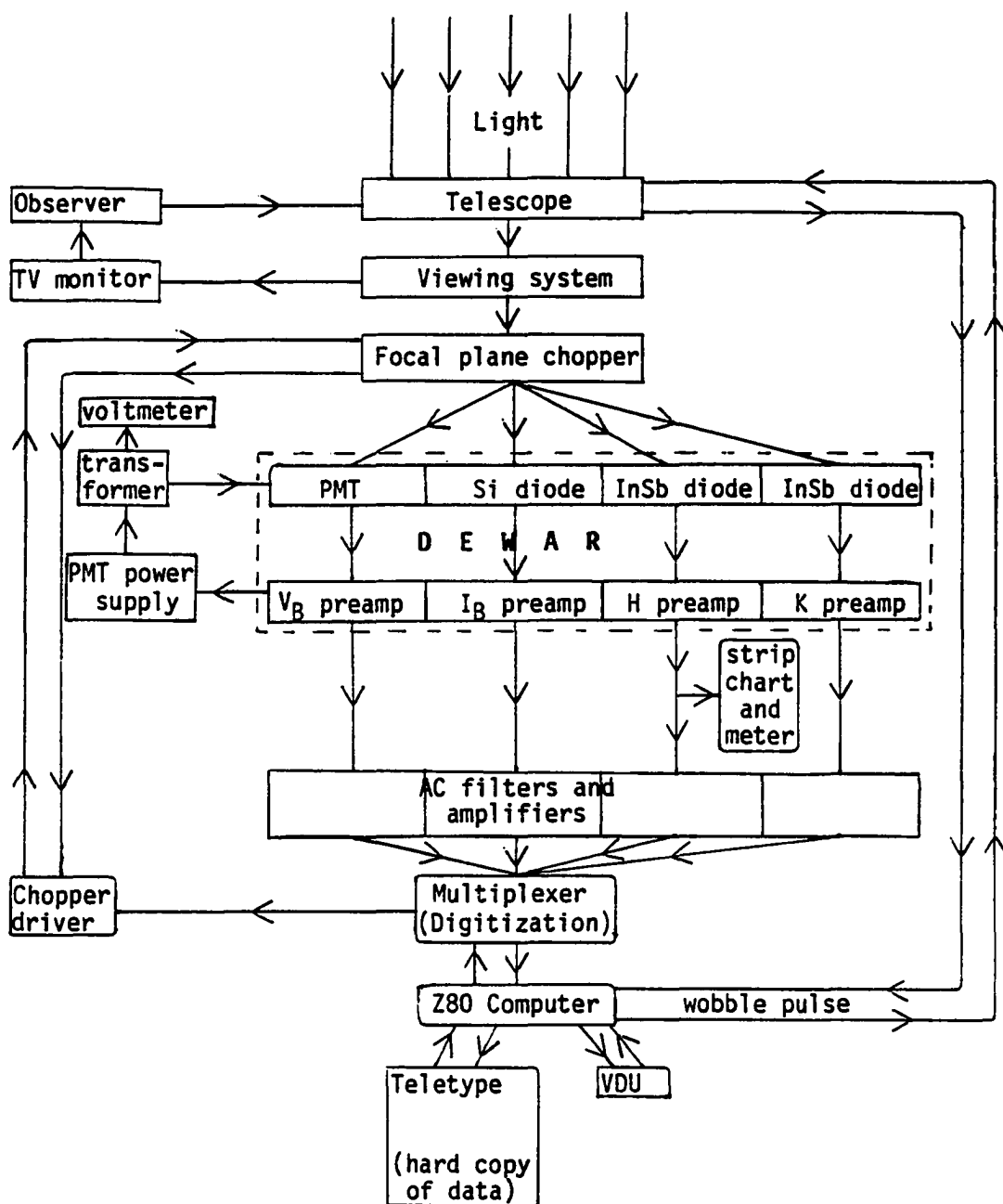
Figure 9(a). Observing Block diagram. The flow of signals and control is indicated by arrows. The dashed line outlines the SPIV dewar components.

Figure 9(b). SPIV and Associated Apparatus at the 61" Telescope. The photograph displays most of the components shown in Figure 9(a). These can be identified using the letter codes in the drawing as follows:

a. Telescope
b. Viewing system
c. Focal plane chopper
d. SPIV dewar
e. Photomultiplier (PMT)
f. V_B preamplifier
g. I_B preamplifier
h. H and K preamplifiers
i. Telescope control paddle
j. Teletype printer
k. Video display terminal (VDT)
l. Z80 Computer
m. Signal monitoring meter
n. Stripchart recorder
o. AC filters and amplifiers
p. Multiplexer/Digitizer
q. PMT power supply
r. PMT monitoring voltmeter
s. Chopper driver
t. Oscilloscope (chopper monitor)
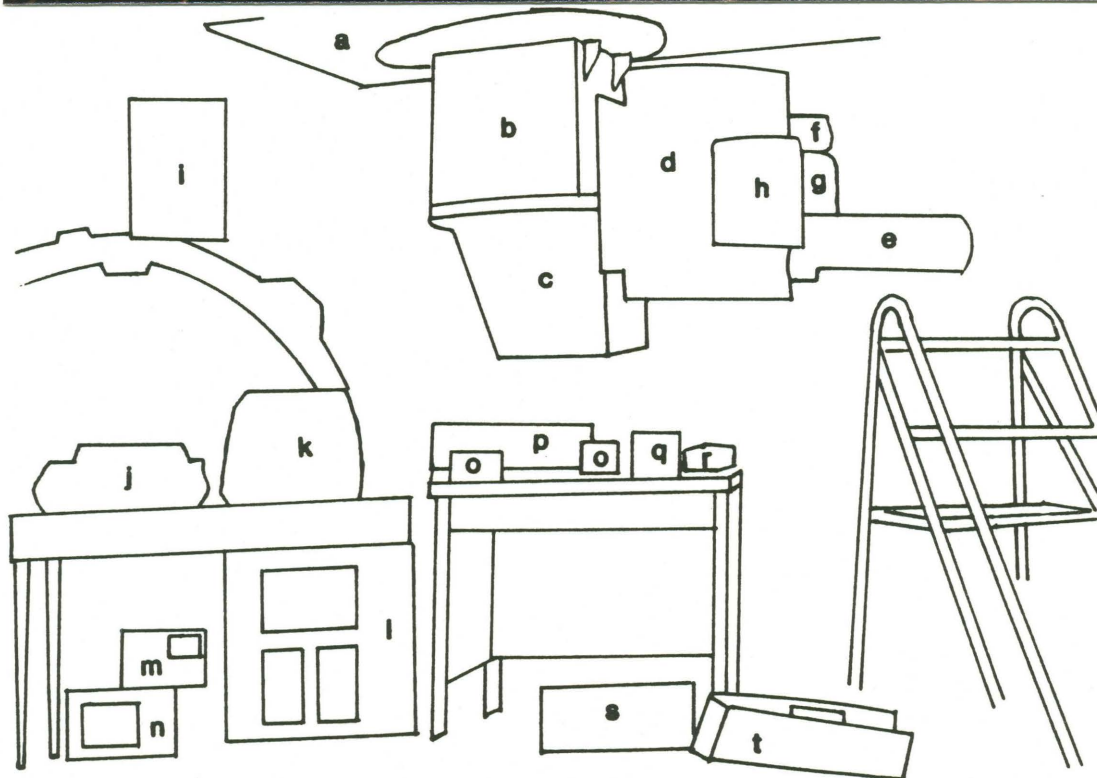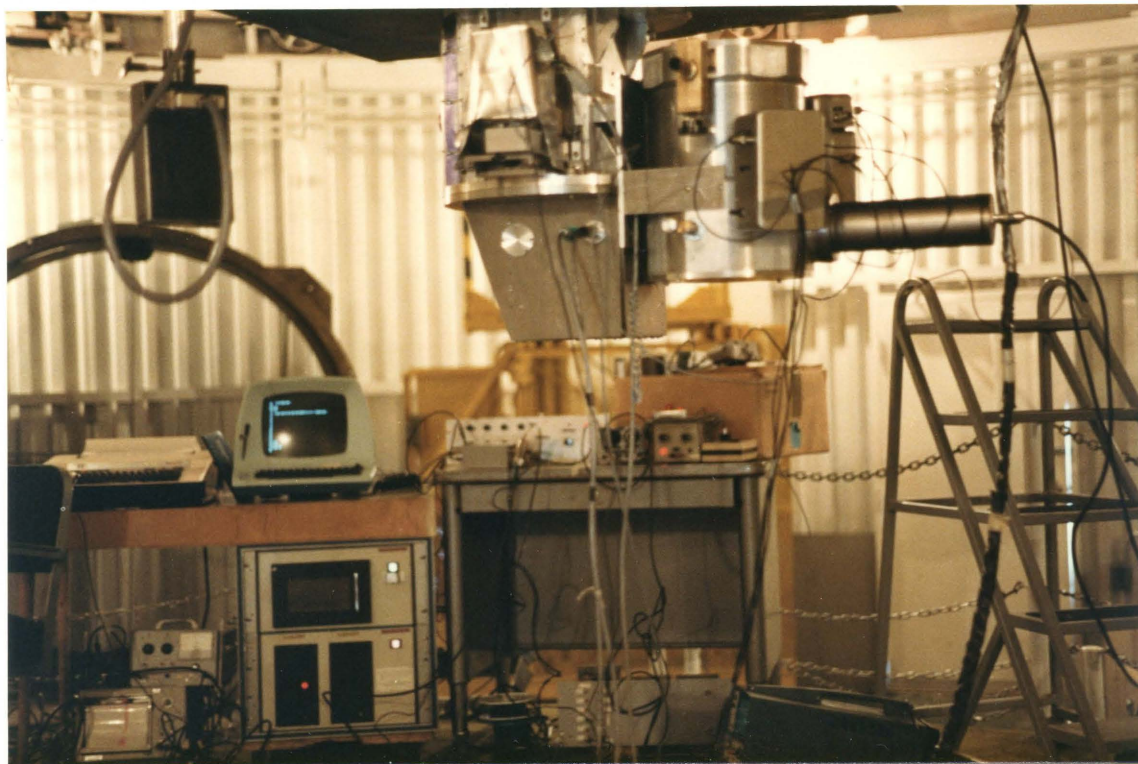
Figure 9(b). SPIV and Associated Apparatus at the 61" Telescope.
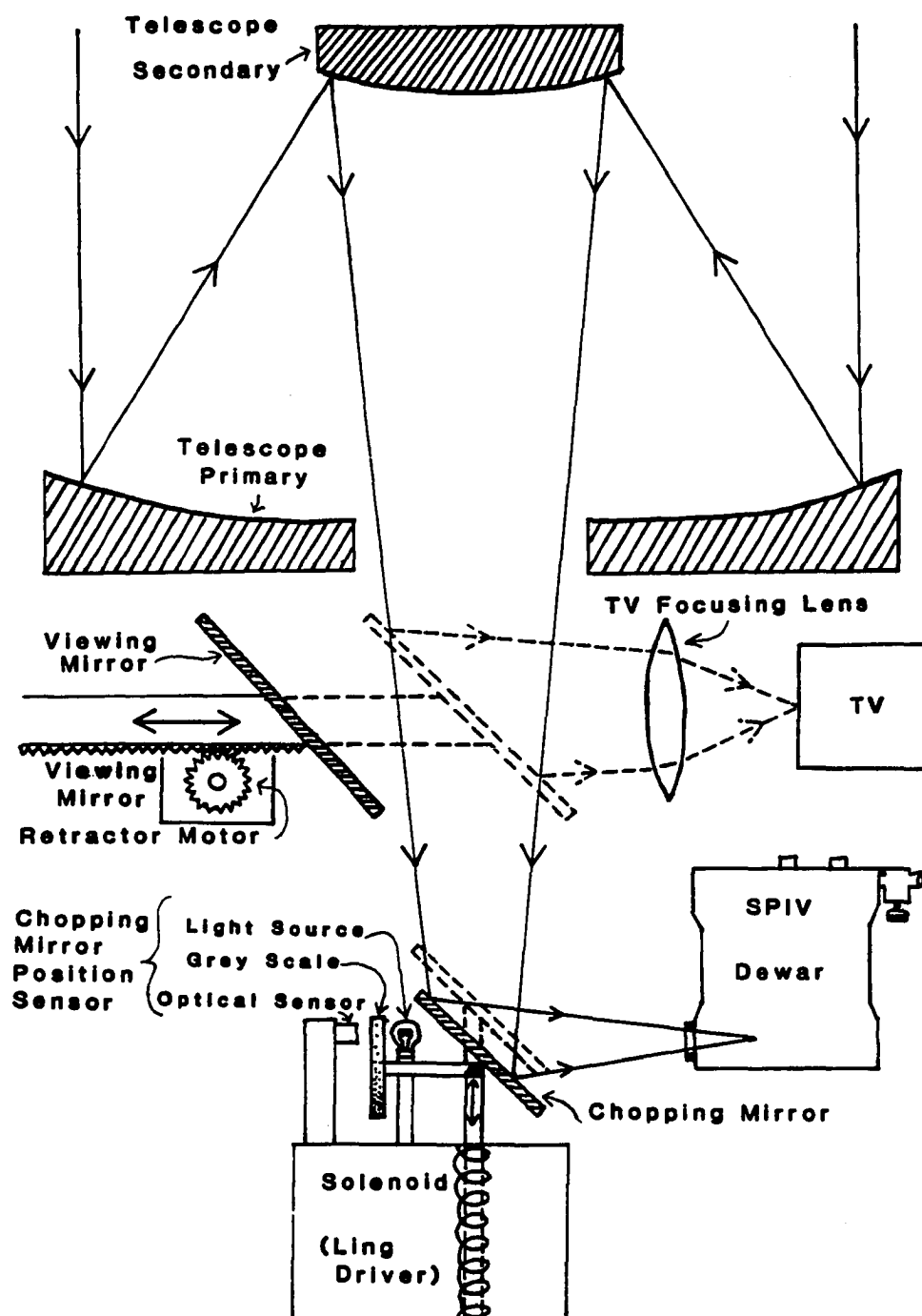
Figure 10. Schematic Cross Section of the Viewing System.

Figure 10). At the 61", the viewing system is integral to the telescope.

Focus. At the start of a run, the telescope secondary focus is adjusted by optimizing the beam profile (six profiles at the MMT), and then focusing the television image. Because the television focus adjustment for the MMT and 90 " is part of the viewing system hardware which travels with SPIV and is locked in place, the television focus coincides with the SPIV focal plane. Therefore, once the beam profile is checked on an initial run, focusing the television image with the telescope secondaries is all that is required on these telescopes.

Guiding. The telescope is centered on a suitably bright star by measuring the half power points (typically for the H channel) in both coordinates, and a cursor set to mark the star's position on the monitor. The telescope is then offset using the coordinate readouts to the object position (determined as discussed below), if necessary via a nearby guide star. Measurements can then begin, with viewing mirror insertions every few minutes to check tracking. At the MMT, because it offsets accurately and has a small field, the telescope is periodically offset to the nearest SAO star, stacked (the six images are superimposed) and centered, and offset back to the object. This procedure requires well under a minute.

Chopping and Wobbling

With the viewing mirror retracted for observing, light next encounters the chopper. Chopping is required for infrared observing because of high background levels. There are two telescope optical con-

figurations, (labelled A and B below) corresponding to the two positions of the chopping mirror, and two positions on the sky (labelled 1 and 2). Assuming position 2 contains the object, the net signal is:

(object B + sky 2B + telescope B) - (sky 1A + telescope A)   3.1

If the telescope configurations are identical, and the sky contribution at 1 and 2 is the same, only the desired object signal will be left. The first assumption especially is dangerous, and for this reason the telescope is repointed so that the object is in configuration A. This procedure, known as wobbling, introduces a third position on the sky, and an opposite phase for the object signal. The result of differencing the signals (or deflections) from the two wobble positions is then:

[(object B + sky 2B + tel B) - (sky 1A + tel A)]   3.2

- [(sky 3B + tel B) - (object A + sky 2A + tel A)]

= (object A + object B) + (sky 2B - sky 3B) + (sky 2A - sky 1A)

Under the assumption that the sky background emission at locations 1, 2 and 3 is the same (these positions are within an arcminute) we are left with the object signal. This assumption may cause difficulty when observing high redshift objects (see Chapter 4).

Because SPIV is used with optical secondaries, chopping is done just before the focal plane using a flat diagonal mirror. The mirror is driven up and down by a solenoid (Ling driver), with position information feedback from an optical sensor which monitors a grey scale attached to the diagonal mount. The chopper throw is set to be slightly larger than the aperture size (2 mm), and the waveform adjusted to be as square as possible. The chopping rate is usually set to 5 Hz because detector NEP's were empirically found to be smallest at this frequency.

The chopper spacing on the sky is determined empirically from the position readouts by centering the telescope on a star in the two configurations A and B. This spacing, which is rechecked when the telescope is moved, is encoded into the mount wobble control. The chopping orientation is in declination on the 61" and 90", and in altitude at the MMT. The wobbling rate is typically set to 15 seconds.

Detection and Digitization

The chopping mirror deflects light into SPIV's side looking dewar, where it is split as described in the previous chapter. Because galaxies are extended objects, the aperture used in this work was the largest available, 2mm, which corresponds to 20 arcseconds on the 61" and 90" telescopes, and to 7 arcseconds on the MMT.

A three position filter slide just in front of the photomultiplier tube allows the choice of a blocked off position, a Johnson V filter, and a UV blocking filter (this position was open in early observations). The latter position is invariably used in this work. Power to the PMT is provided by a Heathkit variable power supply, modified by Earl Montgomery, which feeds a regulated transformer. The cathode voltage was either -1000 or -1200 volts, monitored at the transformer. A switch in the V preamplifier "crowbars" the power supply if the anode current exceeds an adjustable threshold value, usually a few microamperes. This crowbar switch unfortunately triggers sometimes when the viewing mirror motor turns on or off. The high voltage was always reset to within two volts of its previous value in these cases; the supply is also stable to about this level.

Output from the four preamplifiers is conducted along a shielded multiwire signal cable using a line driver and line receiver to reduce the output impedance, again built by Earl Montgomery. In early observations four coaxial cables were used. Because of concerns about noise and cross talk in the long (100 foot) cables, they were replaced by the line driver arrangement. Output is monitored at this point on one channel for focusing and centering, using a strip chart recorder and meter. The signal cable connects to four AC filters and amplifiers. The filters have a one Hz bandpass and are set to the chopping frequency. The amplifiers have selectable gain settings in multiples of ten up to 1000.

Next the signals are digitized and fed to a Z80 microcomoputer. Each channel has a sample and hold device which measures the output 32 times per chop cycle. The multiplexer then reads these sequentially into a 12 bit digitizer. The data rate for the Z80 is thus 640 samples per second (160 per channel), at a chopping rate of 5 Hz. The phase differences between the channels are corrected at the beginning of a night by telling the Z80 which of the 32 samples contains the peak counts for each channel. Output is ignored during the telescope's wobble motion.

The Z80 displays output either graphically in "oscilloscope" mode on an ADM-3 terminal, or as the integrated counts from one deflection on the teletype. The former method is useful in setting up and ensuring that the system is functioning, while the latter is preferred for a printed record of actual observations. The Z80 computes the mean and standard deviation of the deflection differences

at the end of each integration, which can be terminated by the observer at any time. "Spikes," or obviously spurious deflections can be removed at this time. Typically 10 to 20 deflection pairs, each requiring 30 seconds, are taken before checking the guiding. The longest integrations were about 100 deflection pairs, transpiring over approximately one hour.

Performance

For comparison with the predictions made in Chapter 2, the raw signal to noise measurements at the MMT for galaxies with redshifts near 0.5 and 1 are presented in Table IV(a). These were computed by dividing the mean by the standard deviation, and multiplying by the square root of the factor needed to make the integration time one hour. No other corrections were applied here. The full set of reduced data is the subject of Chapter 4.

The observed ratios vary widely, even for similar objects on the same night. But in general they are somewhat higher than predicted at H, lower at K and especially I_B, and about as predicted at V_B.

Because each individual observation can be subject to its own peculiarities (examples of which are discussed in Chapter 4), the observed performance was reevaluated in terms of limiting magnitudes, i.e. the magnitude which corresponds to a signal equal to the noise (standard deviation) after a one hour integration. These magnitudes are shown in Table IV(b). The noise levels were selected as the smallest typical values on integrations of 10 minutes or more under good

TABLE IV(a)

Observed Signal to Noise Ratios for Some High Redshift Galaxies

The S/N ratios shown below are from MMT observations normalized to a one hour integration.

Object	Redshift	V_B	I_B	H	K
3C200	0.458	32.8	20.1	76.6	33.4
13F	0.460	36.0	20.3	55.9	23.8
16betabeta	0.530	13.2	11.6	54.6	32.6
16KPNdelta	0.900	2.5	1.9	21.	5.4
3C280	0.996	7.3	2.8	15.5	8.5
3C356	1.079	3.4	1.9	7.8	3.9

TABLE IV(b)

Limiting Magnitudes Under Good Conditions at Three Telescopes

The limiting magnitude, referred to A0 stars as discussed in Chapters 2 and 4, corresponding to a signal to noise ratio of 1 after one hour integration is shown for each band. The MMT(Pd) entry is the prediction based on Table II. Also listed are the linear (not logarithmic) ratios of the sensitivities at the MMT and 90" to the sensitivity at the 61".

Telescope	V_B	I_B	H	K
61"	22.0	20.3	18.8	17.4
90"	22.6	21.5	19.4	18.0
MMT	24.3	23.2	21.1	19.5
MMT(Pd)	25.3	24.1	21.1	20.2
MMT/61"	8.3	14.	8.3	6.9
90"/61"	1.7	3.0	1.7	1.7

conditions on each telescope, and are calibrated in the SPIV instrumental magnitude system with reference to AO stars (see Chapter 4). The limiting magnitudes should therefore be representative of the best performance achievable with SPIV, and are more suited for comparison with the predictions made in Chapter 2 than the individual object S/N ratios of Table IV(a).

Also shown in Table IV(b) are the relative sensitivities of the MMT and 90" compared to the 61". The values are closely in accord with the predictions made in Table III for the background limited case in the V_B, H and K bands. I_B, however, appears to be detector noise limited. This is not surprising, because the calculations of Chapter 2 showed background and detector noise to be nearly equal for an optimal Si diode with the preamplifier design used.

The limiting magnitudes are brighter than predicted, except for H. This can be attributed to a combination of higher noise levels and/or lower transmissions and quantum efficiencies than were used in the prediction. There is good evidence that the Si diode is noisier than expected from Rieke et al. (1981), and the InSb diode for the K band is measurably noisier than that for H. For V_B, it seems likely the transmission and quantum efficiency are smaller than expected.

Another issue of concern is whether all four channels of SPIV are looking at the same point in the sky (see section on Alignment in Chapter 2). The fact of a common aperture goes far towards ensuring this, but it is still possible for the response across the aperture to vary widely from detector to detector. Figure 11 shows the relative output of the four bands from scanning the standard star HD84800 across
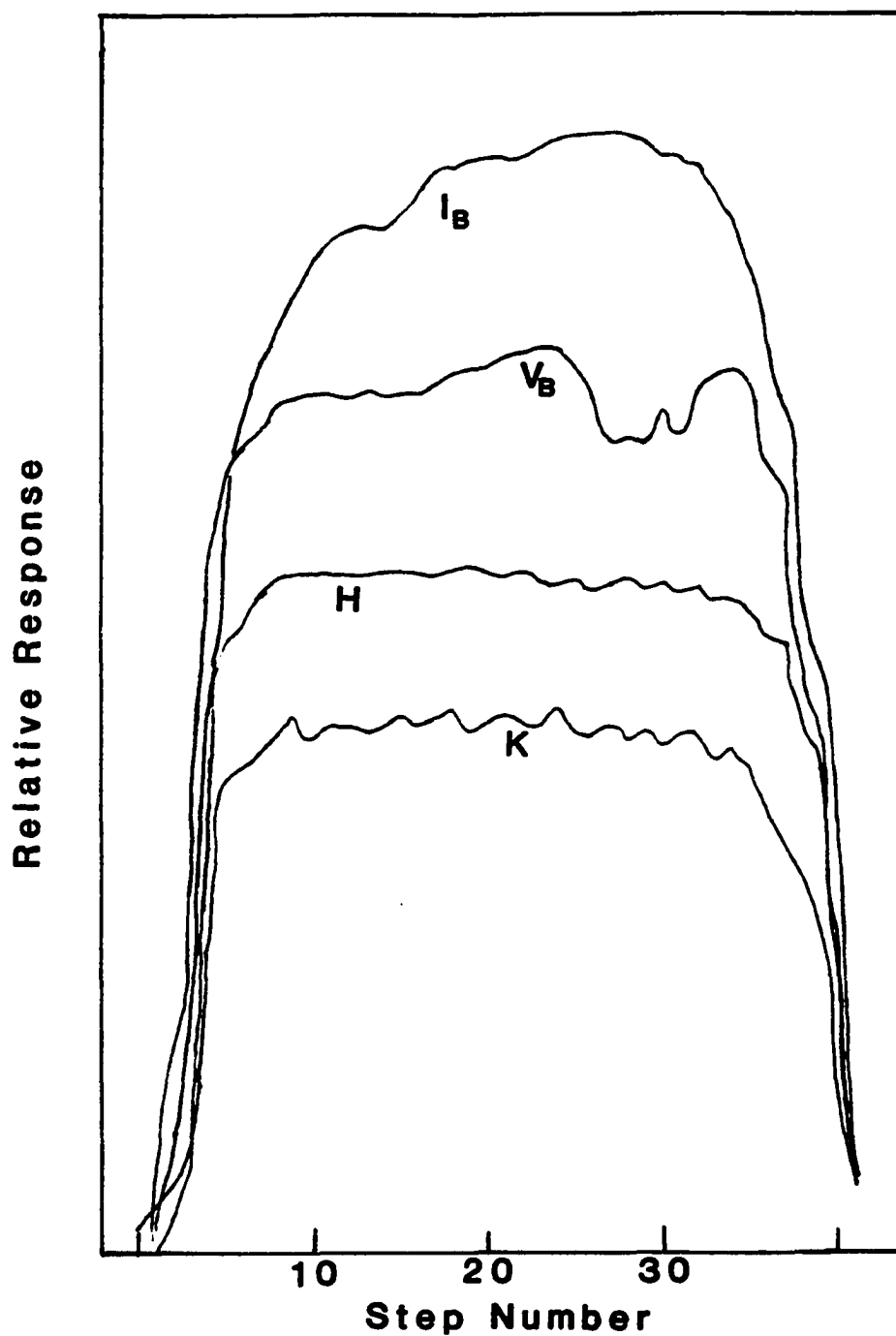
Figure 11. Observed Beam Profiles. The relative response of each of SPIV's four channels to a bright star scanned across the 2mm aperture.

the 2mm (20 arcsecond) aperture at the 61". The profiles were produced by a series of 50 0.7 arcsecond steps and 1.3 second integrations across the center of the aperture. Figure 11 illustrates several things:

1) The four beam profiles are aligned to within 10% of the aperture size.

2) The profiles are flat to within 20% across the aperture, with most of the variation at the edges. The least flat profile is I_B, as expected from Table I and Figure 8.

3) The images are well focused, as indicated by the steep sides of the profiles.

In summary, SPIV performs at design goals in many respects, and does not fall far short in the remainder. The greatest room for improvement is in the I_B channel.

Observing Sessions

Observations presented in this dissertation were made on eleven nights at the MMT on Mt. Hopkins, three nights at the UAO 90" on Kitt Peak, and three nights at the UAO 61" on Mt. Bigelow. These nights, and the various minor variations in equipment used, are listed in Table V. No useful observations were made at V_B on June 23/24 1983. Observations made on Oct. 31/Nov.1 1983 at the MMT, Nov. 28/29 1983 and Jan. 3/4 1984 at the 61", and Jan. 25/26 1984 at the 90" are not presented because of problems with equipment or observing conditions. Data from several "engineering" runs in the first part of 1983 is also not presented. The poor seeing referred to in Table V for the Feb. 1984 MMT nights was approximately two arcseconds, poor only for the MMT. I was present for

TABLE V

Observing Sessions

PMT refers to voltage on photomultiplier, V_B tells whether or not the UV blocking filter was used, and Cables indicates whether the initial (old) cable arrangement of 4 separate coaxial cables, or the (new) multiwire line driver was used. The letter code for each date is used in Table VI.

	Date			Tel	PMT	V_B	Cables	Comments
A	June 1/2	1983		MMT	1000	open	old	
B	June 2/3	1983		MMT	1000	open	old	
C	June 23/24	1983		MMT	1200	open	old	
D	June 24/25	1983		MMT	1200	open	old	
E	June 25/26	1983		MMT	1200	open	old	
F	June 26/27	1983		MMT	1200	open	old	
G	June 27/28	1983		MMT	1200	open	old	
H	Sept 26/27	1983		90"	1000	open	new	
I	Sept 27/28	1983		90"	1000	open	new	clouds at end
J	Nov 29/30	1983		61"	1200	open	new	
K	Dec 5/6	1983		61"	1200	open	new	
L	Jan 24/25	1984		90"	1200	UV	new	
M	Feb 23/24	1984		MMT	1200	UV	new	
N	Feb 24/25	1984		MMT	1200	UV	new	
O	Feb 25/26	1984		MMT	1200	UV	new	seeing poor
P	Feb 26/27	1984		MMT	1200	UV	new	seeing,clouds,closed
Q	Mar 5/6	1984		61"	1200	UV	new	

all the nights listed except for June 26/27 1983. The focal ratio was f/13.5 at the 61" and f/9 at the other telescopes. Typically five standard stars and ten to fifteen objects were observed per night. The standards are discussed in Chapter 4.

The galaxies observed, along with their (epoch 1950) positions, redshifts and references are listed in order of right ascension in Table VI. Positions were obtained using the KPNO two axis Grant machine, using nearby SAO stars as reference points. Solutions for the positions were generally accurate to 0.5 arcseconds. When possible, measurements were made off of the KPNO glass copy of the Palomar sky survey. The non-radio galaxies too faint to appear on the sky survey were measured by Marcia Rieke on their discovery plates (see below), while positions for extremely faint radio galaxies were taken from the references in Table VI. Radio galaxies have reference numbers from 1 to 6, while objects with reference numbers greater than 6 are non-radio galaxies. The galaxy sample is discussed in Chapter 5.

TABLE VI

First Ranked Cluster and Radio Galaxies Observed

An asterisk indicates a note about the object. Date lists the letter
code(s) from Table V for the night(s) the object was observed.

Object	RA(1950)	Dec(1950)	Redshift	Ref	Date
A21	0:18:18.07	28:21:38.7	0.095	10	H
4C25.04	1:08:40.66	25:49:49.2	0.066	6	J
3C42	1:25:42.67	28:47:30.4	0.395	2	H
4C31.07	1:58:01.56	31:33:01.9	0.175	6	H
A399	2:55:08.66	12:49:51.4	0.073	10	I
0308.5+1642	3:08:25.10	16:41:59.4	0.260	9	H
4C39.12	3:31:01.30	39:11:25.0	0.021	6	J
3CR98	3:56:10.25	10:17:32.9	0.031	2	J
A553	6:08:51.65	48:36:31.3	0.067	7	KQ
4C26.23	6:32:29.53	26:19:07.2	0.040	6	J
A568	7:05:00.87	35:03:58.2	0.078	10	L
A569	7:05:21.76	48:41:47.4	0.019	7	LQ
4C28.18	7:14:48.03	28:40:35.5	0.083	6	K
3C184	7:33:59.01	70:30:01.1	0.994	1	MN
4C30.14	8:05:09.86	30:55:29.0	0.301	6	LO
3CR197.1	8:18:00.92	47:12:11.3	0.130	2	Q
0822+67	8:22:19.34	67:56:40.7	0.384	8	M
3C200	8:24:21.43	29:28:42.2	0.458	2	M
A671	8:25:26.37	30:35:51.7	0.050	7	Q
3C217	9:05:41.42	38:00:29.9	0.890	3	OP
4C36.14	9:22:34.20	36:40:04.9	0.112	6	JQ
3CR223.1	9:38:18.23	39:58:23.5	0.108	2	MQ
0938-01	9:38:49.98	-01:29:20.2	0.382	6	O
3C225B	9:39:32.21	13:59:33.3	0.580	3	P
*A868	9:42:58.25	-08:25:16.5	0.154	8	K
3C228	9:47:27.63	14:34:02.5	0.520	3	P
9sigma	9:48:24.63	46:53:30.5	0.430	11	M
0948.9+4426	9:48:53.13	44:27:39.7	0.361	9	M
0949.9+4409	9:49:47.92	44:09:37.1	0.385	9	LN
9C114	9:50:46.77	45:53:50.0	0.410	11	M
3C241	10:19:09.44	22:14:40.7	1.617	4	P
1021.1+0427	10:21:03.76	04:26:22.3	0.286	9	L
3C244.1	10:30:19.65	58:30:04.7	0.428	1	M
4C30.19	10:37:42.79	30:13:38.7	0.093	6	Q
1049.4-0904	10:49:24.70	-09:03:36.0	0.330	9	N
4C37.29	11:07:04.48	37:54:47.4	0.346	6	O
3C252	11:08:48.93	35:57:00.1	1.105	4	OP
A1246	11:21:20.69	21:45:15.4	0.216	8	L
*1134+015	11:34:55.63	01:32:50.6	0.430	6	O
1153+2341	11:53:27.20	59:03:47.2	0.143	7	L
3C268.3	12:03:54.28	64:30:18.6	0.371	2	N

TABLE VI--<u>Continued</u>

3C274.1	12:32:56.76	21:37:05.7	0.422	2	M
3C277.3	12:51:46.29	27:53:49.5	0.086	2	L
1253+4422	12:53:22.75	44:21:41.4	0.198	7	F
3C280	12:54:41.66	47:36:32.7	0.996	1	ABM
1304+3110	13:03:28.28	31:10:19.8	0.183	7	FLO
13KPNgamma	13:22:01.79	30:28:38.0	0.690	11	DEN
13KPNalpha	13:22:28.99	30:27:15.5	0.750	11	DO
13F	13:29:33.54	32:19:12.5	0.460	11	EM
A1759	13:31:39.39	20:30:43.9	0.168	8	L
3C289	13:43:27.38	50:01:32.0	0.967	4	MN
1431+3146	14:30:29.81	31:52:04.1	0.131	7	Q
1446+26G2	14:47:17.62	26:20:16.4	0.370	9	EM
CrB Cl .1	15:20:17.35	27:53:31.8	0.072	9	Q
1534+3748	15:34:26.53	37:48:29.4	0.153	7	Q
16betabeta	16:01:32.39	42:53:36.9	0.530	11	AN
16KPNdelta	16:02:45.88	43:12:58.6	0.900	11	CE
16KPNepsilon	16:02:54.92	43:28:59.5	0.920	11	C
16KPNmu	16:03:41.96	42:57:06.0	0.610	11	AB
1604.0+3935	16:04:51.24	39:35:34.7	0.235	9	BFN
1607.6+3953	16:07:40.67	39:52:30.9	0.280	9	AN
3C330G2	16:09:14.83	66:04:30.1	0.530	2	FNO
1610.8+4115	16:10:55.41	41:13:49.3	0.300	9	AN
1612.6+4204	16:12:35.34	42:03:39.7	0.275	9	FN
1613+31	16:13:48.39	31:04:40.7	0.415	9	BF
3C337	16:27:18.41	44:25:35.7	0.630	3	DE
3C340	16:27:30.17	23:26:45.7	0.760	3	FN
3C343.1	16:37:55.16	62:40:33.8	0.750	2	AB
3C356	17:23:06.66	51:00:18.2	1.079	1	CDEG
3C368	18:02:45.60	11:01:13.8	1.132	1	F
A2320	19:16:48.95	70:50:41.8	0.170	8	GI
3C427.1	21:04:45.12	76:21:07.3	1.175	5	ABE
3C436	21:41:57.94	27:56:30.0	0.215	2	FG
A2397	21:53:35.47	01:09:11.6	0.222	8	G
3C438	21:53:45.46	37:46:12.3	0.290	2	GI
21KPNsigma	22:01:31.69	02:58:15.6	0.640	11	CD
4C39.72	23:03:43.88	39:11:07.1	0.206	6	H
A2634south	23:35:58.84	26:45:18.4	0.031	9	H
3C465F	23:37:30.60	26:51:25.0	0.031	6	J

References:

1. Spinrad (1982)
2. Smith and Spinrad (1980)
3. Spinrad (1984)
4. Spinrad et al. (1984)
5. Spinrad et al. (1981)
6. Burbidge and Crowne (1979)

7. Sandage (1972b)
8. Kristian et al. (1978)
9. Gunn and Oke (1975)
10. Hoessel (1980)
11. Gunn (1980)

*A868 has reference beam problem, 1134+015 is a Parkes radio source.

CHAPTER 4

REDUCTION AND CALIBRATION

Because of the nonstandard nature of the instrument response function (IRF), calibration to a standard magnitude system (e.g. the Johnson system) is complicated, particularly for the very broad V_B and I_B bands. At least two general approaches are possible: a multilinear regression fit relating the standard system to the SPIV instrumental system; and a spectral modelling procedure where monochromatic fluxes are derived by assuming a spectrum for the object. Both of these approaches are used, but the emphasis in this dissertation is on using results in the SPIV instrumental system. Instrumental magnitudes have the advantage of not requiring modelling or extrapolation beyond the color range available from standards in a regression fit.

Another basic issue is whether to reduce observations in terms of magnitudes in each band, or in ratios of these bands (color indices - hereafter simply called colors). Because SPIV measures its four bands simultaneously and through the same aperture, the colors should be reliable, more so than the magnitudes. For this reason, and because this dissertation is primarily concerned with color evolution, the reduction was carried out in colors referred to the H magnitude. H is preferred for three reasons:

1) The standard elliptical galaxy spectrum, Figure 1, peaks in this band.

2) The signal to noise ratio is empirically best for SPIV's H band. Objects were always detected in the H band, which is not true for the other bands.

3) H is the most standard of SPIV's four channels, with no transformation required between instrumental and standard H magnitudes.

4) The K correction (see Chapter 5) is smallest for H. Coincidentally, H also happens to be the "straight shot" band in SPIV. (see Figure 2).

The reduced observations on the SPIV instrumental system, arranged in order of redshift, are shown in Table VII. The colors have been corrected for atmospheric and galactic extinction, and for the effect of the UV blocking filter in the case of V_B-H. The H magnitudes have also had the aperture and chopping corrections applied. In a few cases where an object was not detected in one or more bands, two sigma lower limits (for V_B-H and I_B-H) or upper limits (H-K) are shown; these are indicated by a value of -1 for the uncertainty. The uncertainties and corrections are discussed in detail below.

Instrumental System

To define what I mean by instrumental magnitudes and colors, the following terminology will be helpful:

^{o} appearing as a superscript refers to an object (galaxy).

* similarly refers to a standard star.

^{AO} refers to an AO standard star.

$_x$ as a subscript refers to a SPIV instrumental filter.

$_{x'}$ similarly refers to a standard system filter.

TABLE VII

Reduced Observations in SPIV Instrumental System

Colors and H magnitudes, along with their associated uncertainties (σ), were calculated as described in the text. A σ of -1. indicates a two sigma upper (H-K) or lower (V_B-H, I_B-H) limit. N is the number of times the object was observed.

Object	Redshift	N	V_B-H	σ	I_B-H	σ	H	σ	H-K	σ
A569	0.019	2	3.33	0.05	2.31	0.03	9.42	0.02	0.29	0.01
4C39.12	0.021	1	2.98	0.07	1.84	0.05	9.04	0.05	0.32	0.02
3C465F	0.031	1	3.63	0.08	2.14	0.06	9.71	0.05	0.29	0.02
3CR98	0.031	1	3.30	0.08	2.09	0.06	11.07	0.05	0.35	0.03
A2634south	0.031	1	3.42	0.05	2.87	0.07	10.05	0.01	0.34	0.02
4C26.23	0.040	1	3.31	0.08	1.74	0.06	11.40	0.05	0.26	0.05
A671	0.050	1	3.51	0.08	2.30	0.05	11.32	0.03	0.37	0.02
4C25.04	0.066	1	2.66	0.13	1.80	0.14	13.67	0.08	0.49	0.12
A553	0.067	2	3.18	0.04	1.98	0.03	11.86	0.02	0.42	0.02
CrB Cl .1	0.072	1	3.41	0.08	1.95	0.06	12.52	0.03	0.38	0.03
A399	0.073	1	3.47	0.04	2.91	0.07	12.28	0.02	0.45	0.04
A568	0.078	1	3.16	0.07	2.55	0.04	12.54	0.02	0.32	0.03
4C28.18	0.083	1	3.02	0.07	2.05	0.07	12.92	0.05	0.40	0.07
3C277.3	0.086	1	3.30	0.07	2.66	0.06	13.11	0.02	0.40	0.02
4C30.19	0.093	1	3.04	0.08	2.01	0.06	13.21	0.03	0.39	0.04
A21	0.095	1	3.40	0.09	2.94	0.10	12.66	0.05	0.51	0.07
3CR223.1	0.108	1	3.41	0.08	2.25	0.09	13.60	0.04	0.66	0.05
4C36.14	0.112	2	3.34	0.06	2.12	0.04	12.91	0.03	0.54	0.03
4C-04.17	0.118	1	3.99	0.14	2.20	0.10	14.12	0.05	0.47	0.08
3CR135	0.127	2	2.88	0.07	1.94	0.06	14.60	0.03	0.60	0.07
3CR197.1	0.130	1	3.45	0.11	1.80	0.09	14.68	0.05	0.43	0.10
1431+3146	0.131	1	3.54	0.08	1.81	0.06	13.37	0.03	0.48	0.05
1153+2341	0.143	1	3.60	0.07	2.63	0.03	12.72	0.02	0.52	0.02
1534.4+3748	0.153	1	3.30	0.14	1.78	0.10	14.25	0.06	0.82	0.07
A868	0.154	1	2.65	0.07	2.26	0.09	13.58	0.06	0.60	0.08
A1759	0.168	1	3.82	0.09	2.66	0.06	14.13	0.03	0.56	0.04
A2320	0.170	2	3.57	0.04	3.21	0.06	13.04	0.02	0.34	0.02
4C31.07	0.175	1	3.32	0.09	2.44	0.06	14.78	0.03	0.71	0.10
1304+3110	0.183	2	3.44	0.04	3.23	0.06	13.94	0.03	0.59	0.03
1253+4422	0.198	1	3.58	0.13	2.36	0.13	15.41	0.06	0.85	0.05
4C39.72	0.206	1	3.46	0.12	3.17	0.11	15.17	0.03	0.74	0.09
3C436	0.215	2	3.22	0.10	3.31	0.11	15.43	0.07	0.83	0.07
A1246	0.216	1	3.63	0.08	2.70	0.05	13.75	0.03	0.60	0.03
A2397	0.222	1	3.65	0.08	2.33	0.07	13.95	0.02	0.63	0.02
1604.0+3935	0.235	3	3.31	0.03	3.22	0.05	15.17	0.02	0.62	0.02
0308.5+1642	0.260	1	3.81	0.20	2.16	0.07	15.10	0.03	0.91	0.07
1612.6+4204	0.275	2	3.70	0.06	3.47	0.11	15.91	0.03	0.70	0.05
1607.6+3953	0.280	2	3.27	0.05	3.17	0.07	15.74	0.03	0.78	0.05
1021.1+0427	0.286	1	3.40	0.10	2.43	0.07	14.92	0.05	0.72	0.08

TABLE VII--<u>Continued</u>

3C438	0.290	1	3.97	0.18	3.51	0.10	14.84	0.02	0.80	0.04
1610.8+4115	0.300	2	4.04	0.09	3.38	0.06	15.45	0.02	0.74	0.03
4C30.14	0.301	2	3.81	0.09	2.57	0.09	16.05	0.03	0.13	0.08
1049.4-0904	0.330	1	3.85	0.08	3.18	0.11	15.45	0.05	0.73	0.06
4C37.29	0.346	1	3.88	0.14	3.31	0.25	16.61	0.06	0.74	0.11
0948.9+4426	0.361	1	4.28	0.08	3.04	0.10	15.72	0.02	0.66	0.06
1446+26G2	0.370	2	4.24	0.09	3.17	0.13	16.27	0.03	0.82	0.03
3C268.3	0.371	1	4.59	0.13	4.26	0.36	16.32	0.04	1.00	0.06
0938-01	0.382	1	4.63	0.16	3.07	0.13	16.19	0.05	0.77	0.07
0822+67	0.384	1	4.52	0.09	3.38	0.11	15.87	0.02	0.81	0.06
0949.9+4409	0.385	2	4.43	0.09	3.19	0.11	15.68	0.03	0.76	0.04
3C42	0.395	1	4.34	0.24	2.88	0.10	15.96	0.04	0.83	0.11
9C114	0.410	1	4.03	0.08	3.16	0.11	16.19	0.03	0.69	0.07
1613+31	0.415	2	3.81	0.05	4.22	0.17	16.21	0.04	0.71	0.07
3C274.1	0.422	1	4.67	0.11	3.54	0.15	16.08	0.03	0.75	0.05
3C244.1	0.428	1	4.07	0.08	3.07	0.10	15.99	0.04	0.61	0.07
1134+015	0.430	1	3.12	0.10	2.97	0.11	15.48	0.04	0.87	0.05
9sigma	0.430	1	4.63	0.11	3.62	0.15	16.25	0.03	0.58	0.07
3C200	0.458	1	4.35	0.08	3.35	0.11	15.97	0.03	0.75	0.06
13F	0.460	2	3.18	0.07	3.11	0.09	16.59	0.03	0.72	0.11
3C228	0.520	1	4.44	0.28	3.40	0.40	17.43	0.10	0.82	0.13
16betabeta	0.530	2	5.00	0.15	3.68	0.10	16.43	0.02	0.66	0.05
3C330G2	0.530	3	4.45	0.11	3.53	0.11	16.40	0.04	0.74	0.06
3C225B	0.580	1	4.51	0.27	3.02	0.23	17.14	0.09	0.53	0.15
16KPNmu	0.610	3	3.22	0.07	3.22	0.14	17.30	0.04	0.78	0.08
3C337	0.630	2	3.22	-1.00	3.07	0.21	18.06	0.08	0.62	-1.00
21KPNsigma	0.640	3	2.66	-1.00	3.30	0.22	17.29	0.05	1.11	0.15
13KPNgamma	0.690	3	5.30	0.18	3.41	0.12	17.05	0.03	0.66	0.08
13KPNalpha	0.750	2	4.82	0.29	3.21	0.14	17.02	0.04	0.72	0.08
3C343.1	0.750	2	3.32	0.08	3.82	0.19	17.32	0.06	0.71	0.14
3C340	0.760	2	3.13	0.07	2.65	0.09	16.57	0.04	0.05	0.11
3C217	0.890	2	3.26	0.51	2.60	0.85	19.13	0.35	0.72	0.63
16KPNdelta	0.900	2	3.97	0.42	2.25	-1.00	17.93	0.06	1.11	0.17
16KPNepsilon	0.920	1	1.04	-1.00	1.47	-1.00	19.80	0.59	2.40	-1.00
3C289	0.967	2	5.27	0.46	4.42	0.71	17.88	0.06	0.96	0.11
3C184	0.994	2	4.53	0.22	3.31	0.30	17.70	0.06	0.80	0.12
3C280	0.996	3	3.72	0.09	3.47	0.20	17.70	0.05	0.93	0.12
3C356	1.079	4	3.20	0.22	3.54	0.48	18.48	0.06	1.35	0.16
3C252	1.105	2	2.80	0.33	2.19	0.46	18.74	0.30	0.84	0.49
3C368	1.132	1	3.22	0.36	2.35	0.18	17.92	0.12	0.85	0.22
3C427.1	1.175	3	3.51	-1.00	3.70	0.24	17.11	0.03	0.70	0.09
3C241	1.617	1	4.76	0.40	3.45	-1.00	18.06	0.15	-.05	0.33

S is the observed signal.

m is the apparent magnitude.

F is the photon number flux per unit wavelength.

R is the combined atmospheric/SPIV system response function.

$\emptyset$ is the IRF of Figure 3.

For example, $m_{x'}^*$ is the magnitude of a standard star in the standard system filter x'. The instrumental magnitude of an object is given by:

$$m_X^O = -2.5 \log \frac{S_X^O}{S_X^*} + m_X^*$$ 4.1

or, substituting for S_X^O and S_X^* from equation 2.4:

$$m_X^O = -2.5 \log \frac{\int F^O R_X d\lambda}{\int F^* R_X d\lambda} + m_X^*$$ 4.2

The response function R will in general be a function of time, wavelength, and position in the sky. I will make the simplifying assumption that these dependences are separable, and postpone discussion of the position variation to the section on extinction below. Then:

$$R_X(\lambda, t) = r(t)\emptyset_X(\lambda)$$ 4.3

where r(t) represents the time variation in R. Substituting in 4.2:

$$m_X^O = -2.5 \log \frac{\int F^O \emptyset_X d\lambda}{\int F^* \emptyset_X d\lambda} \frac{r(t^O)}{r(t^*)} + m_X^*$$ 4.4

If $r(t^O)$ and $r(t^*)$ are equal, these terms vanish. If there is a long interval between t^O and t^*, this may not be true, unless r is changing very slowly (i.e. the night is photometric). If we consider the difference between two magnitudes at x and y we have:

$$m_x^0 - m_y^0 = -2.5 \log \frac{\int F^0 \phi_x d\lambda}{\int F^* \phi_x d\lambda} \frac{\int F^* \phi_y d\lambda}{\int F^0 \phi_y d\lambda} \frac{r(t^0)}{r(t^*)} \frac{r(t^*)}{r(t^0)} + m_x^* - m_y^*$$

$$= -2.5 \log \frac{\int F^0 \phi_x d\lambda}{\int F^0 \phi_y d\lambda} \frac{\int F^* \phi_y d\lambda}{\int F^* \phi_x d\lambda} + m_x^* - m_y^* \qquad 4.5$$

which is independent of time if equation 4.3 is true, because bands x and y are measured simultaneously. This is the justification for the statement made above that colors are more reliable than magnitudes.

Standards

The problem with equations 4.3 and 4.5 is that we know the standard star magnitude m^* in the standard system x', not the instrumental system x. If we define standard and instrumental magnitudes to be equal for A0 stars:

$$m_x^{A0} \equiv m_x^{A0'} \qquad 4.6$$

it follows from equation 4.1 that the relation between the standard magnitudes in the instrumental and standard systems is:

$$m_x^* \equiv -2.5 \log \frac{s_x^*}{s_x^{A0}} + m_x^{A0'} \qquad 4.7$$

Standard stars were taken from Elias et al. (1982) and Moffett and Barnes (1979). They fall into two classes: Primary standards of spectral type A0 or A2 and (Johnson) J-K < 0.125 whose listed magnitudes require little or no change to be used as instrumental magnitudes; and secondary standards of widely varying color (up to J-K = 0.98) which were observed at least twice and whose instrumental magnitudes were found using equation 4.7.

Primary Standards

The 14 primary standards are Draper catalogue (HD) stars with JHK photometry and positions from Elias et al. (1982). Somewhat surprisingly, only one of these (HD105601) has photoelectric visual photometry published in the USNO compendium (Blanco et al. 1968). Least squares linear regressions based on this star and the colors listed in Johnson (1966) for spectral types B7 through A7 suggested the relations $V-K = 4(J-K)$ and $I-K = 2.5(J-K)$ should be accurate to better than 0.1 magnitudes for the small range of J-K covered by the primary standards. These values for V and I were adopted for V_B and I_B, together with the published H and K values.

Secondary Standards

Using the primary standard instrumental magnitudes, corrected for extinction (see below), the zero points for each color $(V_B-H, I_B-H, H-K)$ and the H magnitude were calculated for each of the 17 nights in Table V by averaging over the primary standards measured on that night. These zero points were applied to the remaining (secondary) standards, again corrected for extinction. The secondary instrumental magnitudes were then determined by averaging the individual values from each night. In both of these averaging steps some observations were excluded if they disagreed sharply with the other observations relevant to the quantity being averaged. The disagreement was virtually always found to be attributable to either saturation of the 12 bit digitizer, or poor observing conditions at the beginning or end of a night. Secondary standards with only one reliable measurement were discarded.

TABLE VIII

SPIV Instrumental Standards

Primary (HD) standards are listed first. N is the number of observations used to derive the secondary standard colors and H magnitudes. Standards are from Elias et al. (1982) and Moffett and Barnes (1979).

Name	N	V_B-H	I_B-H	H	H-K
HD1160		0.06	0.04	7.05	0.01
HD18881		-.04	-.02	7.13	-.00
HD22686		0.04	0.02	7.19	0.01
HD40335		0.34	0.21	6.47	0.02
HD44612		0.09	0.06	7.04	0.00
HD77281		0.28	0.17	7.05	0.02
HD84800		0.12	0.08	7.53	0.00
HD105601		0.67	0.29	6.72	0.03
HD106965		0.22	0.13	7.34	0.02
HD129653		0.22	0.13	6.94	0.02
HD136754		0.07	0.04	7.13	0.00
HD162208		0.39	0.23	7.15	0.04
HD201941		0.29	0.17	6.64	0.02
HD203856		0.24	0.14	6.88	0.02
093-103	2	2.57	1.28	6.32	0.15
096-615	3	2.48	1.25	7.01	0.15
099-296	2	2.62	1.24	5.97	0.15
100-607	2	1.24	0.68	8.78	0.06
102-276	3	1.19	0.77	8.74	0.05
106-863	3	1.31	0.80	9.28	0.06
107-998	6	1.51	0.83	8.92	0.08
108-984	2	1.29	0.72	9.06	0.06
109-537	2	1.59	0.73	8.76	0.09
111-2009	2	2.09	1.14	8.57	0.05
113-466	3	1.10	0.65	8.79	0.05
115-273	4	1.46	0.80	8.62	0.05
G77-31	2	5.97	2.45	8.22	0.30
Gl105.5	2	3.00	1.40	6.63	0.13
Gl299	3	4.94	2.01	7.97	0.26
Gl406	3	6.98	2.80	6.52	0.35

Because of their importance in determining the SPIV instrumental system, the 16 secondary and 14 primary standards are listed with their adopted instrumental colors and H magnitudes in Table VIII.

Reduction

Extinction

The position variation in R mentioned above is more commonly known as extinction. This is a particular problem for V_B because extinction increases rapidly towards the ultraviolet, and because the band is so broad ($\Delta\lambda/\lambda_{eff} > 0.5$ -- see equation 2.1 and Figure 3). It was for this reason that the UV blocking filter was added to V_B.

No attempt was made to derive empirical extinction coefficients from the standard star observations. A check of the June 1983 standard observations showed a rough correlation in the expected sense, but the scatter was so large that the coefficients were very uncertain. Instead mean extinction coefficients were used. These were taken from Hayes (1982) for V_B and I_B, and from Lebofsky (1984) for H and K. The coefficients adopted were 0.05 mag/airmass for I_B, and 0.1 for H and K.

Extinction for V_B. The Hayes coefficients are monochromatic and cover from 0.32 to 0.84 microns, so the dependence of the V_B extinction correction on airmass and spectral shape could be calculated by numerical integration over the IRF. A linear airmass correction proved to be within one percent of the integrated values up to airmasses of two, but the coefficient does depend on the spectrum. The very red galaxy of Figure 1 has a coefficient about .05 mag/airmass smaller than does an AO star, a value which changes only slightly with redshift. The

UV blocking filter lowers the coefficient slightly. The adopted coefficients are: 0.21 mag/airmass (0.19 with the UV blocking filter) for the standard stars, and 0.05 mag/airmass less for the galaxies.

Zero points

With the extinction correction applied, the zero points for each color and night were again solved for, this time using the full set of thirty instrumental standards. The difference between these zero points and those calculated using the primary standards alone was typically less than 0.03 magnitudes, but the larger number of standards allowed the standard deviations for each color and night to be calculated. These zero points were used to calculate the object colors, and the standard deviations were added quadratically to those calculated from the integrations for each observation. The average over all nights of σ^2 gives the following typical standard deviations (in magnitudes): V_B-H: 0.06; I_B-H: 0.06; H: 0.03; H-K: 0.012. No useful V_B observations were made on June 23/24 1983, and on June 1/2, 1983 and June 24/25, 1983 only one standard was observed at V, so the uncertainty in V_B-H for these nights could not be calculated. The night of Feb. 26/27 1984 had unusually discrepant standards at V_B (though not in the other bands) and so was not included in the typical uncertainty calculation; with this night, the value rises to 0.08 for V_B-H.

Correction for UV blocking filter

The UV blocking filter affects standard and galaxy V_B magnitudes differently, because relatively more of a standard's flux is eliminated by the filter. There will therefore be a systematic <u>overestimation</u> of

the galaxy flux **with** the filter as compared to the same observation made without the filter. To put all V_B magnitudes on the "open" (no UV blocking filter) system, the following correction was calculated:

$$m^O_{open} - m^O_{uv} = -2.5 \log \frac{\int \phi_{open} F^O(z) d\lambda}{\int \phi_{open} F^{AO} d\lambda} \frac{\int \phi_{uv} F^{AO} d\lambda}{\int \phi_{uv} F^O(z) d\lambda} \qquad 4.8$$

where the subscripts uv and open refer to the V_B band, with and without the UV blocking filter, respectively. F^O was taken from Figure 1, appropriately redshifted, and F^{AO} was provided by Djorgovski (1984). Although this correction changes by 0.08 mag between z = 0 and 0.5, it is clear from the discussion in Chapter 5 that Figure 1 is not correct for z > 0.5 in the V_B band. Therefore an average value (0.175 mag) was added to the V_B-H color for all galaxies observed with the UV blocking filter. This value should be within 0.04 mag of the true correction.

Aperture Correction

Giant elliptical galaxies are clearly extended objects, therefore, the measured flux of one depends on the size of the measuring aperture and on the angular size of the galaxy. The angular size is a function of z and q_0, so attempting to determine q_0 by measuring magnitudes as a function of redshift is a convoluted process. The color (index) of a galaxy depends very little on the aperture, however (Frogel et al. 1978), another advantage of using colors rather than magnitudes.

The aperture correction was found by fitting a polynomial to Sandage's (1972a) curve of growth for giant ellipticals. When referenced to a standard metric diameter of 32 kpc/h, where h is Hubble's constant in km/sec/Mpc over 100, the correction (in magnitudes) is given by:

$$m(32kpc/h) - m(\theta, q_0, z) = -0.356 + 1.265f - 0.760f^2 + 0.296f^3 \quad 4.9$$

$$f = \log \left[\frac{\theta \, q_0 z + (q_0 - 1)[(1 + 2q_0 z)^{1/2} - 1]}{q_0^2 (1 + z)^2} \right]$$

This polynomial is accurate to better than 1% over the range of Sandage's growth curve. Here θ is the measuring aperture in arcseconds. The quantity in large brackets is just $\theta H_0 R_0 r/c(1 + z)$, where $R_0 r$ is given by equation 2.3, and is equal to the metric diameter if θ is in radians. A useful aproximation for this quantity, found by expanding $(1 + 2q_0 z)^{1/2}$ for small $q_0 z$ is:

$$10^f = \frac{\theta z}{(1+z)^2}[1 + 0.5z(1-q_0)(1-q_0 z)] \quad 4.10$$

which is accurate to $5q_0^2 z^4/24$. For $q_0 = 0$, 32 kpc/h corresponds to a 7 arcsec aperture (MMT observations) at $z = 0.64$, or to 20 arcsec (61" and 90" observations) at $z = 0.13$. For $q_0 = 1/2$, the maximum metric size corresponding to 7 arcsec is about 30 kpc/h near $z = 1.2$, while 20 arcsec = 32 kpc/h for $z = 0.14$.

I chose $q_0 = 1/2$ and the 32 kpc standard diameter in applying equation 4.9 to the observations for consistency with earlier work (e.g. Lebofsky and Eisenhardt 1984, Lebofsky 1981), and because the inflationary universe models predict $q_0 = 1/2$. The difference in the aperture correction at $z = 1$ for $q_0 = 1$ and $q_0 = 0$ is 0.15 mag, so my corrections should be within about 0.08 mag of the true values. The size of the correction, which was applied only to the H magnitudes, not to the colors, ranged from -1.07 to +0.22 magnitudes.

Chopping Correction. Closely related to the aperture correction is a correction for flux subtracted from the signal because it appears

in the reference beam. Because the reference beam is only one aperture diameter away from the object beam, this correction can be appreciable. The subtracted flux was approximated by considering a ring of outer diameter 3Θ and inner diameter Θ. Equation 4.9 was used to calculate the flux in this ring, and this was divided by eight since the reference beam covers one eighth the area of the ring. Although the rigorously correct procedure would be to integrate the reference beam over the growth curve, the size of this correction does not justify such a complicated approach. The chopping correction (again applied only to the H magnitude) consistently increased the flux by about 5%, except for very low redshift galaxies, where it was as large as -0.13 magnitudes.

Consistency of Multiply Observed Objects

Once the aperture and chopping corrections were applied, the individual color and H magnitude observations, weighted by their standard deviations, were averaged together for objects observed more than once. There were 37 such objects, including 4 which were second or third ranked in a cluster, and they were observed from two to four times, in some cases using two different telescopes. The standard deviations included the uncertainty in zero point for the particular night and color involved.

In most cases the agreement between two different observations of the same object was consistent with the errors. There were several cases, however, where the individual points disagreed in the sense that the quantity:

$$\frac{\Sigma \left[\dfrac{m_i - m}{\sigma_i}\right]^2}{N}$$

was greater than 9, where N is the number of individual observations m_i with standard deviations σ_i, and m is the weighted mean. Because equation 4.11 is a squared quantity, this criterion is analagous to a three sigma limit, although the concept of sigma is not very meaningful here as N is at most 4. The discrepant objects are:

V_B-H: 1604.0+3935, 1607.6+3953, 1612.6+4204, 16KPNmu.

I_B-H: 1304+3110, 1604.0+3935, 1610.8+4115, 3CR223.1, A569.

H: 1610.8+4115, 16KPNdelta, 3CR223.1, 3C330G2, 3C427.1, 4C30.14

No objects had equation 4.11 as great as 3 for H-K, although 1604.0+3935 was somewhat discrepant in all bands. The discrepancy was worst for 3CR223.1, which was observed on the 61" and on the MMT. Because there was some question at the MMT whether the correct object was observed, the MMT observation was discarded.

The discrepant observations are most likely the result of systematic errors, either associated with the equipment or the object. There was some concern in the early observing runs about crosstalk between channels, which is why the coaxial cables were replaced by the line driver arrangement in September 1983 (see Table V and section on Detection in Chapter 3). To check if the June 1983 MMT observations were systematically different from the others, the data were reanalyzed without these observations. Unfortunately, this eliminated most of the multiple observations, so it was difficult to assess the effect on equation 4.11, although that parameter was on average smaller. However,

the restricted data set showed negligible differences in the color vs. redshift plots presented in Chapter 5, indicating that systematic instrumental error is unimportant for the purposes of this dissertation.

Equation 4.11 is greatest for the H magnitude, and smallest for H-K, in both the unrestricted and restricted (i.e. without June 1983) data sets. It is not surprising that the errors are relatively greater for the magnitude compared to those for the colors, because many errors will affect both bands in a color index in a similar way (e.g. eqn. 4.5 vs. eqn. 4.4, the aperture and chopping corrections). A likely source of systematic error for some objects is the possibility of other sources in the reference beam, which becomes increasingly probable at faint magnitudes. The fact that the objects are in galaxy clusters increases the likelihood of another galaxy being in one of the two reference beams, which should mainly affect the H magnitudes. All the high redshift galaxies were observed at the MMT, where chopping was in elevation. Hence the position of the reference beam on the sky depended on hour angle, and was generally different for multiple observations of the same object. At a galactic latitude of 20°, there is on average a 15% probability that a K = 18 source will appear in a reference beam (Lebofsky and Eisenhardt 1984). Most of these are stars, so they will affect V_B and I_B proportionately more than H and K. This may explain the better consistency of H-K compared to V_{B-H} and I_{B-H}.

In summary, the errors listed in Table VII should be viewed cautiously, particularly for the H magnitudes. The color errors are probably representative, especially for H-K.

Reddening

The effects of galactic extinction were corrected for using the reddening maps of Burstein and Heiles (1982). Using the dependence of extinction on Johnson colors from Rieke and Lebofsky (1984) and the relations between V_B, I_B and Johnson B, V, R and I derived below, the following corrections were applied:

$$E(V_B\text{-}H) = 2.68 \ E(B\text{-}V) \hspace{3cm} 4.12$$

$$E(I_B\text{-}H) = 1.19 \ E(B\text{-}V)$$

$$E(H\text{-}K) = 0.15 \ E(B\text{-}V)$$

$$A_H = 0.54 \ E(B\text{-}V)$$

Most objects are at high galactic latitude and have $E(B\text{-}V) < 0.12$. Exceptions are the galaxies labelled A553, 3C368, 3C427.1, 3C438, 4C26.23, and 4C39.12. 4C26.23, at a galactic latitude $b = 8.4°$, longitude $\ell = 187.7°$, was not on the Burstein and Heiles (1982) map. Sandage's (1972b) cosecant law, normalized to the Burstein and Heiles value at $b = 10°$, $\ell = 187.7°$ was used to derive $E(B\text{-}V) = 0.31$ for 4C26.23.

Other Corrections

The K correction, equation 2.8, is large, and fundamental to this dissertation. It will be discussed at length in Chapter 5, as will the evolutionary correction. Photometric corrections to determine mono-chromatic fluxes are discussed in the section on Calibration below. Corrections for Bautz-Morgan class (based on the contrast of the brightest galaxy relative to fainter cluster members) and cluster richness (Sandage and Hardy 1973) were not made, because they require

knowledge of the cluster properties which was not available. The possibility of intergalactic extinction will be discussed in Chapter 5.

Calibration

In order to allow comparison with other work, two procedures were used. The first solves for Johnson magnitudes as a function of SPIV instrumental magnitudes using standard stars; the other attempts to model the objects to calculate monochromatic fluxes. Both approaches have problems, which is why only the H magnitudes are listed in Table VII (H requires the least modification).

Standard Star Regression

The infrared photometry for many secondary standard M dwarfs in Elias et al. (1982) was supplemented by optical photometry from Veeder (1974). Two parameter multilinear regression fits, using Bevington's (1969) REGRES program, were applied to the colors (the H transformation was assumed) as a function of B, V, R, I, H and K for the standards. The following relations were found to fit the standards best (here the SPIV magnitude is on the left, published standard values are on the right). Sigma is the standard deviation of the fit.

$$V_B = 0.01 + 0.82 * V + 0.17 * B \qquad \sigma = 0.09 \qquad 4.13$$

$$I_B = 0.12 + 0.70 * I + 0.30 * R \qquad \sigma = 0.10$$

$$K = -0.10 + 0.77 * K + 0.24 * H \qquad \sigma = 0.013$$

$$H = H \quad (\text{assumed}) \qquad \sigma = 0.027$$

It is gratifying to see that equation 4.6 is nearly satisfied by these relations. If agreement with eqn. 4.6 is forced, the standard deviations rise only slightly:

$$V_B = 0.83 * V + 0.17 * B \qquad \sigma = 0.14 \qquad 4.14$$

$$I_B = 0.70 * I + 0.30 * R \qquad \sigma = 0.14$$

$$K = 0.76 * K + 0.24 * H \qquad \sigma = 0.014$$

Of greater interest is the inverse transformation, i.e. the Johnson magnitudes in terms of the SPIV instrumental system. These will be given with H_{SPIV} as the second parameter, because it is always present in Table VII. Again forcing agreement with eqn. 4.6, with the Johnson magnitudes on the left, the transformations are:

$$V = 0.96 * V_B + 0.04 * H \qquad \sigma = 0.11 \qquad 4.15$$

$$I = 0.70 * I_B + 0.30 * H \qquad \sigma = 0.13$$

$$K = 1.24 * K - 0.24 * H \qquad \sigma = 0.016$$

Note that equation 4.15 could be rewritten as: $V-H = 0.96 * (V_B-H)_{SPIV}$; $I-H = 0.7 * (I_B-H)_{SPIV}$; $H-K = 1.24 * (H-K)_{SPIV}$; where the left hand sides are the colors in the standard system.

Applying equations 4.13 to 4.15 to galaxies may be less accurate than the values of σ imply, because the galaxies are so much redder and fainter than the standard stars. It was to aid in transforming galaxy observations that the agreement with equation 4.6 was forced, that is the coefficients were required to add to 1 (as is required if the detectors are linear).

Photometric Corrections

A calibration technique which compensates for the differences in effective wavelength for different colored objects is the photometric correction, discussed in Low and Rieke (1974). When added to the

magnitude of the object, the result is a monochromatic magnitude at the wavelength chosen, if the model is correct.

The photometric correction in band x can be defined as:

$$P.C. = -2.5 \log \frac{\int F_m^{AO} \phi_x d\lambda}{\int F_m^O \phi_x d\lambda} \frac{F_m^O(\lambda_x)}{F_m^{AO}(\lambda_x)} \qquad 4.16$$

where the subscript "m" refers to the model spectra, and λ_x is some wavelength in band x, often the effective wavelength (equation 2.1). When added to the instrumental magnitude, equation 4.4, we have:

$$m_x^O + P.C. = -2.5 \log \frac{\int F^O \phi_x d\lambda}{\int F^{AO} \phi_x d\lambda} \frac{\int F_m^{AO} \phi_x d\lambda}{\int F_m^O \phi_x d\lambda} \frac{F_m^O(\lambda_x)}{F_m^{AO}(\lambda_x)} + m_x^{AO} \qquad 4.17$$

where I have used equation 4.6 and assumed that $r(t^O) = r(t^*)$ in equation 4.4. If the model is a good one, i.e. $F_m = F$, equation 4.17 reduces to:

$$m_x^O + P.C. = -2.5 \log \frac{F_m^O(\lambda_x)}{F_m^{AO}(\lambda_x)} + m_x^{AO} \qquad 4.18$$

which can be converted to a monochromatic flux.

These corrections have been calculated using the same spectra (appropriately redshifted) as were used for the UV blocking filter correction above. The wavelengths chosen were (in microns): 0.55, 0.90, 1.65, and 2.20. These wavelengths were selected so that the corrected data could readily be converted to fluxes, given the information in Johnson (1966). The photometrically corrected data are listed in Table IX. These corrections are most important at V_B and I_B, where they are as large as -0.7 mag. For H and K they were usually less than 0.1 in absolute value. The corrections were mainly in the sense that the observed magnitude was an underestimate of the monochromatic brightness,

TABLE IX

Data with Photometric Corrections Applied

Object	Redshift	V_B-H	I_B-H	H	H-K
A569	0.019	3.04	1.99	9.37	0.27
4C39.12	0.021	2.69	1.53	8.98	0.29
3C465F	0.031	3.31	1.82	9.66	0.26
3CR98	0.031	2.97	1.78	11.02	0.33
A2634south	0.031	3.09	2.55	9.99	0.31
4C26.23	0.040	3.00	1.44	11.36	0.27
A671	0.050	3.30	2.08	11.25	0.36
4C25.04	0.066	2.58	1.58	13.57	0.44
A553	0.067	3.10	1.76	11.75	0.35
CrB Cl .1	0.072	3.28	1.72	12.41	0.30
A399	0.073	3.35	2.68	12.17	0.36
A568	0.078	3.00	2.32	12.43	0.24
4C28.18	0.083	2.85	1.82	12.80	0.30
3C277.3	0.086	3.12	2.43	12.99	0.30
4C30.19	0.093	2.84	1.77	13.08	0.28
A21	0.095	3.20	2.69	12.54	0.40
3CR223.1	0.108	3.08	1.99	13.50	0.56
4C36.14	0.112	2.96	1.85	12.83	0.56
4C-04.17	0.118	3.60	1.93	14.04	0.48
3CR135	0.127	2.49	1.68	14.55	0.61
3CR197.1	0.130	3.05	1.55	14.63	0.44
1431+3146	0.131	3.14	1.55	13.31	0.48
1153+2341	0.143	3.11	2.32	12.70	0.53
1534.4+3748	0.153	2.77	1.43	14.25	0.84
A868	0.154	2.11	1.92	13.58	0.61
A1759	0.168	3.31	2.32	14.14	0.55
A2320	0.170	3.06	2.87	13.03	0.33
4C31.07	0.175	2.81	2.11	14.76	0.67
1304+3110	0.183	2.92	2.88	13.91	0.53
1253+4422	0.198	3.04	1.99	15.38	0.74
4C39.72	0.206	2.95	2.81	15.12	0.62
3C436	0.215	2.73	2.97	15.38	0.69
A1246	0.216	3.14	2.36	13.70	0.45
A2397	0.222	3.15	1.96	13.92	0.50
1604.0+3935	0.235	2.88	2.95	15.11	0.44
0308.5+1642	0.260	3.46	1.92	15.06	0.93
1612.6+4204	0.275	3.36	3.11	15.93	0.78
1607.6+3953	0.280	3.03	2.79	15.76	0.86
1021.1+0427	0.286	3.22	2.11	14.86	0.73
3C438	0.290	3.77	3.21	14.76	0.79
1610.8+4115	0.300	3.84	3.11	15.36	0.72
4C30.14	0.301	3.60	2.28	15.98	0.13
1049.4-0904	0.330	3.63	2.89	15.40	0.74
4C37.29	0.346	3.51	2.95	16.59	0.80

TABLE IX--Continued

0948.9+4426	0.361	3.89	2.69	15.68	0.68
1446+26G2	0.370	3.86	2.83	16.21	0.82
3C268.3	0.371	4.23	3.91	16.26	1.01
0938-01	0.382	4.49	2.71	16.16	0.81
0822+67	0.384	4.38	3.01	15.85	0.83
0949.9+4409	0.385	4.28	2.82	15.65	0.78
3C42	0.395	4.52	2.56	15.88	0.84
9C114	0.410	4.10	2.84	16.15	0.76
1613+31	0.415	3.96	3.88	16.19	0.79
3C274.1	0.422	4.94	3.27	16.00	0.79
3C244.1	0.428	4.45	2.81	15.90	0.67
1134+015	0.430	3.52	2.69	15.40	0.94
9sigma	0.430	5.02	3.34	16.18	0.64
3C200	0.458	4.47	3.07	15.88	0.83
13F	0.460	3.31	2.83	16.51	0.79
3C228	0.520	4.39	3.10	17.36	0.85
16betabeta	0.530	5.12	3.38	16.36	0.67
3C330G2	0.530	4.57	3.24	16.53	0.74
3C225B	0.580	4.47	2.65	17.05	0.52
16KPNmu	0.610	3.16	2.92	17.16	0.72
3C337	0.630	3.17	2.73	17.95	0.53
21KPNsigma	0.640	2.60	2.95	17.19	1.02
13KPNgamma	0.690	5.03	2.95	17.00	0.66
13KPNalpha	0.750	4.61	2.82	17.01	0.76
3C343.1	0.750	3.11	3.44	17.31	0.74
3C340	0.760	2.90	2.22	16.56	0.13
3C217	0.890	3.12	1.93	19.04	0.72
16KPNdelta	0.900	4.04	1.56	17.86	1.16
16KPNepsilon	0.920	1.04	0.76	19.77	2.49
3C289	0.967	5.37	3.67	17.82	0.99
3C184	0.994	4.63	2.59	17.61	0.80
3C280	0.996	3.81	2.76	17.61	0.93
3C356	1.079	3.47	2.92	18.42	1.40
3C252	1.105	3.06	1.64	18.66	0.88
3C368	1.132	3.49	1.72	17.86	0.95
3C427.1	1.175	3.83	3.10	17.00	0.75

except for V_B where the correction ranged from -0.5 to +0.4. For V_B-H however, it is clear from Chapter 5 that the model is not accurate, except at low redshift.

Because of this, in Chapter 5 I have used the data in Table VII in preference to that in Table IX. For similar reasons I decided to use the photon number spectrum rather than the energy spectrum. For the diodes in particular, the IRF is fairly flat: i.e. one photon anywhere within the sensitive region produces the same signal, independent of energy.

CHAPTER 5

ANALYSIS

        With the observations reduced, we are ready to discuss their significance. The galaxies observed naturally fall into two categories: those that are radio sources, and those that are not. Both categories include redshifts near one, with lookback times of many billions of years. The major issues addressed here are:

        1) Are these galaxies the same as nearby ellipticals?

        2) Do radio galaxies have the same properties as non-radio galaxies?

        3) If 1) is false, can the differences be explained by stellar evolution over the lookback time?

The Sample

High Redshift Galaxies

        There are still relatively few high redshift galaxies known. Because of the extremely faint visual magnitudes, spectroscopic redshifts have been difficult to obtain. In fact one of the original motivations behind SPIV was the possibility of estimating redshifts from broadband colors. This hope appears unlikely to be fulfilled, but in any case the number of galaxies with known redshifts greater than 0.5 is small, which leads to problems in developing a well defined sample. The policy was to observe as many of these as possible, investigating selection effects after the fact.

Radio Galaxies

Most of the high redshift radio galaxies are 3C sources whose redshifts have been measured by Spinrad and his collaborators. A well defined sample of 3C galaxies has been investigated by Lilly and Longair (1984), and the subset observed here can be usefully compared with their results.

At the lower redshifts, especially below z = 0.2, there are many galaxies to choose from. Radio galaxies were selected according to the following criteria:

1) Membership in the Burbidge and Crowne (1979) Optical Catalog of Radio Galaxies

2) Classified as an elliptical galaxy

3) $z < 0.2$

4) $m_V < 18.$

5) $-20° < dec < +65°$

The first requirement means $L_{radio} > 10^{41}$ergs/sec between 10 MHz and 10 GHz, and that a redshift has been measured. The second excludes N galaxies. The third is appropriate for a giant elliptical which meets the fourth criterion, which was imposed so that these galaxies could be readily observed using the 61 inch telescope. The north declination limit is also imposed by the 61".

Non-Radio Galaxies

All of the optically selected galaxies with z > 0.5 are from a survey for faint clusters of galaxies conducted over the past decade by Gunn, Hoessel and Oke (Oke 1984). Information on these was kindly

presented in advance of publication. The galaxies were identified as the brightest in a cluster on deep KPNO 4 meter IIIaF and IVN plates, with redshifts subsequently measured using the Oke scanner and the Prime Focus Universal Extragalactic Instrument (PFUEI) on the Palomar 200 inch telescope.

Lower redshift galaxies were also required to be first ranked cluster ellipticals, and were often in Abell clusters. One of these, 1304+3110, is a radio source, and A2634 appears to coincide with 3CR465 (Burbidge and Crowne 1979). Several second and lower ranked ellipticals were also observed, but these will not be discussed here.

In all, data from 79 galaxies is presented, 40 of them radio galaxies. The distribution of these objects in redshift is shown in Figure 12.

Selection effects

The lack of a well defined sample can lead to serious biases. Two important selection effects here are: 1) Galaxies and clusters must be identified as such, generally by deep optical surveys; 2) Redshifts must have been obtained.

The first effect means the high redshift non-radio galaxies are biased towards rich clusters whose higher contrast makes them stand out against the background, which becomes increasingly crowded at fainter magnitudes. Also, red galaxies may be missed because the K correction will make them extremely faint in the optical for high redshifts. Gunn, Hoessel and Oke used red sensitive plates to forestall this problem.
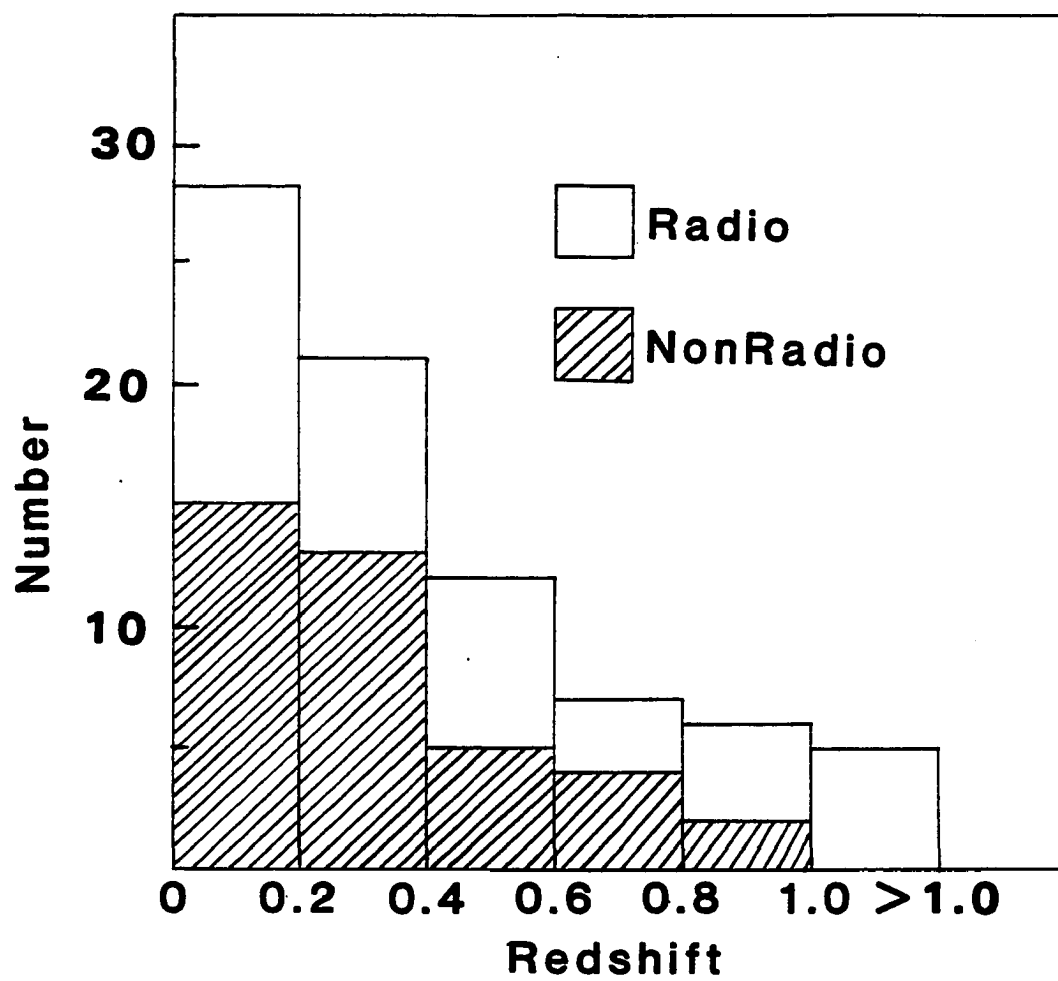
Figure 12. Distribution of Redshifts in Sample.

The second effect will tend to favor galaxies with emission lines. Gunn et al. circumvented this bias by getting redshifts from fitting to standard galaxy spectra, rather than looking for lines. By attempting to adjust discovery and redshift measuring procedures to what is expected from redshifting well observed nearby galaxies, however, they may be discriminating against the unexpected.

Because the 3C sample has nearly complete identification and redshift measurements, the selection effects for it are quite different from those mentioned above. Comparing the radio and non-radio galaxies is therefore very useful. The radio galaxies observed here may include some N galaxies at high redshifts. Two low redshift (z=.12) N galaxies, 3CR135 and 4C-04.17, were observed and found to have peculiar V_B-H colors, in agreement with the findings of Lilly and Longair (1982) and of Sandage (1973a).

Observed and Predicted Colors

The K Correction

The data in Table VII have been corrected for several effects: extinction, reddening, aperture, cancellation due to chopping, and a correction to put V_B observations made with and without the UV blocking filter on the same system. The largest of these is the aperture correction, which does not alter the colors. The other corrections are less than 0.2 magnitudes in most cases, which is not substantial given the errors. The colors in Table VII are therefore "model independent," not significantly affected by changes in the spectrum of Figure 1, and can reasonably be called observed quantities. The K correction

(equation 2.8), in contrast, is large (up to 3 magnitudes in some cases) and depends strongly on Figure 1. For these reasons I have chosen to treat the K correction as a "zero order" (no evolution) theoretical prediction for comparison with the observed colors.

The definition of K_{corr} in equation 2.8 differs in appearance from the more commonly used form (Oke and Sandage 1968):

$$K_{corr} \equiv 2.5 \log \frac{\int \phi(\lambda)L(\lambda/1 + z)d\lambda}{(1 + z)\int \phi(\lambda)L(\lambda)d\lambda} \qquad 5.1$$

where $L(\lambda)$ is the _energy_ per unit wavelength of the object in the object (emitted) frame. The difference, the factor of $1 + z$ in the denominator which does not appear in equation 2.8, can be traced to my use of the photon rather than the energy spectrum, and the two definitions are equivalent.

The equation for the predicted color as a function of redshift, referred to an A0 star, follows from equation 2.12 or 4.5:

$$m_x - m_y = -2.5 \log \frac{\int \phi_x N(\lambda/1+z)d\lambda}{\int \phi_x A0(\lambda)d\lambda} \frac{\int \phi_y A0(\lambda)d\lambda}{\int \phi_y N(\lambda/1+z)d\lambda} \qquad 5.2$$

which includes the prediction for the zero redshift color. Equation 5.2 was calculated for the V_B-H, I_B-H, and H-K colors, while equation 2.8 was used to calculate the K correction for the H magnitude. For convenience in comparing to the observations, these predictions were fitted by polynomials in redshift, as shown in Table X. It was necessary to use two polynomials to obtain a satisfactory fit to the predicted H-K color, one for redshifts < 0.7, another for the high redshifts. The polynomial for V_B-H is not valid beyond $z = 1$, because this would require data beyond the range of Figure 1. Because the zero

TABLE X

Polynomial Fits to Predicted Color vs. Redshift Curves

N is the order of the polynomial. Δmax is the maximum deviation (in magnitudes) of the polynomial from the exact prediction. a_M is the coefficient of the Mth order term, z^M.

Color		N	Δmax	a_0	a_1	a_2	a_3	a_4	a_5
V_B-H	z<1	3	0.03	3.31	2.06	4.195	-3.70		
I_B-H		4	0.03	1.87	0.88	1.57	-2.61	1.44	
H-K	z<.7	5	0.02	0.26	1.14	11.38	-54.11	77.87	-35.91
H-K	z>.7	3	0.01	-2.00	6.80	-4.96	1.19		
H (K corr)		5	0.03	0.02	-0.60	4.66	-8.98	6.26	-1.495

order term a_0 is the predicted color for zero redshift, the K correction (equation 2.8) for each color is just these polynomials less a_0, except for the H magnitude where the K correction is shown directly.

Comparison of Observed Colors with "No Evolution" Prediction

The exact predictions of equation 5.2 are shown along with the observed colors from Table VII in Figure 13, plotted separately for radio and non-radio galaxies. For a few objects, two sigma upper (H-K) or lower (V_B-H, I_B-H) limits are shown by arrows. 3C241 has been omitted (unless explicitly stated otherwise) because no other object is near it in redshift, and it was observed only once under poor conditions. The similarity of the radio and non-radio observations is evident, and for the present they will be lumped together. This procedure will be justified in a separate section. The H magnitude observations will be discussed in the section on the Hubble diagram.
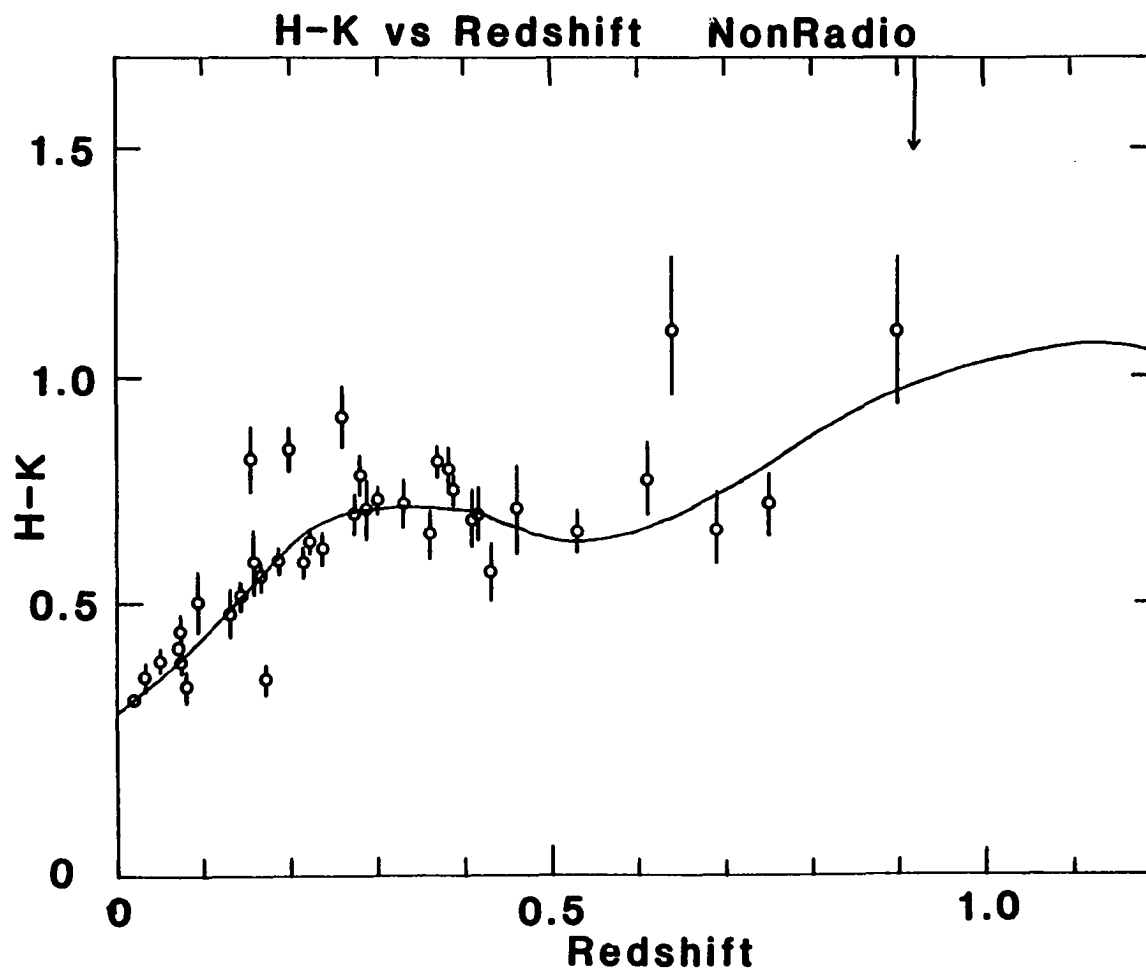
Figure 13(a). Observed H-K Color vs. Redshift for Non-Radio Galaxies. The observations are shown first
separately for radio and non-radio galaxies, then together, for the colors indicated. The solid line
is the no evolution prediction from the spectrum of Figure 1. Open circles are non-radio galaxies,
filled are radio sources. Arrows indicate only an upper or lower limit for the color was measured.

Figure 13(b). Observed H-K Color vs. Redshift for Radio Galaxies. See Figure 13(a) for explanation.
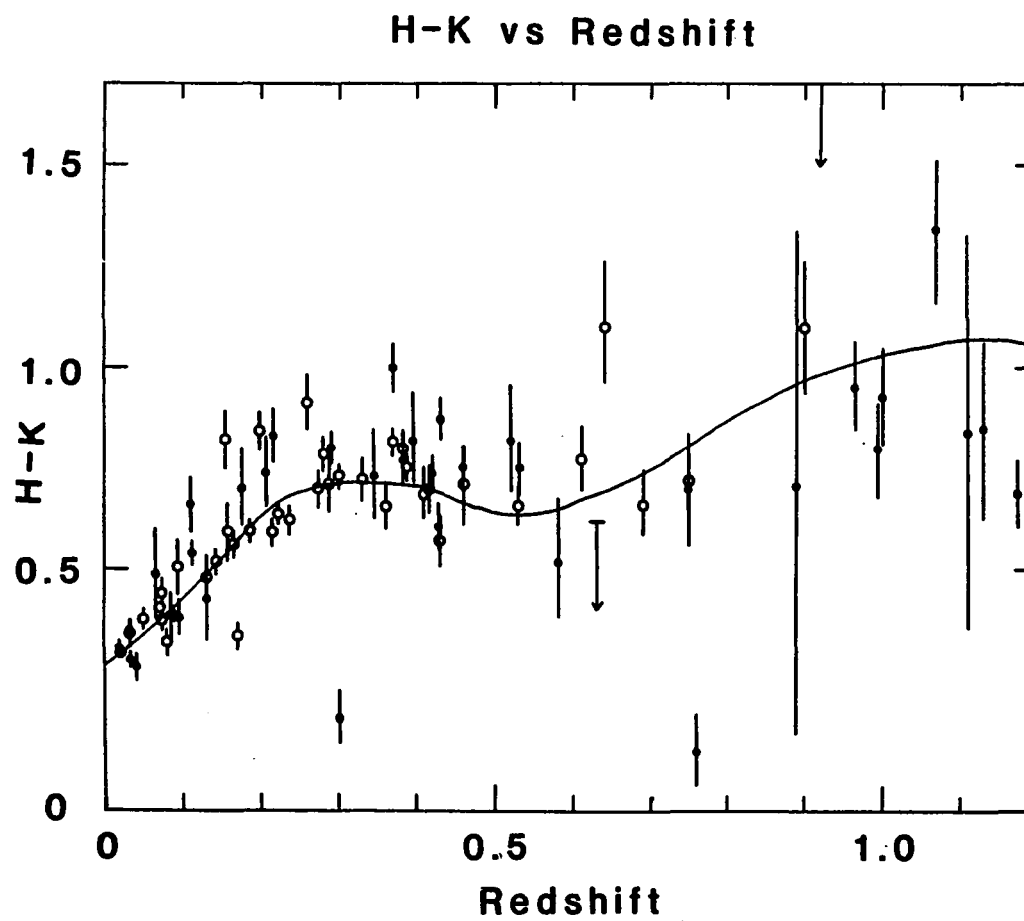
Figure 13(c). Observed H-K Color vs. Redshift. See Figure 13(a) for explanation.
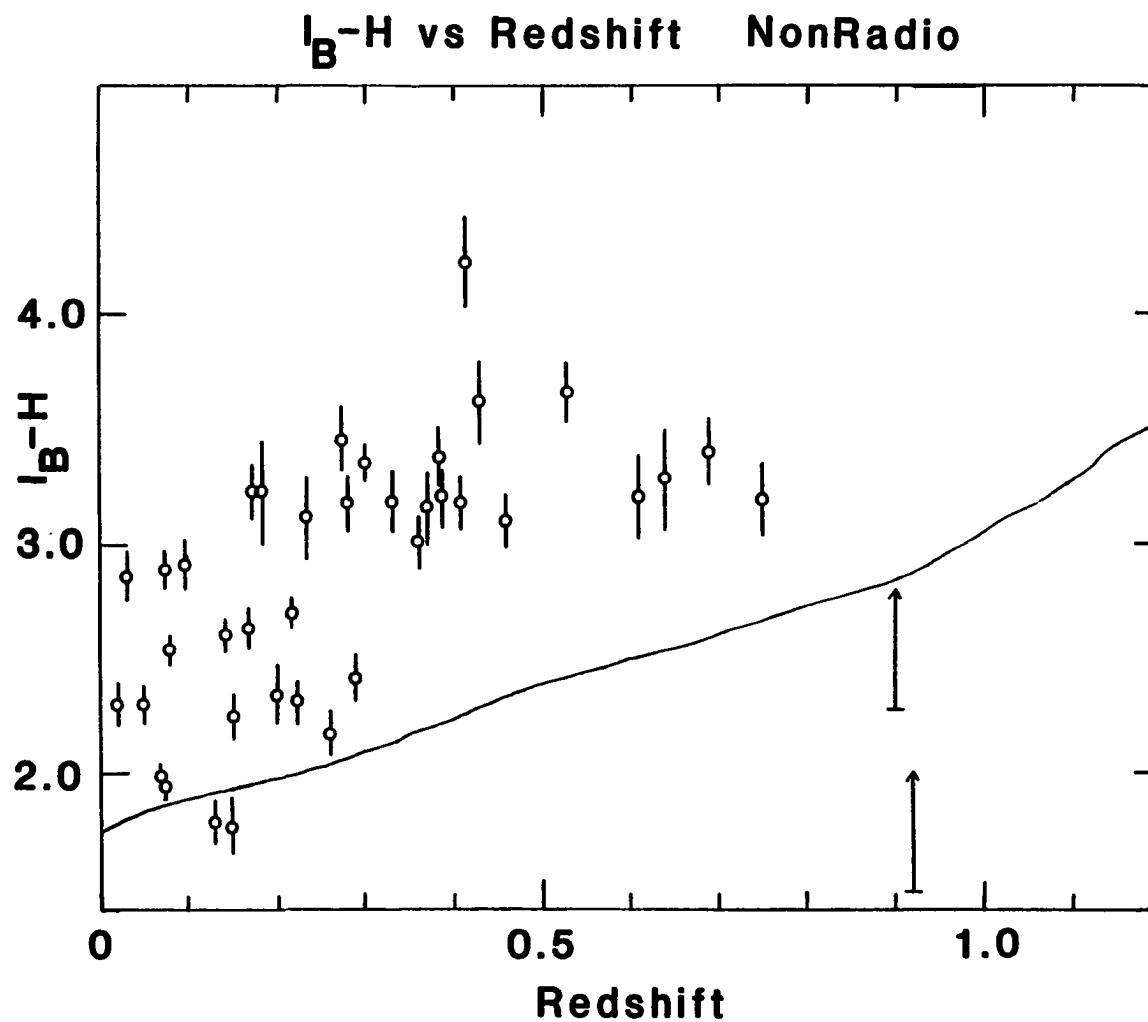
Figure 13(d). Observed I_B-H Color vs. Redshift for Non-Radio Galaxies. See Figure 13(a) for explanation.

Figure 13(e). Observed I_B-H Color vs. Redshift for Radio Galaxies. See Figure 13(a) for explanation.

Figure 13(f). Observed I_B-H Color vs. Redshift. See Figure 13(a) for explanation.

V$_B$-H vs Redshift NonRadio
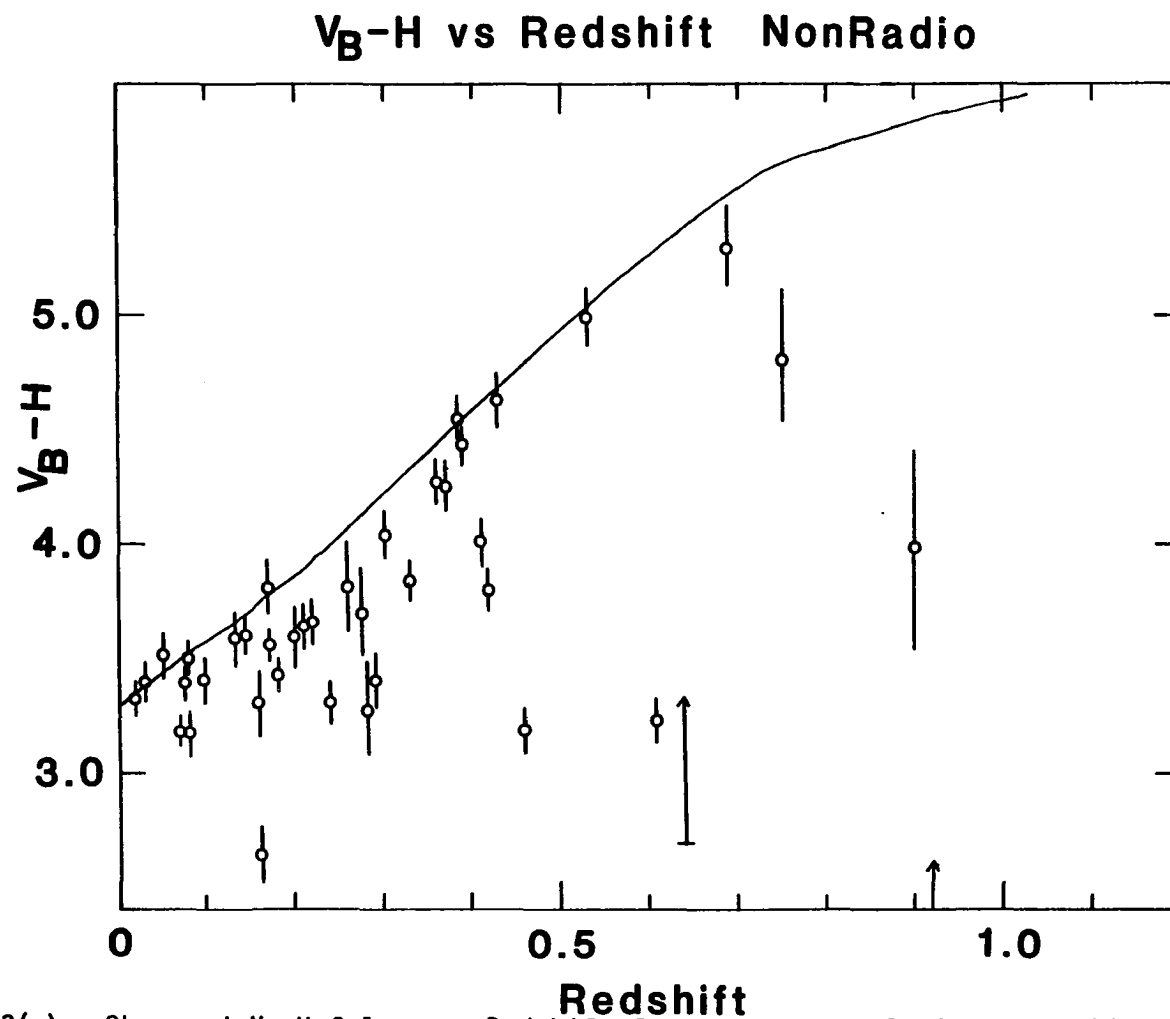
Figure 13(g). Observed V$_B$-H Color vs. Redshift for Non-Radio Galaxies. See Figure 13(a) for explanation.

V_B-H vs Redshift Radio
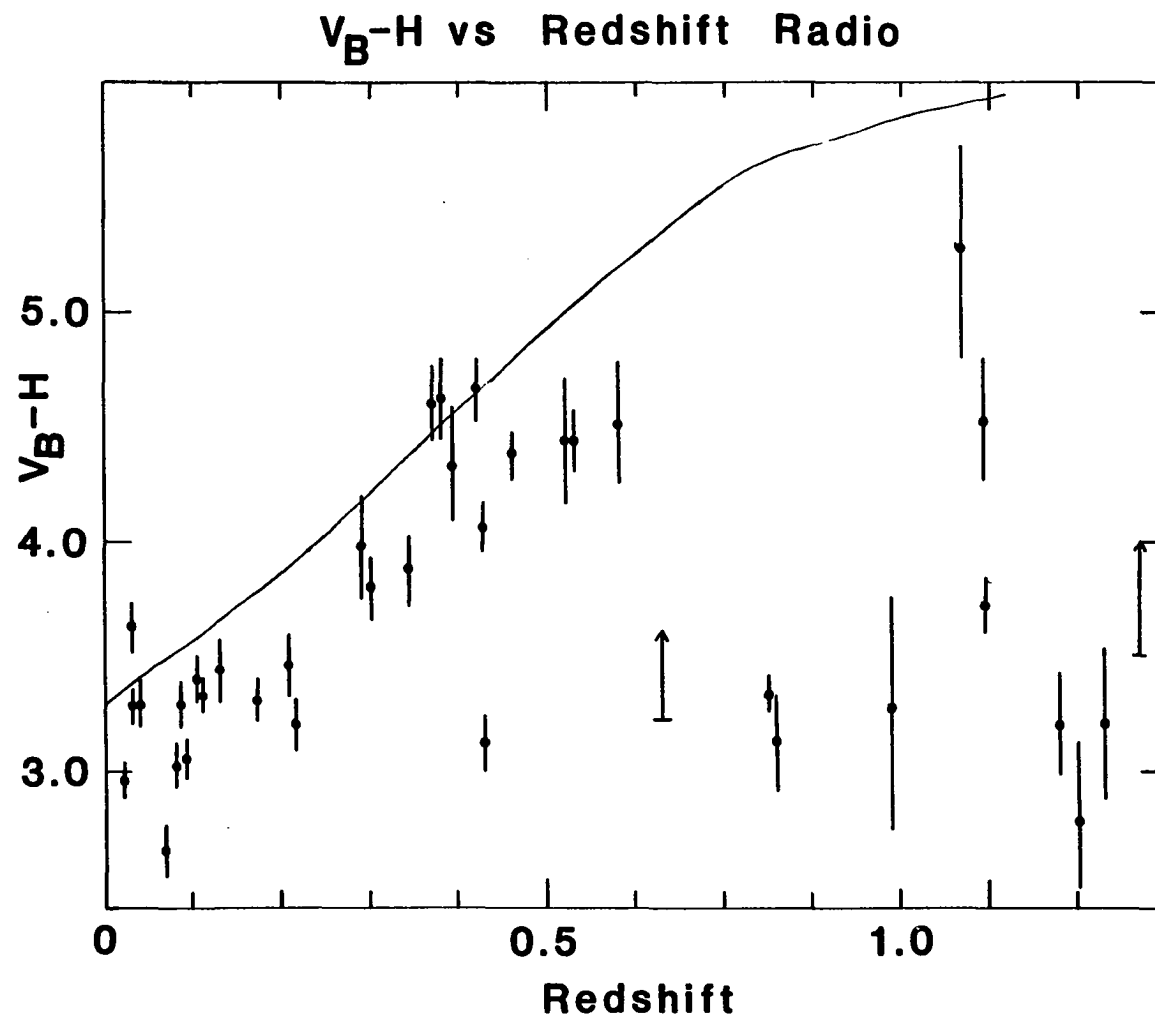
Figure 13(h). Observed V_B-H Color vs. Redshift for Radio Galaxies. See Figure 13(a) for explanation.
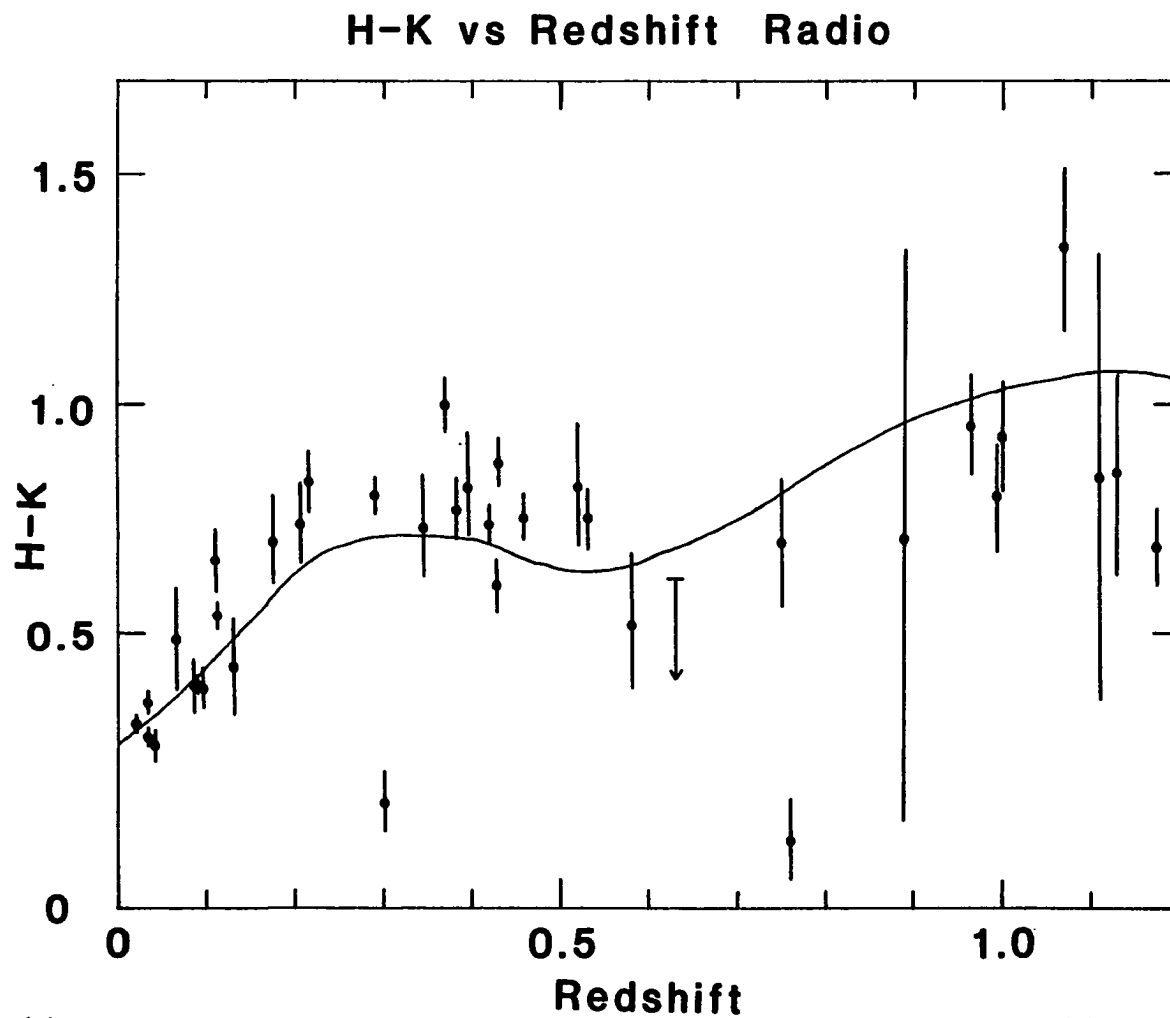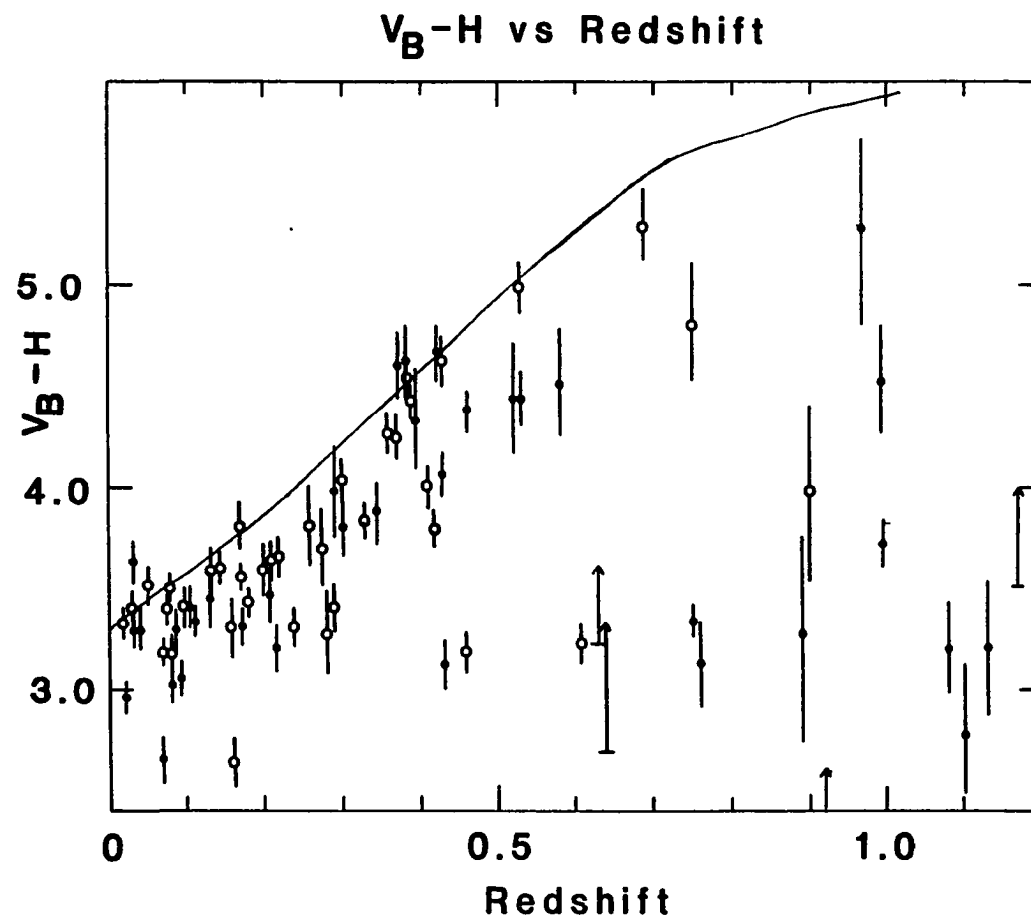
Figure 13(i).   Observed V_B-H Color vs. Redshift.   See Figure 13(a) for explanation.
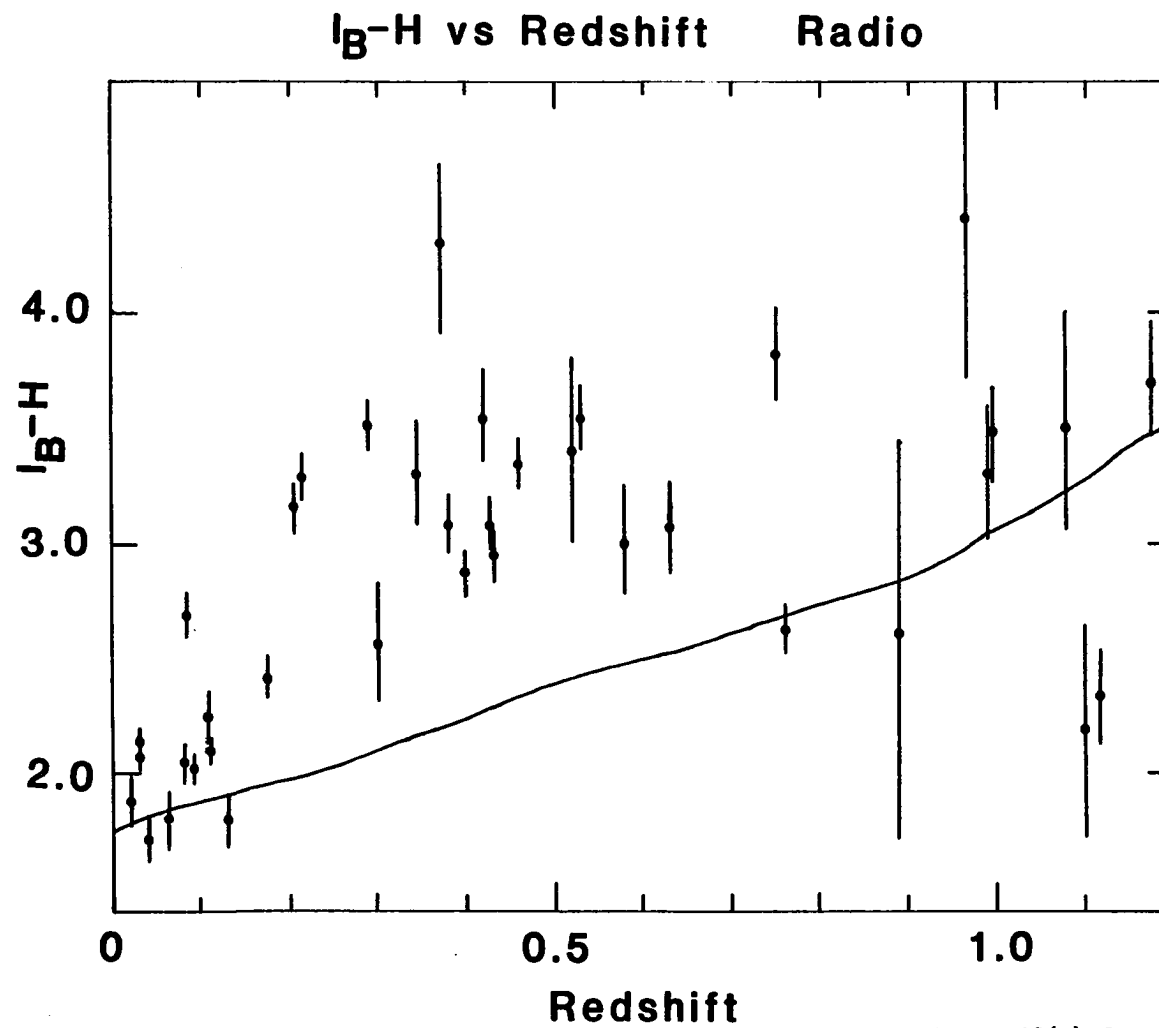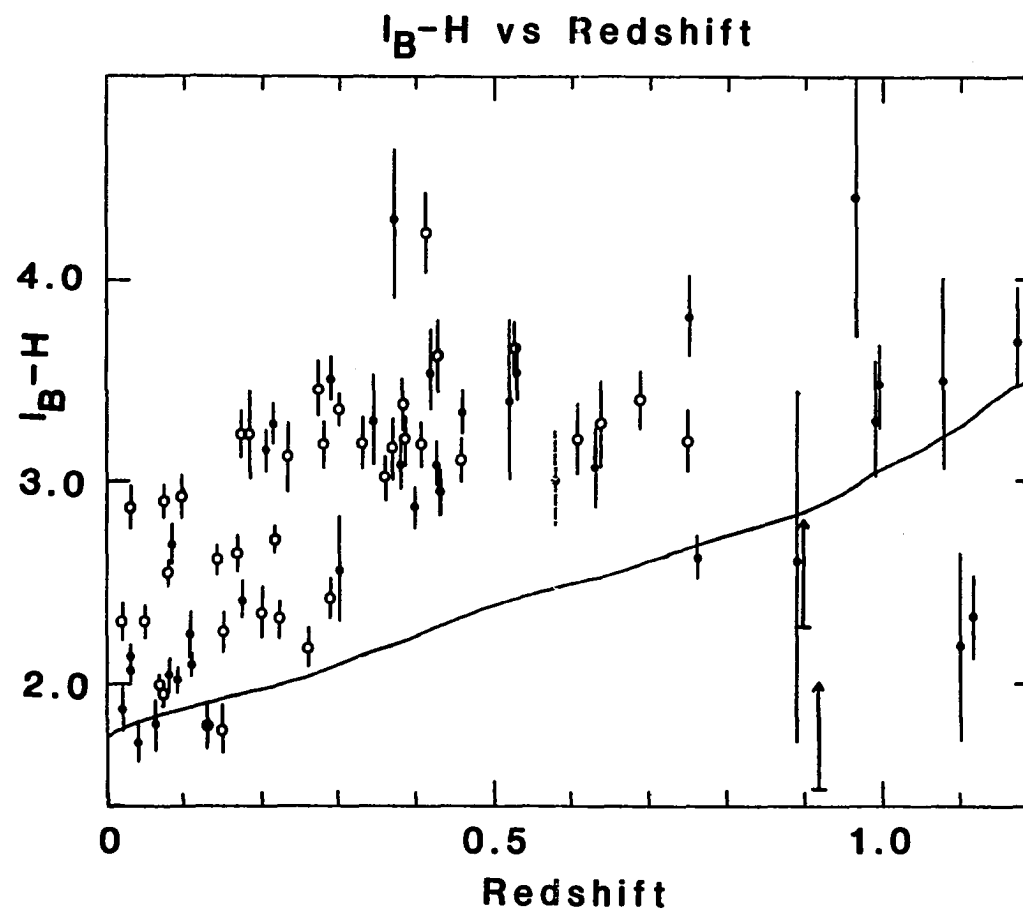
It is to be emphasized that the predicted colors contain no free parameters: the zero point was calculated from the IRF, Figure 1, and the AO star spectrum (Djorgovski 1984), without reference to the observed data. It is also worth noting that the predicted curves contain no effects of stellar evolution. They are simply the result of changing the wavelength scale of the light from the present day population in ellipticals. Predictions incorporating stellar evolution are discussed below.

Zero Points. In general, the zero redshift colors predicted from equation 5.2 are in good agreement with the observations. Empirical zero points were found by calculating first order (linear) weighted fits to the low redshift observations (z < 0.30 for V_B-H and I_B-H, z < 0.15 for H-K). The lower redshift cutoff was used for H-K because a linear fit is clearly not appropriate by z = 0.3. The empirical (listed first with their formal uncertainty) and predicted zero points are: V_B-H: 3.28±.02, 3.30; I_B-H: 2.01±.02, 1.86; H-K: 0.26±.01, 0.26. The agreement shows the accuracy of the IRF, and of Figure 1 in the regions measured at z = 0. I_B-H shows the poorest agreement, but matters only get worse as the redshift increases. Given the scatter in the low redshift I_B-H data, the discrepancy is not serious.

Polynomial Fits to the Data. To determine if the data differed systematically from the no evolution prediction, weighted polynomials were fitted to the observations. These are listed in Table XI. The reduced chi squares calculated for these fits and those of Table X to various subsets of the data are shown in Table XII. Several points were always excluded in calculating these polynomials and chi-square values:

TABLE XI

Polynomial Fits to the Observed Color vs. Redshift Data

Column headings have the same meanings as for Table X.

Color	N	a_0	a_1	a_2	a_3	a_4	a_5
V_B-H	1	3.31	0.99				
V_B-H	3	3.40	-2.20	14.31	-10.89		
I_B-H	3	1.98	4.35	-3.67	0.84		
H-K	3	0.24	2.51	-3.77	1.76		
H-K	5	0.27	1.25	7.15	-31.25	38.85	-15.29

those where only two sigma limits were measured, 3C340 and 4C30.14 because of their extreme blueness at H-K, 3C241 because of its isolated redshift, and A868 because of probable reference beam problems. These points were excluded from all further analysis (with appropriate substitutions for two sigma limit objects) in all colors, and this data set will be referred to as the "unselected set." In calculating the polynomial fits in Table XI, several other points were omitted because their colors were sharply different from other objects at the same redshift. These varied with the color involved, and are discussed in the relevant sections below. This smaller data set is referred to as the "selected set." Only the first order V_B-H polynomial in Table XI was fit to the unselected set. Also shown in Table XII are the values of σ_c, the (presumed) cosmic dispersion in color necessary to make the reduced chi square equal to unity. These were found by calculating the quantity:

TABLE XII

Reduced Chi-Square and "Cosmic" Dispersion Values

Sample is the subset of the color data for which the chi-square value was calculated. Unless otherwise indicated, the full redshift range was used. "uns" and "sel" mean the unselected and selected sets. Fit is the polynomial from Table X (for "pred" entries) or Table XI used. "IH3", for example, is the third order fit to I_B-H in Table XI. N is the number of data points in the sample. X^2/v is the reduced chi square value. σ_c is the cosmic dispersion discussed in equation 5.3.

Color	Sample	Fit	N	X^2/v	σ_c
H-K	uns	pred	73	5.15	0.10
H-K	uns	HK3	73	5.04	0.10
H-K	uns	HK5	73	4.74	0.09
H-K	uns z<.5	HK5	55		0.09
H-K	sel	pred	66	2.14	0.05
H-K	sel	HK3	66	2.05	0.06
H-K	sel	HK5	66	1.64	0.035
I_B-H	uns	pred	73	97.	
I_B-H	uns	IH3	73	25.	0.42
I_B-H	uns z<.31	IH3	38	46.	
I_B-H	uns z >.31	IH3	35	5.2	
I_B-H	sel	pred	68	101.	
I_B-H	sel	IH3	68	25.6	0.36
V_B-H	uns	pred	71	75.	
V_B-H	uns	pred-.43	71	44.4	
V_B-H	uns	VH3	71	33.8	
V_B-H	uns	VH1	71	21.7	
V_B-H	uns z<.41	pred	47	31.4	
V_B-H	uns z<.41	pred-.29	47	14.7	
V_B-H	uns z<.41	VH3	47	10.9	
V_B-H	uns z<.41	VH1	47	15.9	
V_B-H	uns z>.41	VH1	24	36.1	
V_B-H	sel	pred	60	32.1	0.40
V_B-H	sel	pred-.31	60	14.3	0.26
V_B-H	sel	VH3	60	9.77	0.24
V_B-H	sel z<.41	pred	46	31.3	0.32
V_B-H	sel z<.41	pred-.28	46	14.6	0.23
V_B-H	sel z<.41	VH3	46	10.5	0.23

$$\frac{\Sigma \dfrac{(m_i - f(z_i))^2}{(\sigma_i^2 + \sigma_c^2)}}{N - (n + 1)} \qquad \qquad 5.3$$

where N is the number of object colors m_i with standard deviations σ_i and redshift z_i, and $f(z)$ is an nth order polynomial fit with (n+1) free parameters (but note that (n+1) is zero for the predicted curves).

A868 is unusually blue in V_B-H, and a check showed another galaxy 12 arcseconds to the south. The aperture was 20 arcseconds in this case, so a reference beam problem is virtually certain. The radio sources 4C30.14 and 3C340 are much bluer in H-K than other objects. Both were observed twice, so observational error is unlikely. 3C340 is also quite blue in V_B-H and is a Parkes (high frequency) radio source. The coordinates and discussion in Laing, Riley and Longair (1983) indicate that the wrong object, a z = 0.31 galaxy, was observed. Even at the lower redshift, the H-K color is far too blue. 4C30.14 is also a high frequency radio source. The finding chart image (Grueff, Vigotti, and Spinrad 1980) is not obviously extended, so this object may be an N galaxy.

F Test. In comparing various fits to the data, I will make extensive use of the statistical F test. The F test uses the ratio F of two reduced chi squares. It gives the probability of observing a value larger than F for a random sample (Bevington 1969). Therefore the optimum probability is 50%, for then it is equally likely that a value greater or less than F would be found. I will regard probabilities between 5% and 95% as indicating the two samples for which the chi squares were calculated are equivalent, and probabilities < 1% or > 99%

as showing the samples are significantly different (with the sample having the smaller reduced chi square value favored). The probabilities, shown in Table XIII, were calculated using equation 26.6.15 of Abramowitz and Stegun (1965).

H-K. The agreement in H-K between observation and prediction is excellent, with a few isolated exceptions, most of which are excluded from the unselected set. The unselected set here excludes 3C337 and 16KPNepsilon, for which only two sigma limits in H-K were found. Comparison with the predicted polynomials of Table X showed that a cosmic scatter of 0.10 magnitudes is needed to obtain a reduced chi square value of unity, for both the $z > 0.7$ and $z < 0.7$ observations. The average of the residuals is less than 0.02 mag, in the sense that the data are slightly redder than predicted.

The third and fifth order fits are plotted in Figure 14(a), along with the predicted curve (Table X). Several points were omitted in calculating these polynomials (in addition to those excluded from the unselected set): 3CR223.1, 1534.4+3748, A2320, 1253+4422, 0308.5+1642, 3C268.3, and 21KPNsigma. A2320 is unusually blue and was observed twice, but in both cases there were problems with the telescope mount at the time, so observational error is a possibility. The other sources are all too red. 3CR223.1 and 21KPNsigma were observed twice, and the H-K measurements are consistent. 3C268.3 is also very red in I_B-H. The excess redness in these objects is most likely due to a nonthermal source, unless it is caused by reference beam problems. Figure 14(a) shows the fitted polynomials in good agreement with the predicted curve, with the fits slightly bluer at redshifts near one. For the unselected

TABLE XIII

F Test Comparison of Observed and Predicted Colors

Sample indicates if a restricted redshift range was used and if the data set was selected or unselected; and in cases where fits at two different redshift ranges are compared, which polynomial fit was used for both redshift ranges. Fit 1 and Fit 2 are the fits from Table XII for which the ratio of the reduced chi squares, F, was calculated. v_1 and v_2 are the number of degrees of freedom for the respective fits. P is the probability that a value larger than F would be obtained from a random sample.

Color	Sample		Fit 1	Fit 2	v_1	v_2	F	P
H-K	uns		pred	HK3	73	69	1.02	47%
H-K	uns		pred	HK5	73	67	1.08	37%
H-K	sel		pred	HK3	66	62	1.04	46%
H-K	sel		pred	HK5	66	60	1.30	15%
I_B-H	uns		pred	IH3	73	69	3.88	$<10^{-6}$
I_B-H	sel		pred	IH3	68	64	3.95	$<10^{-6}$
I_B-H	uns	IH3	z<.31	z>.31	34	31	8.85	$<10^{-6}$
V_B-H	uns	VH1	z>.41	z<.41	24	47	2.27	0.8%
V_B-H	uns		pred	VH3	71	67	2.22	0.06%
V_B-H	sel		pred	VH3	60	56	3.29	7×10^{-6}
V_B-H	sel		pred-.31	VH3	59	56	1.47	8%
V_B-H	uns	z<.41	pred	VH3	47	43	2.88	0.02%
V_B-H	uns	z<.41	pred-.29	VH3	46	43	1.34	17%
V_B-H	sel	z<.41	pred	VH3	46	42	2.98	0.03%
V_B-H	sel	z<.41	pred-.28	VH3	45	42	1.39	16%

Predicted H-K vs Redshift
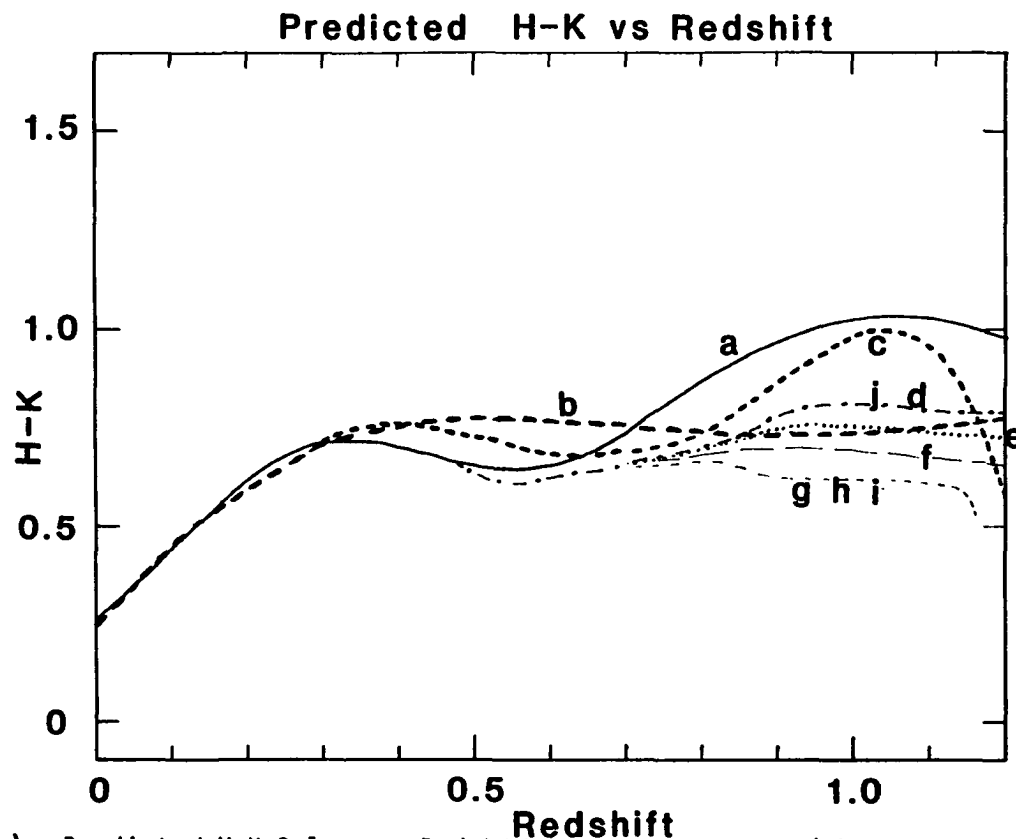
Figure 14(a). Predicted H-K Color vs. Redshift. The solid line (a) is the no evolution prediction from Figure 1. Heavy short dashed line (b) is the third order polynomial fit to the observations (see Table XI). Heavy long dashes (c) are the 5th order fit for H-K, 1st order for V_B-H. Dot dash line (d) and light dash line (g) are for the c model with z_f = 20 and 2 respectively. Dotted line (e) and double dot double dash line (h) are for μ = 0.7 models with z_f = 20 and 2 respectively. Long light dashed line (f) and broadly spaced dotted line (i) are for μ = 0.2 models with z_f = 20 and 2 repectively. Double dot dash line (j) is for μ = 0.54 and z_f= 5 with H_0 = 50 and q_0 = 0. Other models have H_0 = 80 and q_0 = 0.5.

Figure 14(b). Predicted I_B-H Color vs. Redshift. See Figure 14(a) for explanation.

Predicted V_B-H vs Redshift

Figure 14(c). Predicted V_B-H Color vs. Redshift. See Figure 14(a) for explanation.

set, the reduced chi square was virtually identical to those for the polynomials, while for the selected set (which was used to fit the polynomials) the F test probabilities of 15% and 46% show the prediction is not significantly different from the fits. The reduced chi square is unity for a cosmic dispers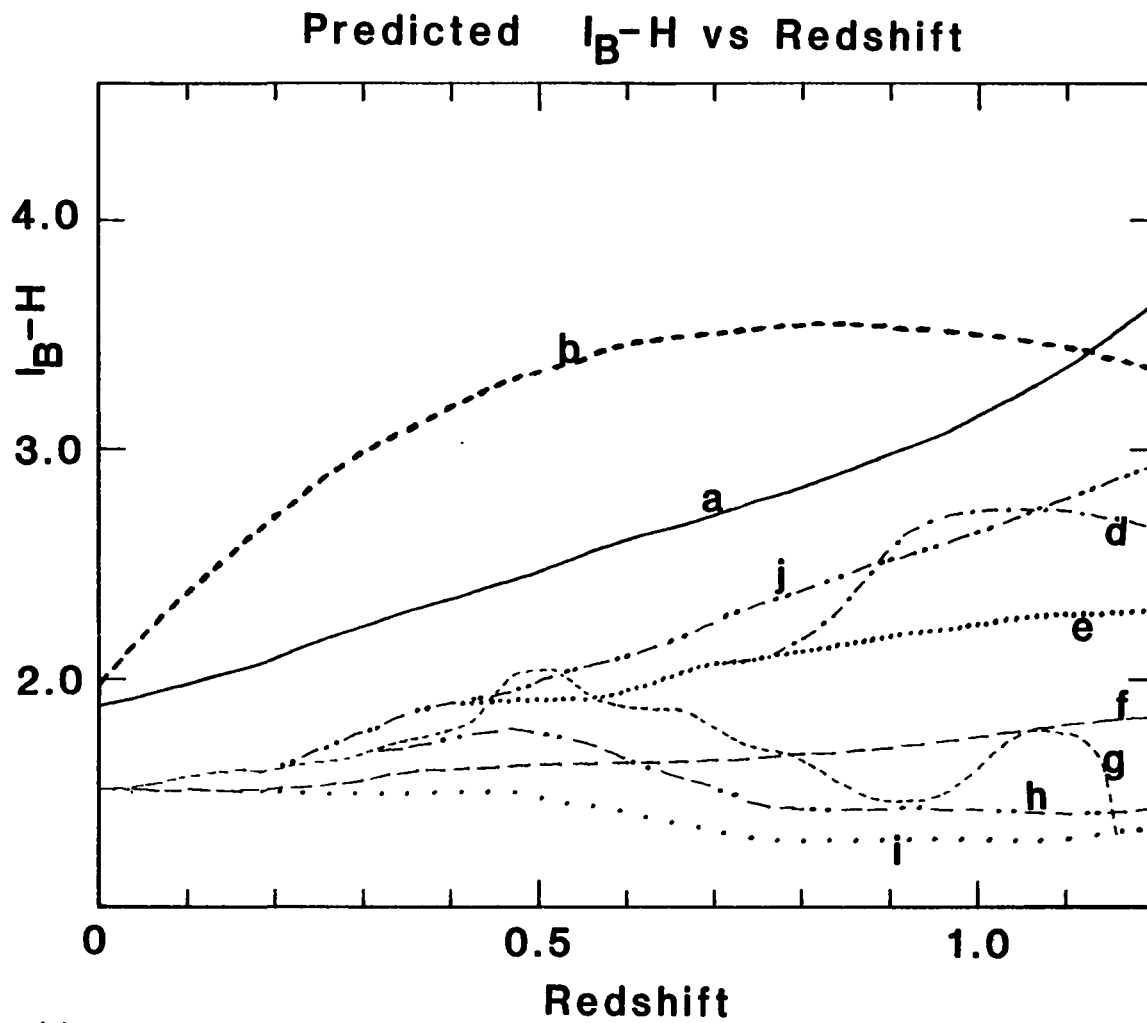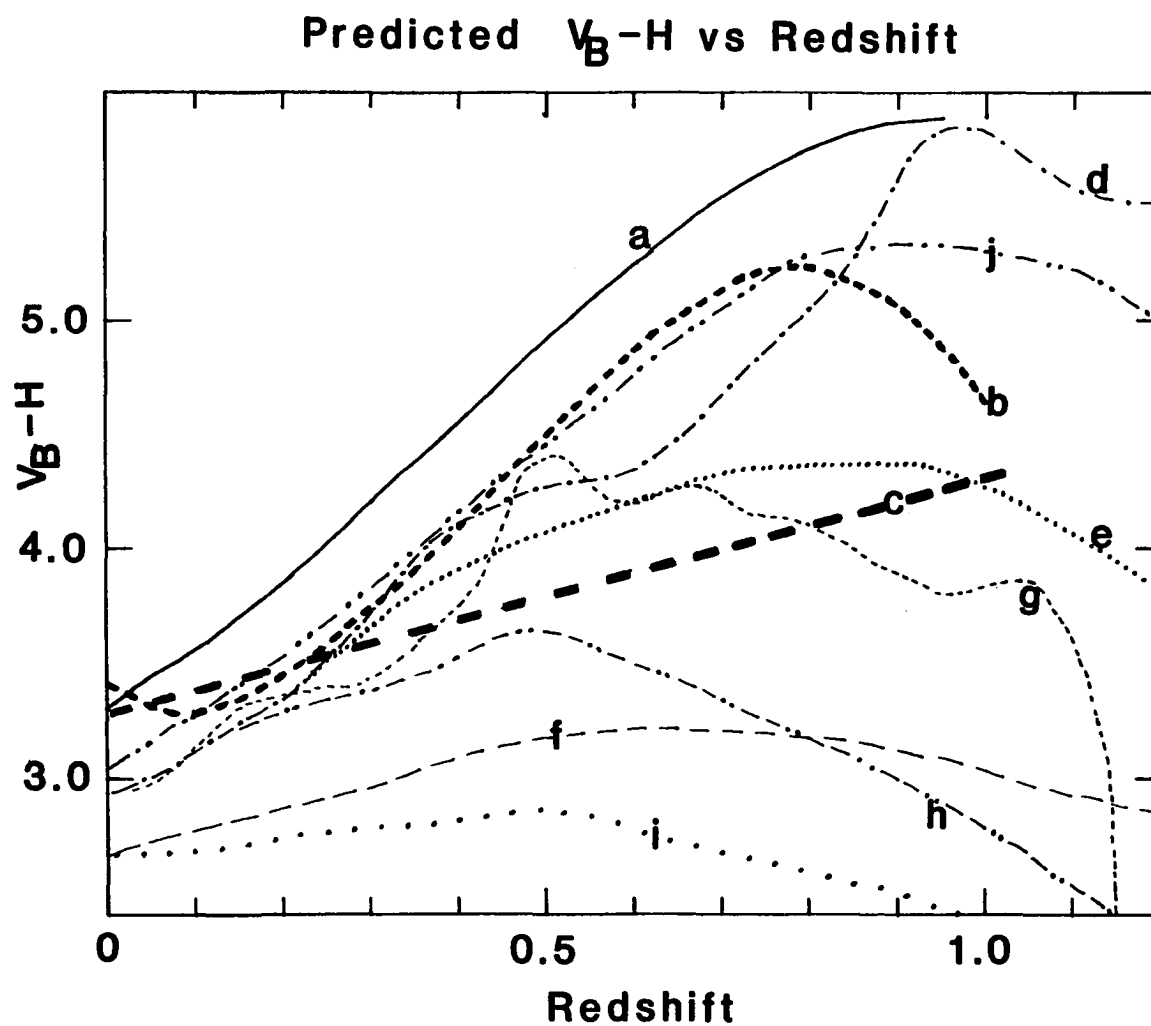ion of 0.09 magnitudes for the fifth order fit and the unselected set, both for redshifts above and below 0.5. For the selected set, a cosmic scatter of 0.035 mags for the fifth order fit and 0.05 for the predicted curve is consistent with the results. Because only one of the objects excluded from the selected set has a redshift greater than 0.5, the scatter is higher at high redshift for the selected set.

The conclusion to be drawn is that the spectrum of Figure 1 is an accurate representation of giant elliptical galaxies out to redshifts of one for wavelengths > 0.8 microns (λ_{eff} of H in the rest frame at $z = 1$), given a cosmic scatter in the color of 0.05 magnitudes. There is a possibility that the observed H-K color becomes bluer than the no evolution prediction for redshifts beyond one, but this is not statistically significant.

$\underline{I_B-H}$. The I_B-H color is troublesome. The scatter is large, and the agreement with the prediction of Table X is poor. Figure 14(b) shows the predicted curve and the weighted third order polynomial fit to a selected set of I_B-H observations. This set excludes 3C268.3 and 1613+31, which are extremely red; and 3C217, 3C252 and 3C368, which are relatively blue high redshift galaxies; as well as those omitted from the unselected set defined above (substituting 16KPNdelta for 3C337). 3C268.3 is also unusually red in H-K, while there is some expectation on

the basis of the results for V_B-H that I_B-H should start to show bluewards scatter near z = 1. 3C217, 3C252 and 3C368 are also quite blue in V_B-H.

Curiously, the agreement between prediction and fit is best at the endpoints. The observed data become red much more quickly than predicted, reaching a maximum (fitted) discrepancy of one magnitude, and are in obvious disagreement by z = 0.3. The observations then flatten, and eventually intersect the prediction as it rises at high redshift. The F test applied to the predicted curve vs. the polynomial fit shows there is much less than 1% chance the polynomial is not the better fit. Nonetheless, an intrinsic dispersion of 0.42 magnitudes about the fitted polynomial is required for the reduced chi square value to be unity for the unselected set, 0.36 mag for the selected set.

There are two issues which need to be addressed here: the systematic deviation from the prediction; and the large scatter. The possibility of systematic instrumental error was mentioned in Chapter 4 in the consistency section. Removing the June 1983 observations (made with the old cable arrangement) had no effect on either the scatter or the red deviation of the I_B-H observations. While this does not rule out an instrumental source for the problem, it suggests we look elsewhere. The scatter may have been caused by reference beam problems, but this is unlikely to have been overlooked for the low redshift objects, where the scatter is already large. Atmospheric variation is another possibility, but this should affect V_B more strongly than I_B, and scatter there is significantly smaller for redshifts below 0.4. The deviation from prediction is also in the opposite sense for V_B. It is

possible to come up with some reason for doubt about virtually any object (e.g. clouds, telescope troubles, low galactic latitude, inconsistency of multiple observations, discrepancy in another color, etc.) but there is no reason for all of these to conspire against I_B. The scatter is approximately five times greater than the typical standard deviation at I_B-H. We are left with two alternatives: the scatter is due to SPIV afterall, or it is intrinsic to the objects. Although the scatter needed to make the reduced chi square value unity is 0.4 at both low and high redshifts, the unadjusted (i.e. no scatter added in) reduced chi square values differ drastically above and below z = 0.31. For the unselected set, the low redshift value, with 38 points, is 46., while the high redshift value with 35 points is 5.2. The F test shows this result is extremely (<< 1%) unlikely to arise by chance. Evidently there is some component in the portion of elliptical galaxy spectra viewed by I_B out to z = 0.3 which varies from one galaxy to the next. The effective wavelength for I_B at z = 0.3 is 0.63 microns.

The systematic redward deviation of the observations also points towards a revision of the model spectrum, in the sense that the flux in the I_B region has been overestimated. There is supporting evidence for this in Lebofsky and Eisenhardt (1984). The low redshift J-K data there show surprisingly large scatter (though smaller than present in I_B-H here), and many points redward of the predicted color. As these observations were made with a different instrument, an instrumental origin for the problem is further discounted. A new photometer (Walker 1984), which uses a germanium photodiode and the integrating

preamplifier discussed in Chapter 2, will be used to investigate the 0.6 to 1.4 micron region of giant elliptical spectra in the next few months.

In summary, the I_B-H observations suggest elliptical galaxy spectra in the 0.6 to 1 micron region are different from one object to the next by several tenths of a magnitude, and that this region is generally fainter than was thought. Because of the possibility of instrumental error, this result needs confirmation.

$\underline{V_B\text{-}H}$. Two phenomena are evident in the plot of V_B-H vs. redshift: 1) The predicted curve represents an upper (red) envelope to the data; 2) At z = 0.4 the data, which had been tracking the predicted curve with moderate scatter, show a sudden large deviation towards the blue. Rather than follow a particular path in the color-redshift plane, however, the data beyond z = 0.4 are scattered over a two magnitude range, bounded on the red by the predicted no evolution curve.

It is clear that no reasonable polynomial can fit the data beyond z = 0.4. But before proceeding, we should check that the scatter is significantly greater at high redshift. A first order polynomial was fitted to the unselected set, which here excludes the (2 sigma limit) points 3C337, 21KPNsigma, 16KPNepsilon, and 3C427.1. The ratio of the reduced chi square values for points above and below z = 0.41 was evaluated using the F test. There is a less than 1% probability that the greater scatter at high redshift is due to chance.

To determine how well the predicted curve matches the low redshift points and the upper red envelope at high redshift, the following additional points were excluded in fitting polynomials: 4C25.04, 1134+015, 13F, 16KPNmu, 3C343.1, 3C217, 16KPNdelta, 3C280,

3C356, 3C252, and 3C368. All of these are bluer than predicted. 4C25.04, the only one of these with z < 0.4, showed erratic behavior at V_B when it was observed. 1134+015 is a Parkes (high frequency radio) source, and may therefore have a nonthermal component, although its other colors are normal. The rest are believed to be correct, and are excluded simply to aid in fitting a polynomial to the red envelope. Most of them were observed more than once, and were consistently blue in V_B-H. The third order polynomial fit to the selected set is shown in Figure 14(c), together with the predicted curve and the first order fit to the unselected set. The form of this fit is similar to the prediction, but consistently bluer. The F test showed this fit to be superior to the predicted curve at better than the 1% chance level for both the selected and unselected sets; and for both the complete redshift range and the low redshift (z < .41) objects. The reduced chi square value for the selected set and the predicted curve was minimized if the constant term of the predicted curve is adjusted from 3.31 to 3.00. For the low redshift objects, 3.02 is the optimum value for the predicted constant term. A scatter of 0.23 magnitudes is consistent with the low redshift data and either the fitted polynomial or the predicted curve with adjusted constant, while for the selected set at all redshifts, a scatter of 0.24 mag for the fit and 0.26 for the adjusted prediction makes the reduced chi square value unity. The F test for the adjusted prediction and fitted polynomial shows no significant difference between the two.

Comparison of Radio and Non-Radio Galaxies

The similarity of the colors of radio and non-radio galaxies in Figure 13 is striking. The distributions appear to be the same across the entire redshift range in each of the three colors. Radio and non-radio ellipticals were also found to have the same properties in Lebofsky and Eisenhardt (1984). This finding has important consequences regarding the optical/infrared properties of radio galaxies, and implies selection effects are not responsible for the deviations from the no evolution predictions. The purpose of this section is to verify statistically what is obvious to the eye.

Two approaches have been used to test the equivalence of the radio and non-radio distributions. The first compares the reduced chi square values of the two distributions with respect to polynomial fits across the whole redshift range, using the F test. In a few cases low and high redshift ranges were also tested. The second compares the mean deviation from polynomial fits, and variance about this mean, in smaller redshift bins.

Third order weighted polynomials were fitted to the radio data (selected set) only, and the reduced chi square of the radio data about this fit was compared to that for the non-radio data about the same fit. The results of the F test for the ratio of the two chi square values are shown in Table XIV. This polynomial clearly should favor the radio data, so this procedure actually emphasizes (perhaps overly so) differences between the two distributions. The chi square values were also calculated with respect to the polynomials fitted to the combined

data sets (from Table X), and the F test probabilities for this case are also shown in Table XIV. As expected, the latter probabilities are generally somewhat higher than those for the radio polynomials.

The second approach compares the two sets as a function of redshift. The price for this more detailed information is smaller samples and hence less reliable statistics. The two sets were divided into five redshift bins from $z = 0$ to $z = 1$. For the higher redshifts it was necessary to use larger bins to ensure there were at least two objects in each sample. The four objects with $z > 1$ were not analyzed because they are all radio galaxies. We wish to compare the mean properties of the two sets within each of these bins. Because there is still a fairly large redshift range ($\Delta z \geq 0.2$) in each bin, the systematic effects of redshift (e.g. the K correction) must be removed before the mean properties for the bin are calculated. This was done by subtracting the fitted polynomials of Table X from the data. The weighted means μ of the residuals in each bin are listed in Table XV. The t test (Freund and Walpole 1980) was used to determine if the difference between the radio and non-radio means was significant.

TABLE XIV

F Test Comparison of Radio and Non-Radio Galaxies

In the "Fit" column, HKR, IHR and VHR refer to the third order polynomials fit to the radio data (selected set). v_r and v_n are the number of degrees of freedom for the radio and non-radio samples respectively. The value of F shown is the ratio of the radio reduced chi square value to the non-radio value. Other terminology is as in Table XIII.

Color	Sample		Fit	v_r	v_n	F	P
H-K	uns		HKR	33	32	0.59	7%
H-K	uns		HK5	31	30	0.55	5%
H-K	sel		HKR	31	27	1.22	30%
H-K	sel		HK5	29	25	1.82	7%
I_B-H	uns		IHR	34	31	0.52	3%
I_B-H	uns		IH3	34	31	0.56	5%
I_B-H	sel		IHR	30	30	0.52	4%
I_B-H	sel		IH3	30	30	0.58	7%
I_B-H	sel	z<.31	IH3	15	19	0.72	26%
I_B-H	sel	z>.31	IH3	15	11	0.80	33%
V_B-H	uns		VHR	32	31	0.70	16%
V_B-H	uns		VH3	32	31	0.76	22%
V_B-H	uns	z<.4	VH1	20	25	0.64	15%
V_B-H	uns	z>.4	VH1	14	8	0.65	23%
V_B-H	sel		VHR	24	28	0.39	1.1%
V_B-H	sel		VH3	24	28	0.44	2.2%
V_B-H	sel	z<.4	VH3	17	23	0.51	8%
V_B-H	sel	z>.4	VH3	7	5	0.26	5%

TABLE XV

Comparison of Radio and Non-Radio Galaxies as a Function of Redshift

Galaxies are drawn from the given redshift range and the unselected set. μ_r and μ_n are the weighted mean deviations from the polynomial fits of Table X for the radio and non-radio samples. The number of galaxies in the range is given by v_r+1 or v_n+1. t is defined by equation 5.4, and P(t) is the corresponding probability. Other terminology is as for Table XIII.

Color	Redshift	μ_r	μ_n	v_r	v_n	t	P(t)	F	P(F)
H-K	0.0-0.2	0.00	-0.01	13	12	0.40	25-40%	0.65	6%
H-K	0.2-0.4	0.12	0.00	6	12	3.82	.2-.4%	0.75	37%
H-K	0.2-0.4*	0.09	0.00	5	12	3.41	.5-1%	0.37	14%
H-K	0.4-0.6	0.02	-0.07	6	4	1.97	5-10%	3.09	15%
H-K	0.6-1.0	-0.05	0.07	4	4	1.72	5-10%	0.18	6%
I_B-H	0.0-0.2	-0.09	0.05	13	12	0.95	10-25%	0.64	22%
I_B-H	0.1-0.3	-0.03	-0.03	7	12	0.01	>40%	0.82	41%
I_B-H	0.2-0.4	0.26	0.01	6	12	1.30	10-25%	0.30	8%
I_B-H	0.3-0.5	-0.08	0.08	7	8	1.23	10-25%	0.72	34%
I_B-H	0.4-0.6	-0.03	0.15	6	4	1.03	10-25%	0.26	7%
I_B-H	0.6-0.8	-0.02	-0.21	1	2	0.51	25-40%	7.82	12%
I_B-H	0.4-0.8	-0.03	0.03	8	7	0.48	25-40%	0.34	7%
V_B-H	0.0-0.2	-0.04	0.08	13	12	1.79	2.5-5%	1.10	44%
V_B-H	0.0-0.2*	-0.03	0.08	12	12	1.61	5-10%	0.91	44%
V_B-H	0.2-0.4	0.12	-0.05	6	12	1.18	10-25%	0.38	12%
V_B-H	0.4-0.6	0.38	0.10	6	4	0.73	10-25%	0.21	5%
V_B-H	0.6-1.0	-0.58	-0.37	4	3	0.53	25-40%	0.18	7%

* indicates 3C268.3 excluded for H-K, 4C25.04 excluded for V_B-H.

The t statistic is given by:

$$t = \frac{\mu_1 - \mu_2}{s_p \left[\dfrac{1}{N_1} + \dfrac{1}{N_2}\right]^{1/2}} \qquad\qquad 5.4$$

$$s_p^2 = \frac{(N_1-1)\sigma_1^2 + (N_2-1)\sigma_2^2}{N_1 + N_2 - 2}$$

$$\sigma^2 = \frac{\chi^2}{\dfrac{(N-1)}{N} \Sigma \dfrac{1}{\sigma_1^2}}$$

where χ^2 is the weighted <u>un</u>reduced chi square value about the polynomial fit calculated from the N data points in the redshift bin each with standard deviation σ_i. The number of degrees of freedom for the t test is $N_1 + N_2 - 2$. The probabilities corresponding to the t statistic were found from Table 26.10 of Abramowitz and Stegun (1965), and are listed in Table XV. They have the same significance as those for the F test, i.e. 50% is the optimum value, indicating no difference between the means. The dispersion about these mean deviations were compared using the F test, and these results are also listed in Table XV.

Overall, the results of these tests confirm the impression of equivalence of radio and non-radio galaxy colors. Of the 48 statistical tests (not all of them independent), 42 support equivalence, 1 supports distinct colors, and 5 are indeterminant, using the criteria adopted in the section on the F test above.

H-K

The one contrary test is the t test for the 0.2-0.4 redshift bin in H-K. The radio galaxies in this region are redder than the non-radio galaxies by 0.12 magnitudes. The mean deviation is only slightly reduced (to 0.09) if the reddest radio galaxy in this range, 3C268.3 (which was excluded from the selected set), is removed. As there are only seven radio galaxies in the bin, this result should be treated cautiously. If true, it is somewhat surprising that the colors should only be different for this intermediate redshift range. Possible explanations include a nonthermal contribution associated with the radio sources, and intergalactic reddening. If caused by a luminosity-color relation, it would be in the opposite sense from that previously reported (Visvanathan and Sandage 1977), as the radio galaxies in this range are <u>less</u> luminous on average than the non-radio galaxies (see Hubble diagram below).

Intergalactic Extinction. This topic has recently been reviewed by Rudnicki (1984). The lower average H luminosity for the radio galaxies is consistent in this case with the redder H-K colors, although Sandage (1972c) has found that radio galaxies extend to lower luminosities than first ranked cluster ellipticals. From equation 4.12, we would expect 0.36 magnitudes of extinction at H for 0.1 magnitudes reddening at H-K. However, the same relations predict 1.8 magnitudes reddening for these galaxies at V_B-H, and this is clearly not seen. We would also expect reddening to increase with redshift. The agreement with prediction to 0.1 mag at z = 1 for H-K sets a limit on intergalactic extinction of 0.5 mag/Gpc at V, assuming H_0 = 80km/sec/Mpc

and q_0 = 0.5. This value is 20 times lower than that reported in Rudnicki (1984). In fact, the limit is lower than this, as the effect of redshift was left out of this calculation.

Because of the preponderance of evidence that radio and non-radio galaxies are the same, I regard the mildly contrary result for H-K in the z = 0.2 to 0.4 range as erroneous, most likely due to the small number of objects in the sample. The infrared colors of radio galaxies in this redshift range should be studied more thoroughly, however.

I_B-H

Two of the indeterminate cases involve the F test for I_B-H across the whole redshift range, using the radio polynomial fit. The F test probabilities for the combined (radio + non-radio) polynomial fit are also at the low end of the acceptable range. This may be due to the difference in scatter above and below z = 0.3 found above, since the redshifts of the radio and non-radio galaxies are not distributed equally. When the F test was done separately for the two redshift ranges, the probabilities that radio and non-radio galaxies have the same colors rose to convincing levels. This is also seen in the fact that the t test for I_B-H unambiguously confirms equivalence in all the redshift bins.

V_B-H

The remaining three indeterminate tests involve V_B-H. The F test probability for all redshifts in the selected set is between 1 and 5% for both the radio and combined polynomial fits. This is partly due to the difference in scatter above and below z = 0.4, and mostly due to

large number of high redshift radio galaxies excluded from the selected set. The selected set is in this case a very biased sample. Nevertheless, when the F test was done separately on low and high redshifts using the selected set, the probabilities rise above 5%. The remaining indeterminate test is the V_B-H t test for the lowest redshift bin. The radio galaxies are somewhat bluer in this color than the non-radio galaxies. This may be an incidence of Sandage's (1972c) finding of a comparatively extended blue "tail" in the radio galaxy color distribution. Note that radio galaxies are also bluer at I_B-H in this bin, though not significantly. Alternatively, simply removing the questionable observation for 4C25.04 raises the t test probability over 5%, making the difference in color insignificant.

Colors Predicted by Evolutionary Models

At a redshift of one the lookback time is one half to two thirds of the age of the universe, for q_0 = 0 to 0.5. The stellar population of z = 1 galaxies must therefore be somewhat different from that of nearby galaxies, unless the star formation rate (SFR) is constant. The fact that nearby ellipticals consist mainly of old stars (Gunn, Stryker, and Tinsley 1981) implies that the SFR for ellipticals must have been much greater in the past.

Evolutionary Synthesis Models

There have been many studies of the effect of stellar evolution on integrated galaxy properties, most notably those of Beatrice Tinsley and her collaborators (e.g. Tinsley 1972 and 1977; Tinsley and Gunn 1976; Gunn, Stryker, and Tinsley 1981), using the evolutionary synthesis

technique. In this approach, analytic forms are assumed for the initial mass function (IMF) and SFR. When combined with theoretical evolutionary tracks for the range of star masses, the distribution of spectral/luminosity types as a function of time can be found. After assigning a properly normalized spectrum to each type, it is straight-forward to calculate the integrated spectrum of the model galaxy as a function of time. In general these studies have found that distant ellipticals should be more luminous and bluer than nearby ones. One would expect this naively, simply because distant galaxies should contain more young, luminous, blue stars. The situation is more complicated than this, however, because of the giant branch, which dominates the luminosity. The important parameter is x, the slope of the IMF, defined by:

$$\frac{dN}{dm} \propto m^{-(1+x)} \qquad\qquad 5.5$$

where dN/dm is the IMF and m is the mass. As the turnoff mass decreases, the rate at which a star moves onto the giant branch slows, and the luminosity drops. If x is large, however, the increasing number of stars compensates for the decreasing evolutionary rate, and the contribution of the main sequence to the luminosity is greater. Hence the luminosity drop is slower, while the redward motion of the turnoff changes the color. If x is small, the giant branch more completely dominates the luminosity, and the color changes more slowly because giant color is independent of mass (Tinsley 1972).

The models of Bruzual (1981) pay particular attention to the ultraviolet, where evolutionary changes are greatest, and cover a wide

range of SFR. At a redshift of unity, the effective wavelength of V_B is 0.26 microns in the emitted frame. For these reasons Bruzual's models were used to compare the observed colors with evolutionary predictions.

Modifications to Bruzual's Models. Bruzual (1981, 1983) lists the expected colors in several standard systems as a function of redshift for various models. Because the SPIV instrument response function (IRF) is nonstandard, it was necessary to obtain the actual spectra as a function of time. Bruzual kindly agreed to let me have these, and the spectra were conveyed to me by S. G. Djorgovski, who also provided software to work with the spectra, and whose assistance was invaluable.

Because only three spectral points beyond one micron are tabulated in the spectra, I decided to append the spectrum of Figure 1 to the model spectra, normalizing at one micron. This means the shape (but not the luminosity) of the infrared spectrum is unevolving. This is justified because Bruzual's three infrared points maintain the same relative fluxes independent of model and time, except for a brief period (10^8 years) following the epoch of galaxy formation. This epoch is almost certainly at redshifts well beyond those observed here.

The modified spectra were integrated over the SPIV IRF as a function of redshift and normalized to an A0 star spectrum (see e.g. equation 2.12). The assignment of redshift to time requires the choice of the galaxy formation redshift z_f; and of H_0 and q_0. The timescale varies by a factor of three for the range $H_0 = 100$ km/sec/Mpc, $q_0 = 0.5$ to $H_0 = 50$, $q_0 = 0$ (the age of the universe ranges from 6.5 to 19.6 billion years), so this choice is important. It is ironic that these

cosmological parameters must be known to study galaxy evolution, since one of the goals of such studies is to correct the value of q_0 obtained from the Hubble diagram for evolution. I have chosen $q_0 = 0.5$ because of the inflationary universe models, and $H_0 = 80$, with z_f a variable. The age of the universe is 8.15 billion years with these parameters, which is in mild conflict with the estimated ages of globular clusters.

The predicted color vs. redshift curves for several different cases are plotted in Figure 14. For the c models the SFR is constant for the first billion years (Gyr), and zero thereafter. The μ models have an exponentially decaying SFR. μ represents the fraction of the total mass that has formed stars after one Gyr. A μ-value of 0.7 is equivalent to an exponential timescale of 0.8 Gyr, a μ-value of 0.2 to a 4.5 Gyr timescale. All models shown here assume the Salpeter IMF, i.e. $x = 1.35$ in equation 5.5. Values of x less than 2 are required because of the observed dominance of giant stars in nearby ellipticals (Tinsley and Gunn 1976). Some models with the Miller-Scalo IMF were tried, but the difference in colors is negligible, as expected for small values of x. The formation redshift z_f was varied from 2 to 20.

Bruzual (1981) found that $\mu = 0.6$ to 0.7 models best reproduced the observed properties of ellipticals. Larger values of μ are not appreciably different from the c models. The $\mu = 0.2$ models are included in an attempt to reproduce the blue V_B-H colors, not because they are thought to be a realistic description of the global star formation rate in ellipticals. Similar remarks apply to the models with $z_f = 2$.

H-K

The infrared colors depend only slightly on details of evolution. All models are somewhat bluer at z = 1 than the no evolution prediction of Figure 1. This difference is in agreement with the observations. It implies the slope of the Figure 1 spectrum rises too steeply around one micron in the rest frame. This region was shown to create problems with the I_B-H colors at low redshift, but in the opposite sense. Very recent formation epochs (z_f < 3) appear to be ruled out, and larger values of μ fit the observations better than the low μ models, though this difference is slight. These results are in accord with the conventional picture of elliptical galaxy formation (Larson 1969), which says that most of the stars formed over a short period of time at an early epoch. Evolution in this scenario is the passive evolution of existing stars, with little or no active star formation at the redshifts observed here.

I_B-H

The problems at I_B noted earlier are only made worse when evolution is considered. While the z = 1 H-K observations imply Figure 1 underestimates the luminosity at I_B, the low redshift I_B-H observations imply Figure 1 overestimates this contribution. The observations are too red at low redshift, and evolution increases the discrepancy. The exception is at high redshift, where the observations flatten out and become bluer, as the evolutionary models predict. This flattening occurs at a level over one magnitude redder (at z = 0.5) than predicted. The observations do not permit a more specific statement.

The large scatter at I_B-H at low redshifts is hinted at again in the high redshift H-K observations, and clearly needs to be understood before more detailed comparisons with evolutionary models are possible.

V_B-H

Evolution has the greatest impact on V_B, and some of the V_B-H observations are much bluer than the no evolution prediction. Others at similar redshift are nearly as red as this prediction. Hence it is clear that no one model is capable of reproducing all of the observations.

The upper red envelope of the V_B-H data is consistent with either the no evolution or the c model. The c model is actually a better fit than no evolution model, implying that the V flux in Figure 1 has been underestimated relative to that at H. The μ models cannot produce the red colors of the high redshift galaxies for H_0 = 80 and q_0 = 0.5. This demonstrates the powerful effect of even a small rate (5% for μ = 0.7, z_f = 20, at z = 1) of residual star formation on V_B. More time is needed than the cosmological parameters chosen allow for a μ = 0.7 model to be sufficiently red at z = 1. This is illustrated by the μ = 0.5, z_f = 5 curve in Figure 14(c), which used H_0 = 50, q_0 = 0.

Either low values of μ or very recent formation redshifts are needed to produce the blue envelope of the V_B-H observations. Essentially some way of getting hot blue stars is required, and these are only available in the models if there has been recent star formation. The H-K data, however, suggest this has not happened on a global scale. On the other hand, the V_B-H data are not so blue as to

require that the majority of stars formed recently. This is best illustrated by the c model with z_f = 2. In this model star formation continues at a constant rate up to z = 1.16, and then terminates. The dramatic effect of the onset of star formation is shown by the precipitous ·blueward plunge of this model for z > 1.1, in all colors.

A possible explanation for the V_B-H observations, then, is that some of the elliptical galaxies have had bursts of star formation at or just prior to the redshifts observed, but the majority of stars formed long ago. A crude estimate of the required level of star formation can be made by assuming the deviation from the red envelope is entirely due to O stars. At a redshift of 0.4, V_B is roughly equivalent to U. Taking the absolute U magnitude to be -19.5 for present day ellipticals (Sandage 1972c) and -9.5 for an O supergiant, roughly 20,000 O stars are required to produce a one magnitude excess (as shown for example by the galaxy 13F). Using the Salpeter IMF, roughly 10^7 stars would be formed in total, which would not significantly affect the overall galaxy properties. The conditions leading to such a starburst could well vary from one galaxy to the next, giving rise to the observed scatter. It is hard to see why this process should begin at a redshift of 0.4, however.

Comparison with Other Observers

Other investigators have found excess blue light beginning at redshifts near 0.4 (Lilly and Longair 1984, Butcher and Oemler 1978). It has been suggested by DeGioia-Eastwood and Grasdalen (1980) that this may be caused by the variation observed in the ultraviolet spectra of nearby ellipticals, as these wavelengths are redshifted into the V band.

However, Bertola, Capaccioli and Oke (1982) show that this variation only occurs below 2500 Å, and is about 1 magnitude by 2000 Å. Because V_B is not sensitive below 4200 Å, these variations should not affect the observations for redshifts < 0.7. On the other hand, it has been suggested that these same variations are indeed caused by a young star population, just as proposed here (Gunn, Stryker and Tinsley 1981). Other explanations include hot stars which are not young, such as blue stragglers or horizontal branch stars (see e.g. Bruzual 1983). If these are part of the normal evolutionary sequence, however, it is difficult to explain the wide range of V_B-H observed.

Lilly and Longair (1984) in a study of a well defined sample of 3C galaxies find the same results as are presented here: the infrared colors behave as expected, while the optical/infrared colors (derived from CCD observations for a subset of their sample) show a large blueward scatter at high redshifts. This implies the radio galaxies observed here are not systematically biased by unknown selection effects. The lack of difference between radio and non-radio galaxies strongly suggests the latter are also representative. It is therefore curious that Oke (1984) states that there is no evidence for changes of colors with redshift for their optically selected sample, since the non-radio galaxies observed here are drawn from this same sample. In fact the statement is at odds with the data presented in Oke's Figures 4 and 5, and with an earlier statement that there is a hot uv source which varies from galaxy to galaxy. It is true that the scatter in color means there is no well-defined correlation of color with redshift,

and when interpreted in this way there is no contradiction between Oke's statement and the findings presented here.

The Hubble Diagram

Although this dissertation is concerned with color evolution, the H magnitudes merit some attention. The data of Table VII have been plotted as a function of redshift, after applying the K correction of Table X, in Figure 15. Expected relations for the cases q_0 = 0, 0.5 and 1 with no evolution are shown. Because the aperture correction was calculated for q_0 = 0.5, the observed magnitudes will change somewhat for $q_0 \neq 0.5$; the respective changes for z = 1 are shown by arrows under the labels q_0 = 0 and q_0 = 1. The radio galaxies appear to be somewhat fainter at intermediate redshifts than the non-radio galaxies. This was briefly noted above in the discussion of H-K for radio vs. non-radio galaxies.

Larger values of q_0 appear to be favored by the high redshift data. This is enhanced by the fact that the galaxies on the faint side of the plot have lower weight. For example the z = 0.92 non-radio galaxy 16KPNepsilon is less than a two sigma detection. The effect of evolution must be considered however. The evolutionary correction (equation 2.8) for the c model with z_f = 20, H_0 = 80, q_0 = 0.5 is shown for z = 1. This correction depends on the choice of cosmology and evolutionary model, but it is clear that the effect of evolution is greater than that of q_0, unless q_0 is quite large. Both issues are considered in much greater detail in Lebofsky and Eisenhardt (1984).
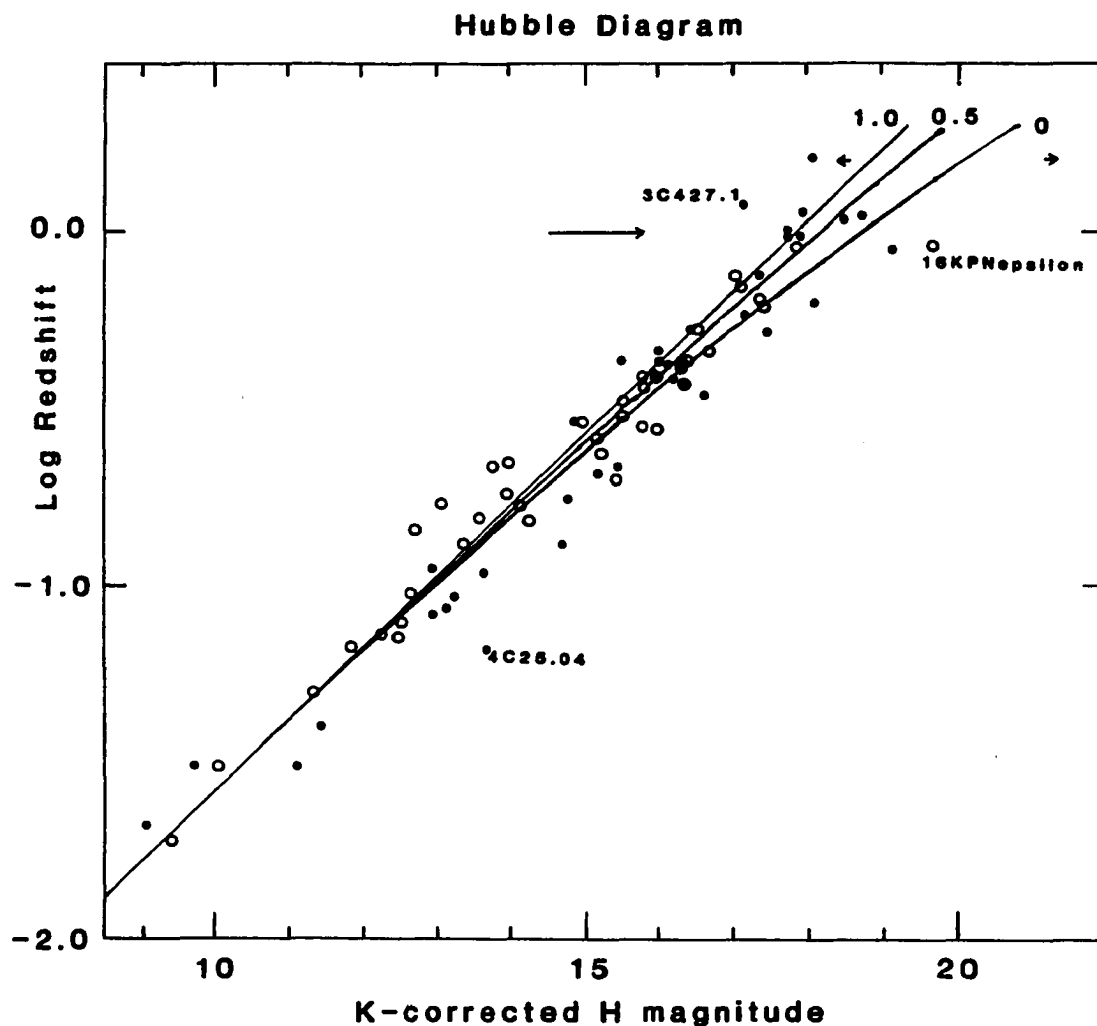
Hubble Diagram

Figure 15. Hubble Diagram. The relations for q_0 = 0, 0.5, and 1 are labelled with the appropriate value. The small arrows beneath 1 and 0 show the motion of the magnitudes for these values of q_0 because the aperture correction applied was for q_0 = 0.5. The much larger arrow pointing towards fainter magnitudes at the log z = 0 level indicates the evolutionary correction for the c model with z_f = 20, H_0 = 80, q_0 = 0.5, at a redshift of one.

The conclusions found there, namely luminosity evolution of about one magnitude by z = 1, and q_0 = 0.3, are consistent with the observations shown here, and will not be discussed further.

Determining Redshifts from Colors

Finally, the prospects for estimating redshifts from broad band colors should be discussed. This was one of the original motivations for building SPIV. The no evolution prediction for V_B-H is a steep function of redshift, and it was hoped this would allow redshifts of order one to be estimated to 10% accuracy in half hour MMT integrations.

Unfortunately the scatter in V_B-H prevents this technique from being reliable for the most interesting redshifts, z > 0.4. Although the observations follow the H-K prediction well, the relation is quite flat beyond z = 0.3, while large scatter at low redshift and a flat relation at higher redshift makes I_B-H of little use. For example, 16KPNmu, with z = 0.61, has colors which are indistinguishable from those of 3C436, at z = 0.215. The H magnitudes are of course very different, and this appears to be the most reliable way of estimating redshift, but no information about q_0 or luminosity evolution can then be obtained.

CHAPTER 6

CONCLUSIONS

The construction of the Simultaneous Photometer for Infrared and Visual light has allowed some of the questions posed at the beginning of this dissertation to be answered, and inevitably raised new ones.

Observations with SPIV have demonstrated that its performance is limited by noise levels set by background radiation from the sky for V_B and H, and thermal radiation from the sky and telescope for K. The only way to improve the performance for these channels is to reduce the background levels, or to improve the instrument's transmission and the quantum efficiency of the detectors. Only the V_B channel has a quantum efficiency significantly less than one, while reducing the background requires less atmosphere, better seeing and/or array detectors to reduce the pixel size, or reduced telescope emission for K. Progress in all of these areas is underway at many institutions. The I_B channel is limited by detector/preamplifier noise, and its performance will be improved by using the integrating preamplifier design of Low (1984). SPIV's performance at H is unlikely to be surpassed until array detectors become available. The limiting magnitudes currently achievable with SPIV are given in Table IV.

Observations of nearly eighty radio and optically selected elliptical galaxies at redshifts from 0 to 1 have yielded several interesting results.

131

There are no convincing differences between the optical/infrared properties of radio and non-radio galaxies. The distribution of these two groups appears to be identical in all colors measured at all redshifts less than one. Possible exceptions are the intermediate redshift (z = 0.2 to 0.4) radio galaxies, whose H-K colors may be slightly redder, and luminosities slightly lower. More observations of radio galaxies at these redshifts are needed. Two important consequences of this result are that radio sources do not significantly alter the optical/infrared properties of giant ellipticals, and that selection effects are unlikely to have affected the samples studied here.

The infrared H-K color varies with redshift as predicted. Although the differences are small, a passively evolving model in which most or all the stars formed at an early epoch is favored over models with protracted star formation. Galaxy formation epochs $z_f > 3$ are indicated. These models also fit the high redshift observations slightly better than does the unevolving prediction created by redshifting Figure 1. The models predict galaxies at a redshift of one are about one magnitude brighter at H than they would be with no evolution.

The I_B-H color shows the most perplexing behavior. Galaxies become redder with redshift much more rapidly than the reddest prediction (the no evolution model), and show a wide scatter in color for redshifts less than 0.3. This result is supported by J-K observations in Lebofsky and Eisenhardt (1984). The spectra of giant ellipticals from 0.6 to 1.4 microns needs further study. Some component

affects this region in a way that varies from one galaxy to the next. The high redshift observations flatten and show individual blue deviations in agreement with the V_B-H colors. A flattening trend is also seen in the evolving models.

Two forms of behavior are displayed by the V_B-H observations. Some galaxies parallel the no evolution prediction out to redshifts of one. This red envelope is about 0.3 magnitudes bluer than the no evolution model, and is better fit by a passively evolving model with no residual star formation and a galaxy formation epoch $z_f > 3$. This result is in accord with the H-K observations. Models with exponentially declining star formation rates cannot match the red colors at high redshift for $q_0 = 0.5$, $H_0 = 80$, requiring an older universe. Beginning at $z = 0.4$, some galaxies show strong blueward deviations from the red envelope. The bluest galaxies at $z = 1$ have V_B-H colors similar to nearby ellipticals, and are three magnitudes bluer than the no evolution prediction. This behavior is most easily explained by episodes of star formation at epochs $z < 1$, involving a small fraction of the total number of stars in a giant elliptical. High quality images of galaxies with large blue excesses should be very interesting. These results are in agreement with those of Lilly and Longair (1984); Gunn, Stryker, and Tinsley (1981); and Butcher and Oemler (1978, 1984).

The above results indicate determining redshifts from broad band colors will be difficult for $z > 0.4$. The flatness of H-K and I_B-H coupled with the scatter in V_B-H mean that galaxies of widely differing redshifts can have the same colors.

Finally, it is clear that cosmological studies should favor infrared observations over optical ones. High redshift galaxies are easier to detect in the infrared, and much better behaved. Optical colors are more sensitive to evolution, but their sensitivity to relatively small amounts of star formation can easily overwhelm the subtle effects of differing cosmologies. SPIV is well suited to study both evolutionary and cosmological effects.

REFERENCES

Aaronson, M. and Mould, J. 1983, _Ap. J._, **265**, 1.

Abramowitz, M., and Stegun, I. A. 1965, eds. _Handbook of Mathematical Functions_ (4th printing; Washington: U.S. Govt. Printing Office).

Bertola, F., Capaccioli, M., and Oke, J. B. 1982, _Ap. J._, **254**, 494.

Bevington, P. R. 1969, _Data Reduction and Error Analysis for the Physical Sciences_ (New York: McGraw Hill).

Blanco, V. M., Demers, S., Douglass, G. G. and Fitzgerald, M. P. 1968, _Pub. USNO_, **21**.

Broadfoot, A. L., and Kendall, K. R. 1968, _J. Geophys. Res._, **73**, 426.

Bruzual, G. 1981, Ph.D. thesis, University of California, Berkeley.

Bruzual, G. 1983, _Ap. J._, **273**, 105.

Burbidge, G. and Crowne, A. H. 1979, _Ap. J. Suppl._, **40**, 583.

Burstein, D. and Heiles, C. 1982, _A. J._, **87**, 1165.

Butcher, H. and Oemler, A. G. 1978, _Ap. J._, **219**, 18.

_____. 1984, _Ap. J._, submitted.

Chamberlain, J. W. 1961, _Physics of the Aurora and Airglow_ (New York: Academic Press), p. 366.

DeGioia-Eastwood, K. and Grasdalen, G. L. 1980, _Ap. J (Letters)_, **239**, L1.

Djorgovski, S. G. 1984, private communication.

Dressler, A. 1984, _Ann. Rev. Astron. Ap._, **22**, 185.

Eisenhardt, P. R. M. 1982, _Proc. S.P.I.E._, **331**, 434.

Elias, J. H., Frogel, J. A., Matthews, K. and Neugebauer, G. 1982, _A. J._, **87**, 1029.

Ellis, G. F. R. 1984, Ann. Rev. Astron. Ap., 22, 157.

Ellis, R. S., and Allen, D. A. 1983, M.N.R.A.S., 203, 685.

Féry, Ch. 1911, Ap. J., 34, 79.

Freund, J. E., and Walpole, R. E. 1980, Mathematical Statistics (3rd
    ed.; Englewood Cliffs: Prentice Hall).

Frogel, J. A., Persson, S. E., Aaronson, M., and Matthews, K. 1978,
    Ap. J., 220, 75.

Grasdalen, G. L. 1980, in IAU Symposium 92, Objects of High Redshift,
    eds. G. Abell and P. J. E. Peebles (Dordrecht: Reidel), p. 269.

Grueff, G., Vigotti, M., and Spinrad, H. 1980, Astr. Ap., 86, 50.

Gunn, J. E. 1980, private communication to M.J. Lebofsky.

Gunn, J. E., and Oke, J. B. 1975, Ap. J., 195, 255.

Gunn, J. E., Stryker, L., and Tinsley, B. 1981, Ap. J., 249, 48.

Guth, A. and Steinhardt, P. 1984, Sci. Am., 250 No. 5, 116.

Hayes, D. S. 1982, KPNO Newsletter, No. 21, June 1, p. 5.

Hoessel, J. G. 1980, Ap. J., 241, 493.

Hubble, E. P. 1936, Ap. J., 84, 270.

Janes, K., and Demarque, P. 1983, Ap. J., 264, 206.

Johnson, H. L. 1966, Ann. Rev. Astron. Ap, 4, 201.

Kristian, J., Sandage, A., and Westphal, J. A. 1978, Ap. J., 221, 383.

Laing, R. A., Riley, J. M., and Longair, M. S. 1983, M.N.R.A.S., 204,
    151.

Larson, R. B. 1969, M.N.R.A.S., 145, 405.

Lebofsky, M. J. 1981, Ap. J. (Letters), 245, L59.

_____. 1984, private communication.

Lebofsky, M. J., and Eisenhardt, P. R. M. 1984, Ap. J., submitted.

Lebofsky, M. J., and Rieke, G. H. 1984, in preparation.

Lilly, S. J., and Longair, M. S. 1982, M.N.R.A.S., 199, 1053.

_____. 1984, M.N.R.A.S., in press.

Low, F. J. 1984, Appl. Opt., **23**, 1308.

Low, F. J., and Rieke, G. H. 1974, in Methods of Experimental Physics, Vol. **12A**, ed. N. Carleton (New York: Academic Press), p. 415.

Moffett, T. J., and Barnes, T. G. 1979, A. J., **84**, 627.

Montgomery, E. F. 1982, private communication.

Oke, J. B. 1984, Clusters of Galaxies with Very Large Redshifts, paper presented at the Meeting on Clusters and Groups of Galaxies at Trieste, September 1983.

Oke, J. B., and Sandage, A. 1968, Ap. J., **154**, 21.

P. J. E. Peebles 1971, Physical Cosmology (Princeton: Princeton University Press), p. 184.

Puschell, J. J., Owen, F. N., and Laing, R. A. 1982, Ap. J. (Letters), **257**, L57.

Rieke, G. H. 1982, private communication.

Rieke, G. H., and Lebofsky, M. J. 1984, Ap. J., in press.

Rieke, G. H., Montgomery, E. F., Lebofsky, M. J., and Eisenhardt P. R. 1981, Appl. Opt, **20**, 814.

Rudnicki, K. 1984, Sky Tel., **68**, 123.

Sandage, A. 1972a, Ap. J., **173**, 485.

_____. 1972b, Ap. J., **178**, 1.

_____. 1972c, Ap. J., **178**, 25.

_____. 1973a, Ap. J., **180**, 687.

_____. 1973b, Ap. J., **183**, 711.

Sandage, A., Sandage, M., and Kristian, J. ed. 1975, Stars and Stellar Systems, Vol. **9**, Galaxies and the Universe (Chicago: University of Chicago Press), p. viii.

Smith, R. A., Jones, F. E., and Chasmar, R. P. 1957, The Detection and Measurement of Infra-Red Radiation, (Oxford: Oxford University Press), p. 330.

Smith, H. E., and Spinrad, H. 1980, Pub. A. S. P., **92**, 553.

Spinrad, H. 1982, Pub. A. S. P., **94**, 397.

_____. 1984, private communication to M. J. Lebofsky.

Spinrad, H., Djorgovski S., and Marr, J. 1983, Bull. AAS, **15**, 932.

Spinrad, H., Stauffer, J., and Butcher, H. 1981, Ap. J., **244**, 382.

Tinsley, B. M. 1967, Ph.D. Thesis, University of Texas, Austin.

_____. 1972, Ap. J., **178**, 319.

_____. 1977, Ap. J., **211**, 621.

Tinsley, B. M., and Gunn, J. E. 1976, Ap. J., **203**, 52.

Veeder, G. J. 1974, A. J., **79**, 1056.

Visvanathan, N., and Sandage, A. 1977, Ap. J., **216**, 214.

Walker, C. 1984, preprint.

Weinberg, S. 1972, Gravitation and Cosmology (New York: Wiley).

Wolfe, W. L., and Zissis, G. J. ed. 1978, The Infrared Handbook (Washington: Office of Naval Reserach), pp. 5-88 and 5-91.